TECHNISCHE UNIVERSITÄT DARMSTADT

Department for Renewable Energies
Institute of Electrical Power Systems

PhD thesis

Ayman B. T. Attya

WIND ENERGY PENETRATION IMPACT ON GRID FREQUENCY DURING NORMAL OPERATION AND FREQUENCY DEVIATIONS

„Gedruckt mit Unterstützung des Deutschen Akademischen Austauschdienstes“

Wind energy penetration impact on grid frequency during normal operation and frequency deviations

Dem Fachbereich Elektrotechnik und Informationstechnik
der Technischen Universität Darmstadt
zur Erlangung des akademischen Grades eines
Doktor-Ingenieurs (Dr.-Ing.)
genehmigte Dissertation

von

Ayman Bakry Taha Attya, M.Sc.

Geboren am 17.05.1983 in Giza, Ägypten

Referent:	Prof. Dr. Thomas Hartkopf
Korreferent:	Prof. Dr. Gerd Griepentrog
Extern Korreferent:	Prof. Dr. Yasser Hegazy
Tag der Einreichung:	11.06.2014
Tag der mündlichen Prüfung:	30.09.2014

D 17

Darmstadt 2014

Erklärung laut §9 Promo

Ich versichere hiermit, dass ich die vorliegende Dissertation allein und nur unter Verwendung der angegebenen Literatur verfasst habe. Die Arbeit hat bisher noch nicht zu Prüfungszwecken gedient.

Preface

Due to increasing wind power penetration the power system impact of wind power is a relevant aspect of research. The present PhD thesis deals with possible support algorithms for wind turbines to participate positively in frequency drops mitigation. Comprehensive dynamic simulation models for wind turbines and conventional generators are integrated in order to simulate their interaction during frequency deviations. In the present thesis, storage mediums are also investigated as a solution for wind energy intermittent nature and its impact on frequency response. The Egyptian case study real and chronological data acquired from related authorities is considered as a benchmark system for the examined algorithms.

The PhD research was carried out in the Institute of Electrical Power Systems - Department of Renewable Energies at Technical University of Darmstadt (Germany). This research work is funded through cooperation between the Egyptian ministry of high education and research from one side and the DAAD (German Academic Exchange Service) from the other side. The duration of the scholarship was from April 2011 till September 2014.

Summary

The fluctuating nature of output from wind farms in relation to wind speed conditions at each wind turbine causes a severe burden on conventional generators, and such wind power variations have a considerable impact on grid frequency and voltage stability. In addition, such fluctuations in output create economic problems, as most of system operators apply financial penalties on wind farms owners when generation levels deviate from forecasted schedules by certain ratios. This thesis focuses on the negative impacts of moderate and high levels of wind power contribution to grid generation capacities on the frequency response. Particularly, integrated wind farms replace certain ratios from conventional generation capacity. Retired conventional capacity is decided according to estimated annual energy production of installed wind farms.

The work presented here focuses on the contribution of wind turbines in the curtailment of frequency drops. Specifically, two algorithms are proposed to provide a predetermined increase in wind farms active power to support the system and mitigate the generation–demand imbalance. One algorithm relates to the stored kinetic energy in the wind turbine rotating parts, and the other relates to the steep rise in output power that is delivered when the wind turbine pitch angle given value in de-loading operation, is reduced to zero. The two offered algorithms are compared mainly from the point of view of energy utilization with respect to standard operation. A dispatching algorithm is also presented to manage the number of wind turbines in each wind farm that should be switched to support mode, and a modified method for estimating the retired conventional generation capacity is also presented. Thus, the expected amounts of annual energy generated by different types of wind turbines in different sites are evaluated based on the available chronological wind speeds records and network load. Finally, this thesis discusses the feasibility and influence of integrating storage mediums, namely battery banks, as a backup power source during frequency events.

Throughout all the mentioned analysis, frequency responses of several hypothetical and a genuine system, namely, the Egyptian system, are examined in different case studies to investigate the impact of the proposed algorithms on frequency performance. MATLAB and Simulink are the main software applied. Results acquisition reveals the capability of wind farms on mitigating frequency drops. The proposed algorithms are seen to deliver advantages and disadvantages, and selection based on compromise is required to choose the best solutions that match the investigated case studies.

Zusammenfassung

Die natürlichen Schwankungen der Leistung von Windparks aufgrund fluktuierender Windgeschwindigkeiten haben einen nicht unerheblichen Einfluss auf die Qualität der Stromversorgung. Die vorliegende Dissertation konzentriert sich daher auf den Einfluss von Windparks auf die Frequenzstabilität in elektrischen Versorgungsnetzen. Dieser Einfluss ist wichtiger und klarer wenn mehr Windparks konventionelle Generatoren auswechseln.

Es werden zwei spezielle Algorithmen vorgestellt, welche eine Erhöhung der aktiven Windparkenergie ermöglichen, die Stabilität des Erzeugungssystems verbessern und die Bilanz von Erzeugung und Nachfrage ausgleichen sollen. Der erste Algorithmus bezieht sich auf die in den rotierenden Teilen der Windkraftanlage gespeicherte kinetischen Energie. Der zweite Algorithmus betrifft den Blatteinstellwinkel, der die Drehgeschwindigkeit des Rotors verändern kann. Während des normalen Betriebs bei entsprechendem Wind ist der Blatteinstellwinkel größer als Null und sinkt, wenn ein Frequenzabfall eintritt. Die beiden hier vorgestellten Algorithmen werden dabei hauptsächlich aus dem Blickwinkel der Energienutzung mit Bezug auf den Normalbetrieb verglichen.

Die vorliegende Forschungsarbeit bietet auf Basis chronologischen Daten für Netzbelastung und Windgeschwindigkeit auch eine neue Methode zur Berechnung der jährlichen Energieproduktion der Windkraftanlagen. Zusätzlich ist eine neue ‚Dispatch'-Methode in die Algorithmen integriert, welche die Unterstützungsrolle für jede Windkraftanlage in jedem Windpark während eines Frequenzproblems definiert.

Eine neuartige Lösung zur Einbeziehung von Speichermedien, insbesondere Batteriebänken, wird zum Abschluss der Arbeit vorgeschlagen und die Energiekapazität sowie die Leistung der Batterien bewertet. Der Einsatz der Batterien zielt zunächst auf eine Aufladung während des Normalbetriebs und bei guten Windkonditionen ab. Danach sind die Batterien in der Lage, zusätzliche Wirkleistung zu liefern, um einem plötzlichen Frequenzabfall unter bestimmten Bedingungen entgegenwirken zu können.

Die gesamte Analyse wird anhand hypothetischer Systeme und *anschließend* für das ägyptische Netz und die dortige Windenergienutzung untersucht. Alle Fallstudien vergleichen und analysieren die Frequenzkurven vor und nach der Integration der präsentierten Methoden und zeigen deren Vor- und Nachteile auf. Als primäre Simulationssoftware wurden MATLAB und Simulink verwendet. Es hat sich ergeben, dass die hier vorgeschlagenen Algorithmen zwar das Potential zur Minderung von plötzlichen Frequenzabfällen besitzen, aber dennoch eine kompromissbasierte Auswahl nötig ist, um die optimale Lösung für die jeweils untersuchte Fallstudie zu finden.

Contents

1. Introduction

Throughout the world, electrical energy is a priority issue for governments, companies, and research institutes, and varying viewpoints are continually be presented in relation to the optimum priorities of generation technologies in both developed and developing countries. For example, developed countries are mainly concerned with the reduction of pollution emissions caused by conventional power plants using fossil fuels such as coal and oil. In the past, nuclear energy was a favourite option for some of these countries, but due to a number of global accidents (such as the tsunami disaster in Japan that caused destruction of nuclear reactors with catastrophic consequence) nuclear reactors are now being perceived as potential threats. Developing countries are seeking solutions for the mitigation of high conventional energy prices and for the political and economic limitations imposed on them in relation to building nuclear reactors. Consequently, renewable energy provides a solution for both teams. Solar, wind, biomass, geothermal, and tidal energies are well known examples of renewable energy resources that are widely used globally at different rates and levels of technology [1]. However, solar and wind power generation are the most commonly used methods nowadays, and statistics show that wind power capacity has increased at a rate of over 20% per year over the past decade in the U.S. and Europe, and the future energy share of wind-generated power will be more than 20% within the next two decades [2]. Similarly, the Danish government and other concerned parties have conceived a plan to increase the wind energy share in the Danish power system to 50% of the grid's overall capacity. In relation to solar energy generation, however, the special requirements involved in its production, namely, the high technology and costly fabrication methods of energy cells and the huge land areas required, are basic constraints preventing the spread of its use [3]. In contrast with solar-generated power, wind is available throughout most of the year, and many different types of wind turbines (WTs) are offered by several companies, with different models delivering relatively low ratings and affordable prices. However, highly rated and advanced WTs equipped with complicated controllers are also available presenting the unremitting efforts that are involved in reaching perfection in energy harvesting efficiency and retaining power system stability [4].

1.1. Motivation

Resolution of the unpredictable and sharply variable nature of output power from renewable power plants is a basic challenge facing power systems engineers. Higher levels of renewable energy generation make the handling of such power variations much more complex, and imply negative influences on system stability. Wind power naturally fluctuates with the intermittent nature of wind speed (WS) which differs between one WT and another in the same wind farm (WF) [5, 6]. However, single and small wind power distributed units installed within the power system do not clearly affect power system operation, but when wind power penetration reaches significantly high levels, and conventional power plants are replaced, the impact of wind power on the power system becomes

noticeable, especially in the form of the number of mismatched events between generation and demand [**7**].

The routine control methods for conventional power plants offer a wide and flexible range of solutions for power systems operators, particularly during system faults and unexpected events. For instance, it is generally easy and practicable to control the amount fuel flow used to run gas and oil generators, while it is impossible to control instantaneous WS, or even to have an accurate prediction of its value. Therefore, many papers in the field of wind power integration in power systems have been published in relation to wind power integration within the power system, and how to overcome or reduce its negative impact on the system voltage and the frequency stability [8, 9]. In some cases, there is no palpable negative impact; nevertheless, the development of feasible methods is required in order to ensure that WFs operate similar to conventional power units, particularly during periods of frequency drop. In fact, the major role of any power plant is to generate active power that covers the required load demand; hence, a variation in the injected fuel amounts at a power plant yields undesired fluctuations in the generated power. These generated power variations directly affect the power system frequency, which is a very important factor, and has a very narrow range of diversity that is acceptable from its nominal value [10].

Nowadays, most installed WTs are equipped with power electronic converters so that the operator has the option of controlling the speed, and the active and reactive power of the WT through predetermined parameters. The above-described problem worsens if the certain ratio of conventional power plants is replaced by WFs, where the process of substitution is constrained by the grid code fulfilment. Nevertheless, driving WFs during system frequency drops is one of the most debated points concerning high levels of wind energy integration, and requires the application of appropriate ride-through and support algorithms [11].

It is therefore clear why a wide spectrum of renewable energy research efforts is focused on providing feasible solutions for unexpected and fluctuating performance of WT power generation. The top priority at present is to propose wise and efficient control mechanisms for WTs during frequency drops, so that WFs react in similar way to conventional generators. These mechanisms should find a balance between the mitigation of wasted wind energy due to applied control methods and retaining system stability.

This dissertation deals with the impact of high wind energy penetration levels, through two main focuses. Firstly, it controls and quantifies the amount of kinetic energy (KE) stored in the WT rotating parts. This KE is considered to be the foremost source for any required support from WFs during frequency excursions elimination. The second pivotal focus is on proposing a comprehensive WT frequency drop support algorithm to overcome expected problems that could occur in the displacement of conventional generation plants. Both algorithms merge several static and dynamic parameters that are related to the WT, WF, or the power system. Additionally, certain related topics are studied and

examined in a way that presents and implements these proposed algorithms, and include precise modelling of the different technologies used in conventional generators and several types of WTs, in addition to basic parameters that differ from one vendor to the other, and the overall suggested benchmark power system. It is of note that this research discusses simplified methods for assessing WF annual power generation in comparison with whole system capacity. Moreover, the integration of energy storage techniques is included and compared to the proposed support algorithms. Simplified mechanisms are applied for generating WSs in cases where there is a lack of sufficient data in relation to the WSs at a given site. In particular, WSs are recorded over a long time step, where monitoring changes in the WSs is required over very short time intervals to cope with system frequency fluctuations analysis.

The factuality of the proposed algorithms is fortified by integrating real data for WSs and power system parameters according to available information acquired from the Egyptian authority. At certain stages in the presented research work the offered methods are applied using hypothetical systems to clarify the required targets and justify the feasibility of proposed algorithms. Most of the presented case studies are executed through MATLAB and Simulink simulation environments.

1.2. Wind turbine concepts

The first step in analysing the performance of a certain WT is to construct a suitable model that delivers the proposed targets of the planned investigation. Literature classifies WT designs into four major types (as shown later in Figure 2.1 [5, 12]). The major difference between the four types is the ability to control the WT rotor speed, and hence maintain the output power at its optimum value at the incident WS. For example, a double-fed induction generator (DFIG) offers a flexible speed control in the range of ±30% from the WT rated rotational speed [13]. In contrast, the fully-rated converter WT has an extended range of rotational speed (GƆ) variations that harness higher amounts of harvested wind energy at an expanded WSs spectrum. However, the DFIG is still the most widely integrated type in modern WFs, as it combines technical superiority and economical affordability.

The basic idea used in variable speed WTs relies on the role of the power electronic converter which manages the flow of active and reactive power to the grid, and tracks the optimum GƆ relative to instantaneous WS (this technique is known as maximum power tracking (MPT)). Further explanations are provided in the next chapters to emphasise the relation between GƆ, WS, and output power. In addition, one of the most challenging issues in enabling wind energy integration is the correct matching between the characteristics of WSs in the intended location, in addition to the landscape features, and the suitable number and size of installed WTs. In fact, WT manufacturers provide the market with different ratings and sizes of WTs to cope with the different technical and financial requirements of related authorities [14].

The inclination angle of WT rotor blades, known as the pitch angle, is the second factor that can be utilized to drive WTs through normal and fault operation conditions. The role of the pitching

mechanism is to change the angle of attack of the rotor blades on the wind stream, which has a serious effect on the WT mechanical output power (PWT_m) [5]. Pitch control was mainly introduced to protect the WT generator (WTG) from any possible excess mechanical input power from the WT during high WSs. Increasing the pitch angle (β) reduces PWT_m, therefore it is activated only when the WS is beyond its predetermined rated value. In addition, pitching control makes the WT mechanical structure able to withstand extremely high WSs until a braking system is triggered, and in this way, the pitching mechanism protects the WT from undesired additional wind power or tower vibrations. Although, this electro-mechanical system has some drawbacks, it has proven to be more practical compared to the normal stall techniques that were used in the early generations of WTs. The mechanical part of pitching control is always executed by servomotors, which are derived by PI or PID controllers (Figure 1.1 shows the WTG construction and major components).

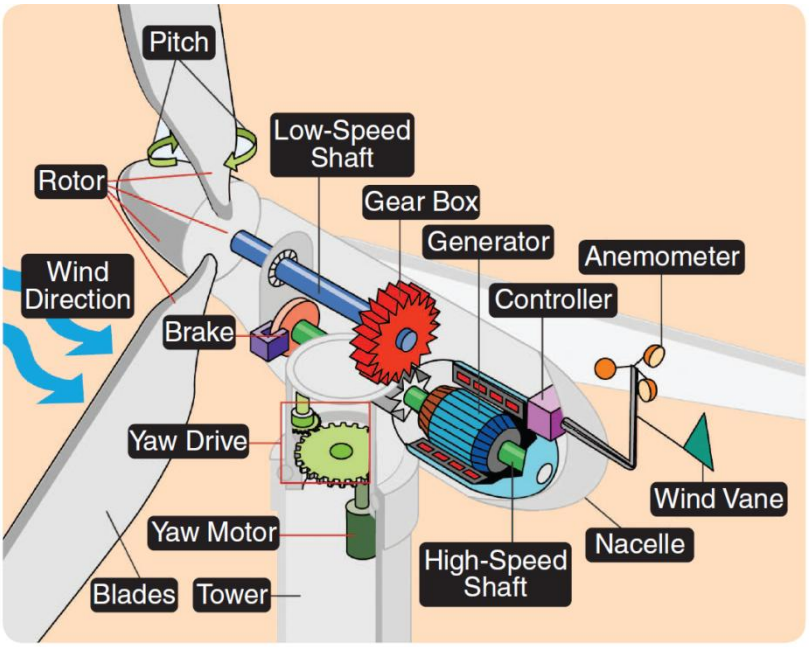

Figure 1.1 Wind turbine construction and components [15]

1.3. Wind speed model

Literature considers variations in WS from two different perspectives. The first perspective considers each case study at a fixed WS and then performs several case studies at different categories of WSs. The second perspective is highly interested in examining the impact of instantaneous WS variations within a defined time step. Rationally, a shorter time step enhances the creditability of the obtained results and emphasises the influence of wind energy integration in a clearer manner. Therefore, WS data recorded at a given site where a certain WF is proposed to be built or studied is of extreme importance. However, the degree of available WS measurement details (e.g. measurements performed at different elevations, short time intervals, and using highly accurate tools) is highly related to the planned analysis and the budget assigned for such measurements [1]. When the WSs are measured within long time intervals (maybe on a scale of hours), a suitable algorithm is required to obtain

artificial arrays at a higher time resolution (for example 10 or 20 s), in order to fit with the power system frequency performance analysis.

The other branch of WS variation modelling is related to its measurements inside a WF. In other words, the magnitude of the WS at each WT inside a WF is the subject of continual debate. The most dominant and simplified assumption ignores any deviations between WS values all over the WF area, and represents the WF as a single WT with a rating that uses a combination of readings from all the installed WTs. However, this assumption is only valid if all WTs are typical, and it causes a moderate reduction in the accuracy of obtained results. In contrast, other studies focus on the shadowing and wake effects and their impacts on the amount of instant power generated by a WF. Several methods with complicated equations and approaches are available to consider such effects in simulating integrated WFs through the prediction of incident WS values at each WT [16]. Generally, most literature agrees that by considering only the annual average WS at a certain site for use in further studies, a very poor approximation is rendered, yielding irrelevant results. This research work therefore offers a detailed classification of available WSs at the WF concerned, and uses associated case studies.

1.4. Research objectives

The main target of this research work is the elimination of any possible negative impacts on frequency support, caused by WFs in replacing conventional generation units. Further, this work also focuses on the ability to operate a WF in a similar manner to a conventional power plant and to predict the impact of newly integrated wind energy on a given power system. Several models and algorithms are proposed, and these are integrated and analysed to reach simple applicable methods with reduced errors. The following steps are amalgamated:

- WS data are gathered, examined, and filtered so that they are applicable to the intended studies. WS generation mechanisms are applied at this stage to convert the available WS data into artificial data with a higher time resolution.
- The relation between stored KE in the WT rotating parts and WT speed is investigated. The first support algorithm causes the WT to over-speed according to the instantaneous WS, so that a certain amount of stored KE is maintained. This extractable KE is utilized to deteriorate any frequency drops suffered by the power system through an innovative support algorithm.
- The electrical power control is involved in the second support algorithm. The WT is de-loaded or decelerated or overloaded based on the WS conditions before and during the frequency event. Numerical values of some of the parameters are pre-determined and then fixed according to the WS nature and the installed WT types at the WF.

These parameters master the proposed support algorithm in both operational modes, namely, normal operational mode and support mode (i.e. when the frequency drops).

- The two previous algorithms are compared with the standard MPT mode from the point of view of performance curves and wasted energy. They are also compared to the default de-loading technique widely offered in literature. Thereafter, a brief discussion of the advantages and disadvantages of the support algorithms is conducted.
- A rough estimation is given for the annual wind energy expected from a certain configuration of WFs and WTs. This assessment is conducted when the WTs are operating in normal mode of the second support method. Proposed methodology utilizes the chronological annual WS data at each WF site in the Egyptian case study.
- Dispatching the power of WF during frequency events is considered to organize the WTs contribution in mitigating frequency drops. In particular, the major task of dispatching is to manage the switching process of WTs groups inside each WF, between normal and support modes of the proposed algorithms. The dispatching technique concedes fixed and variable parameters, such as the capacity of WF, and the incident frequency drop and WS magnitude.
- Finally, energy storage stations are integrated as an alternative for controlling WTs using special support algorithms. A novel method is then proposed to estimate the capacity of each storage bank connected to a particular WF. An appropriate approach is presented for managing energy charging/discharging procedures.

It is worth mentioning that, there are minor and secondary objectives were also considered, as these were essential in performing the previously stated foremost objectives. Some of these minor objectives are described as a consequence of the related major objectives.

1.5. Thesis layout

This thesis is composed of nine chapters. The following chapter presents an expanded technical survey for the topics related to the performed research, and in particular in relation to the WT modelling and control, ride through and support algorithms for frequency events, WSs data, and WFs' aggregation methods. Chapters 3 and 4 present two different algorithms that ensure the positive contribution of the WT in the curtailment of frequency excursions. Chapter 5 proposes a comparison between the offered operation algorithms and standard operation from the point of view of wasted energy. Chapter 6 estimates the expected annual energy production of a selected group of WFs in Egypt, based on real chronological data for load demand, conventional generation, and WS. Chapter 7 describes a novel

method for dispatching power from WTs inside a WF during frequency drops. Clustering techniques related to dispatching algorithms are also explained in this chapter. Chapter 8 then highlights storage batteries as an alternative solution to the proposed support techniques. Finally, Chapter 9 concludes and presents short recommendations based on the obtained results. In addition, it highlights future topics for research.

2. Wind energy integration in power systems

The potential use of a substantial amount of wind energy in power systems poses numerous questions, obstacles, and difficulties that require wise and rational dissection. This chapter highlights such basic issues and emphasizes remediation in relation to this field of research addressed in recent literature. It also addresses major topics related to wind energy generation and integration, and these are combined with the objectives of this thesis.

2.1. Wind turbine concepts and modelling

Providing a feasible and realistic analysis for any component or system requires a robust, clear, and detailed simulation model. The level of required details depends on the nature and aims of the planned study, and therefore, certain parameters can be ignored to simplify computational efforts and shorten the time involved. In addition, the model differs based on the simulated wind turbine type.

2.1.1. Wind turbines types

In general, there are three well-known types of WT, and these are classified according to their capability of controlling the rotational speed [4]. However, some literature considers the doubly outage induction generator (DOIG) to be an independent type; and hence classifies designs into four types, as shown in Figure 2.1 [12].

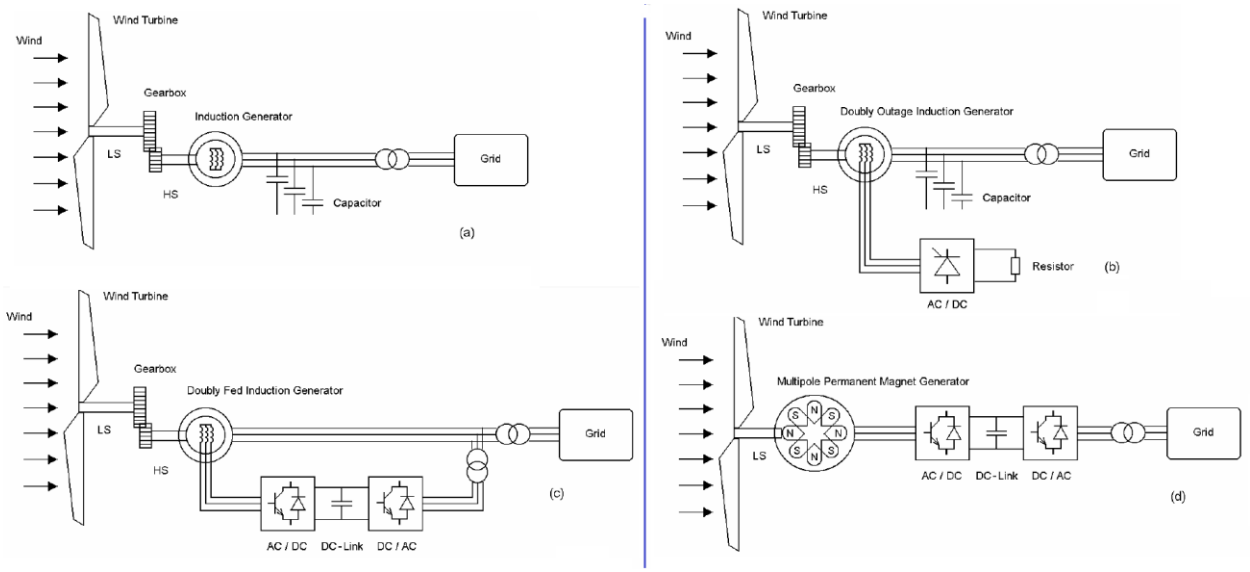

Figure 2.1 Four principal concepts used in WTs [12]

a) Fixed speed squirrel cage induction generator **b) Partial variable speed WT with variable rotor resistance**

c) Double Fed induction generator **d) Full rated permanent magnet generator**

Initial trials in modern WT fabrication produced the squirrel cage induction generator (SCIG) (Type 1) which contained a simplified control algorithm. However, compared to other types of WTs, it wastes more wind energy because it has a fixed operation point and the WT rotational speed is uncontrollable,

and thus, it is unable to track the continuous variations in WS. It relies on a connected capacitor bank to energize the WT (fulfil the machine's reactive power requirements), and maintain connection voltage stability during faults. Additionally, the ratings of the WTG units are limited to hundreds of kilowatts, and it also has certain problems in relation to maintenance and operation. The current dominant and most applicable technology is Type 3. The major advantage of Type 3 is its capability for the tracking optimum operation conditions at each WS. As a further explanation, a compact review of each WT's operational theory is presented.

The physical idea behind a WT depends on converting wind kinetic energy into electrical energy through a WT generator. The output mechanical power (PWT_m) from the WT is evaluated using (2.1):

$$PWT_m = \frac{1}{2} \cdot \rho \cdot C_p(\lambda, \beta) \cdot \mathrm{A} \cdot WS^3 \tag{2.1}$$

The air density (ρ) used is 1.225 kg/m^3 [1], C_p is the coefficient of performance, λ is the tip speed ratio calculated using (2.2), β is the pitch angle and A is the WT rotor swept area in m^2:

$$\lambda = \frac{\omega \cdot \mathrm{R}}{WS} \tag{2.2}$$

The evaluation of C_p depends on the aerodynamic characteristics' of the airfoil of blades. The airfoil design distributes the lift and drag forces implied by wind on the blade, thus the amount of extractable wind energy is determined. However, the maximum possible value for C_p is 16/27 as proved by Betz' law [1]. According to the previous equations, PWT_m variations directly affect generator output. However, there are two main parameters that control PWT_m, namely, λ and β. The control of λ is achieved through G, and control of β is executed using electro-mechanical pitch angle controllers, if the WT is equipped with such a facility [5]. Both parameters are coherently controlled to make C_p follows its optimum pre-determined value ($C_{p\text{-}optimum}$), which differs from one WT to another depending on several factors, for example the size and aerodynamic profile of the installed blades (i.e., default $C_{p\text{-}optimum}$ value is 0.48). The function that describes the relation between the C_p, λ and β, is considered to be an empirical formula with a certain number of coefficients, and it is totally dependent on the rotor blades design and WT characteristics. Equation (2.3) represents a widely applied form for this function in literature, where c_1 to c_6, besides a and b are the related coefficients. Numerical values for these coefficients are simulated in the GE-1.5 MW WT (GE-77) generic model built in MATLAB Simulink power library [17]. A 3-D visualization for the C_p equation of GE-1.5 MW is depicted in Figure 2.2, where the $C_{p\text{-optimum}}$ is 0.48, and it doesn't exceed the maximum theoretical value, namely,

0.593. It is of note here that the author of the current research has made a contribution to this area in relation to the evaluation of C_p equation coefficients [18].

$$C_p(\lambda,\beta) = c_1 \cdot (\frac{c_2}{\lambda_i} - c_3 \cdot \beta - c_4) \cdot e^{\frac{-c_5}{\lambda_i}} + c_6 \cdot \lambda$$
$$\frac{1}{\lambda_i} = \frac{1}{\lambda + a \cdot \beta} - \frac{b}{\beta^3 + 1} \quad (2.3)$$

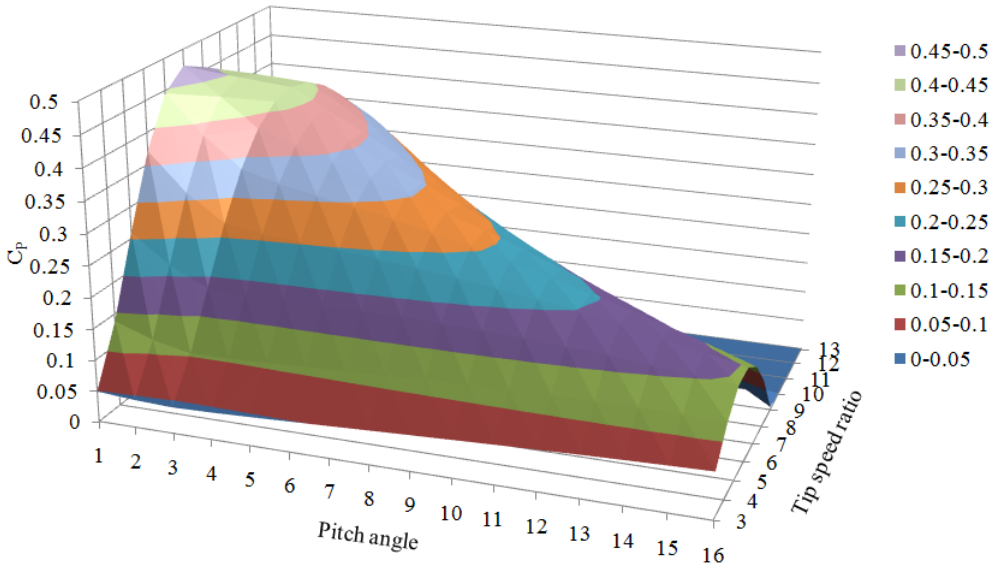

Figure 2.2 3D presentation for the C_p equation of GE-77 embedded model in MATLAB

With reference to the above, and concerning the types of WTs, it is clear that Type 1 is incapable of maintaining a $C_{p\text{-optimum}}$ value at any WS other than the rated WS of the WT. However, Type 3, which is implemented in this research work, offers the ability to track maximum power through *GƆ* control by grid and rotor side converters. However, the range of variation of *GƆ* is limited by the converter ratings and the amount of power that can managed between the grid and the rotor sides. In this case, the WT has a base rotational speed ($GƆ_b$) (measured using per unit (pu) or radians/second (rad/s)). The control speed range is always calibrated based on $GƆ_b$, where the relevant range is 70% to 130% of the $GƆ_b$ [19]. Type 4 was introduced as having a great advantage over the three former types in relation to the absence of a gear box and a full range of *GƆ* variation. The gear box removal solves major problems related to maintenance and operation; in addition, the efficiency of a direct drive WTG makes it superior to the other types. This results in eliminating gear box mechanical losses and reducing the amount of wasted wind energy, because the WTG is now more flexible and able to follow the WS variations. *Anders Grauers* presented an interesting comparison between the efficiencies of the three main WTs types and simplified methods of estimating them [20]. It is worth mentioning that Type 4 has a relatively high cost, and this is the main reason restricting its widespread use and why it

is only installed in large and highly rated WTs (e.g. Enercon-101 3.4 MW [21]). The market shares of the four major types of WTs in 2010 are depicted in Figure 2.3 [22].

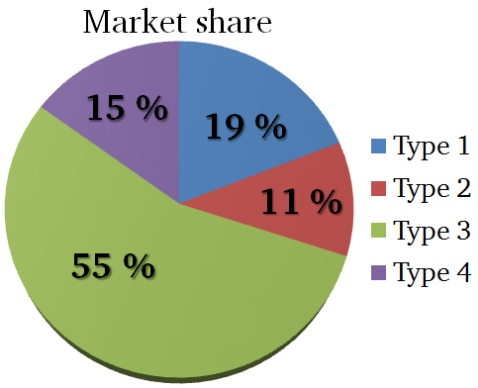

Figure 2.3 Wind power capacity market share of each WT technology

2.1.2. Modelling aspects of wind turbines

Literature divides the WT model into four sub-models, the complexity and level of considered details depend on the study field employing the models. The four sub-models are the WT aerodynamic model, the shaft connecting WT to generator (i.e., drive train) or the shaft model, the generator model, and the pitch angle electro-mechanical controller model. The type of WT only affects the generator model and the method by which this generator is controlled when it is connected to the grid [**7**]. The WT aerodynamic model is usually presented by using the C_p equation previously explained in Section (2.1.1), where this model has three inputs, namely, ω, β, and WS, as well as one output, PWT_m. The shaft model is mathematically presented by a two-mass, as shown in Figure 2.4 or a single mass model. The shaft model receives two inputs (i.e., PWT_m from the aerodynamic model and ω), delivers turbine power, and is essential for use with fixed speed WTGs, but can be ignored in variable speed WTGs (however, it depends on the aims of the study). Disregarding the shaft model in the overall integrated simulated model was a valid assumption in [23], where the method presented describes the connection of a permanent magnet synchronous generator (PMSG) WT through a DC link controlled by a thyristor converter. Although the PMSG is a fixed speed generator, the presence of the DC power electronics-controlled link ensures that the role of shaft inertia is very minor. A third sub-model is constructed to control the pitch angle, and functions using two parts, the proportional integral (PI) controller and the servomotor. The servomotor model is well known and its design is predominantly similar in all literature. However, several designs and methodologies have been proposed for installed PI controllers. Initially, a pitch controller was installed in WTGs to offer an alternative to the normal stalling mechanism, and to extend the operation range of the WT in certain WSs. To understand the possible uses of a pitch controller, it is necessary to look at the WT output power curve vs. WS, as in Figure 2.5. As an illustration, PWT_m continuously increases with an increase of WS until it reaches WT rated WS (WS_r). Beyond this WS, the WT is able to produce a PWT_m higher than the rated power

of the installed generator, and the generator becomes overloaded and damaged if overrated with high ratios over a prolonged time period. To overcome this problem, the pitch controller increases the attack angle of the wind stream, and hence the value of C_p value is reduced too, keeping the PWT_m within an acceptable range for the generator rating. There is therefore no need to stop the WT at WSs higher than WS_r, as the WT operational region is extended to what is known as the cut-out WS (WS_{CO}). It is noted, however, that the value of WS_{CO} is related to the maximum pitch angle that can be achieved by the rotor blades (i.e., theoretically 90°) [5]. In addition, WS_{CO} is employed to avoid any extra mechanical stresses either on the WT mechanical components (the gearbox and drive train) or the tower carrying the whole WTG assembly [24].

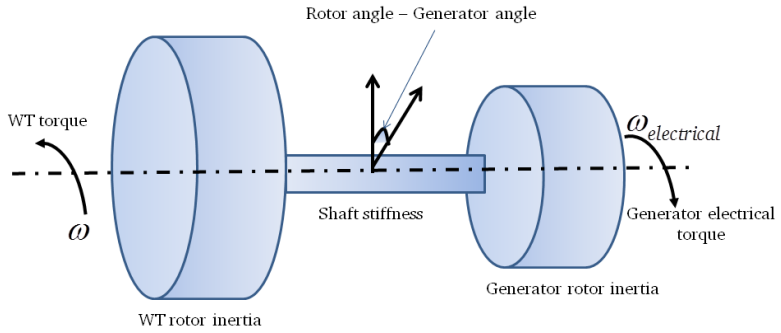

Figure 2.4 WTG shaft two-mass model

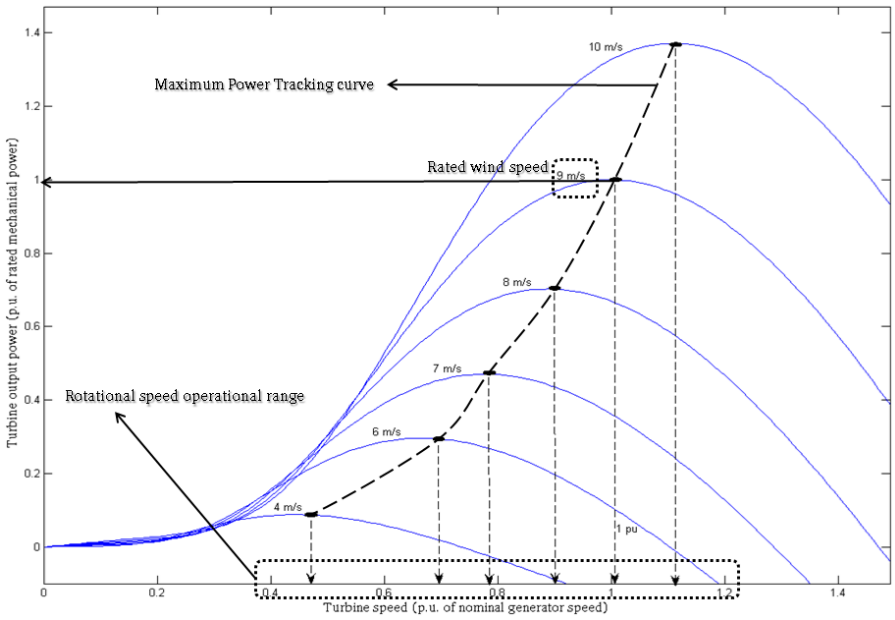

Figure 2.5 WT output mechanical power at MPT operation (β = 0)

The simplified pitch controller receives a single input signal (PWT_m), and this input is then compared to a reference signal (i.e., in default operation it should be 1 pu equivalent to WT rated power (PWT_r)). Afterwards, the deviation signal is processed through the PI controller to evaluate the required new β, which is considered as the lone input signal for the servomotor responsible for the rotor blades' adjustment. However, this method has a weakness in relation to the ability to define an accurate measurement of PWT_m [25]. Some research has attempted to solve this defect by estimating PWT_m through an aerodynamic WT model, and by the measurement of instantaneous WS. In this study, the

dependence of the estimation of β on PWT_m proved to be inaccurate, and produced an undesired oscillatory response in the WT electrical output power (PWT_e), as discussed later in Chapter 6 [26]. The enhanced aspect of pitch angle regulation is realized by inserting a second input control signal, namely, the deviation in $G\mathcal{O}$ ($\Delta G\mathcal{O}$) from its reference value, which depends on the activated operation mode (i.e., normal or fault mode). Compensation for any errors caused by the power deviation was the main reason for the new signal introduced in [27]. This type of controller integrates two independent PI controllers; each one is responsible for one of the input deviation signals, as shown in Figure 2.6. It is worth mentioning that all these signals are in pu so that it is possible to add the PI outputs algebraically to evaluate the new β value required for execution by the servomotor. The dynamics and speed of response of the mechanical parts of the pitching system play an important role in the PWT_m. However, new types of servomotors provide very fast rates of pitch angle change, and can reach approximately 10 degrees/s [27] (a typical servomotor model is shown in the Appendix). Finally, the generator model is a complicated model that includes the converter and their controllers. This research work focuses on the DFIG; hence, the modelling approach of this type is briefly discussed in the next lines. Control of the DFIG is more complicated than control of a standard induction machine, as the mechanical power driving this machine is based on WS, which is a highly unpredictable source. Likewise, the connection of various types of loads can cause the electrical system to be under constant stress, which can severely affect the DFIG if no appropriate control is in place.

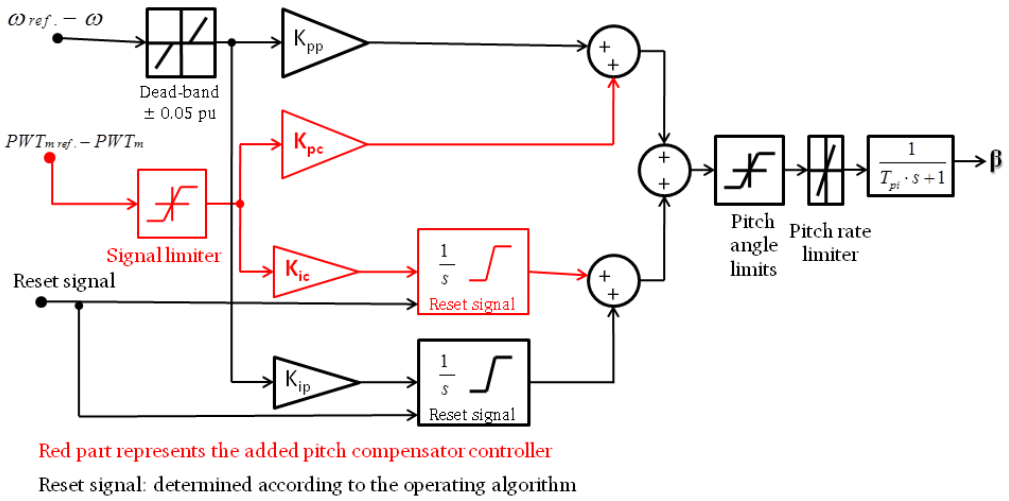

Figure 2.6 Enhanced pitch angle controller

All generation units have two major outputs, active and reactive power. In the DFIG, the generated active power can be controlled either by controlling the input PWT_m or by using the $G\mathcal{O}$ control. In both cases, a power electronics converter (PEC) is the link between the imposed control technique and the generator model. In relation to reactive power, an induction generator requires a reasonable amount of reactive power for its operation. In case of grid-connected systems, the generator obtains reactive power from the grid itself. This is done by operating grid side converter at unity power factor, and then rotor side converter provides the required reactive power. However, the isolated system operation needs an external source of reactive power such as external capacitors that are connected to the

machine rotor through PEC. In special cases, capacitors are replaced by an external source (i.e., batteries). In the case of a grid connected DFIG, the main task of the DC link capacitor shown in Figure 2.7 is to maintain the AC voltage of the grid-side converter so that it is equal to nominal grid voltage [13, 28]. Most of the research work related to voltage stability studies has implemented a detailed vector model of a generator, known as *d*-*q* model. This highly complicated mathematical model is of a great importance to electrical engineers involved in PEC and DC link voltage studies.

Although this thesis research work concentrates on frequency stability through injected active power, it is however essential to briefly mention the *d*-*q* representation system used to model the DFIG converter, in addition to stator and rotor voltages and fluxes. Such a compact summary related to this topic is presented in the second section in [29, 30, 31]. Usually, the *d*-axis of reference frame is defined in the direction of the stator flux space vector, which is evaluated based on stator voltage and current measurements, and the *q*-axis leads the *d*-axis by 90 degrees. Given the amplitude of the stator flux linkage, the rotor current component in the *q*-axis is approximately proportional to the air-gap torque developed in the machine. However, the *d*-axis current component decides the reactive power at the stator side. The *q*–axis current demand is obtained from a quadratic relationship between the desired torque and the rotor speed, which is used as an input signal to the converter controller. Proportional and integral control is applied in both axes to derive the reference voltage for the converter. The rotor current components (i.e., the feedback in the control loops) are calculated using the measured phase quantities, according to the default (abc) voltage sequence, projected to the *d* and *q*-axes taking into consideration the rotor angle.

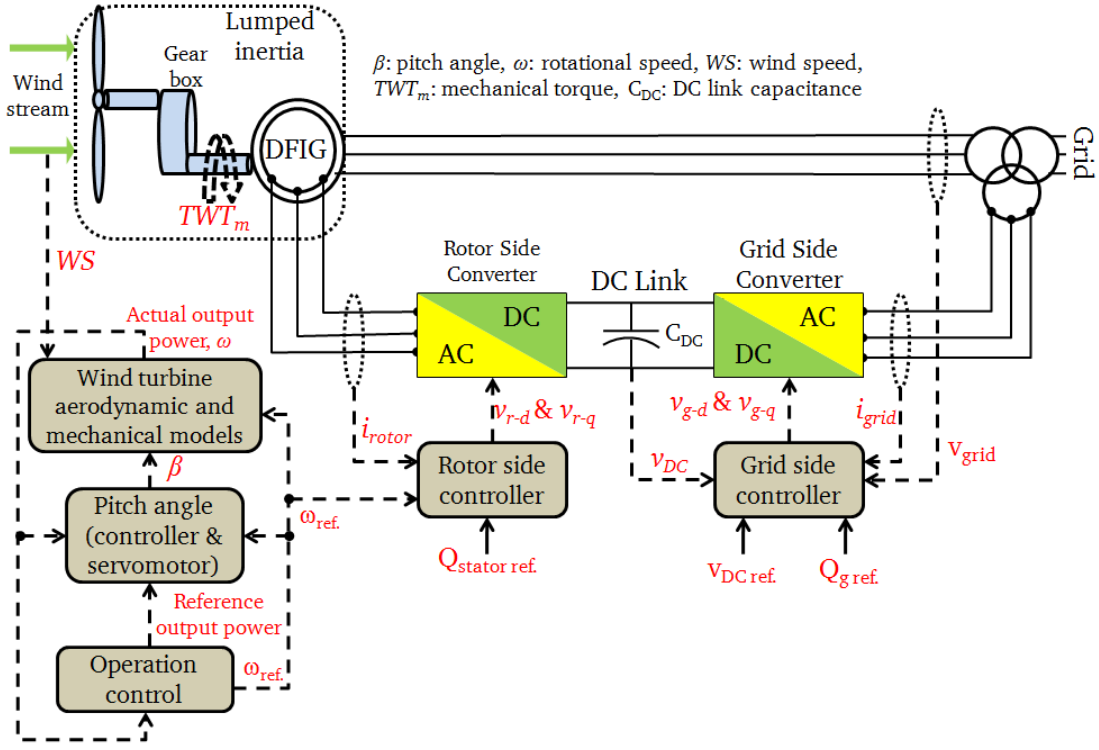

Figure 2.7 Compact model of WTG Type 3, using d-q frame reference system

An innovative criterion presented by *Padrón*, applies the Newton Raphson iterative method to propose two possible WTG models for load flow analysis, namely the active-reactive power bus (PQ) and the active power-voltage bus (PV) [32]. In such way, a WTG, or even a complete WF, can be treated in a similar way to a conventional generator. The main idea is based on assuming that the WT or WF bus is the only unknown bus in the system, whereas the bus type differs based on the implemented method. Thus PWT_m equals P, and the voltage vector is then estimated using an iterative method (in the case of PQ), and likewise Q and the voltage angle are estimated in the case of the PV bus. This work has considerable additional strength in that it does not use the complicated d-q reference frame. However, if more than one WF is connected, these two methods have drawbacks concerning WS prediction complications and WS measurement accuracy. In addition, the WS is calculated using back substitution according to required aggregated power. In other words, the load flow analysis determines the optimum incident WS to satisfy the system requirements. This concept is hard to apply in dynamic analysis, but is practical and simplified when it comes to steady state load flow analysis and DFIG initialization.

Based on the previous brief background, the merits of DFIG can be summarized in four points: 1) it delivers reduced wasted wind energy; 2) the mechanical loads are less and it delivers a simpler pitch control; 3) the controllability of both active and reactive power to achieve near-independency; and 4) oscillations in output power are mitigated.

2.2. Wind turbine operational modes

This section reviews the main WTG operational theories widely offered in literature. The design of such operational methodologies depends on the desired aims, or on the nature of the problem to be solved. Categories of operational methodologies can be summarized by the use of three general approaches: maximum power tracking, low voltage ride through algorithms, and frequency drops ride through and support algorithms. However, it is extremely difficult to achieve these three targets together with a level of adequacy; hence, a compromise is made between them to reach an acceptable solution matching the prerequisites of the involved power system. Because this thesis is oriented to solve frequency drops problems, a separate subsection discusses this approach (Section 2.3).

The current dominant operation algorithm for integrated WTGs in power systems aims to minimize any wasted wind energy. Therefore, this operational mode adjusts the controllable parameters in WTG to match the intermittent nature of the WS. In fact, this operation algorithm tries to provide $G\mathcal{D}$, which achieves $C_{p\text{-optimum}}$, and in turn maximum values of PWT_m [6]. Applying this technique produces an operation curve, which shows a set of different operational points of the WT concerned at WSs less than WS_r, as shown in Figure 2.5. This operational mode implies a zero degree pitch angle because all operational points are below WS_r. In this case, the controller is responsible for providing the reference rotational speed signal and the related PWT_m fluctuations, which act as an input to the rotor side controller, as described in Figure 2.8. *Meng* made an influential modification in the MPT curve to

improve its accuracy [**33**], whereby the offered concept splits the MPT curve into four different regions. The two extremes of this amended curve are zero and ω_{max}, and in between there are two newly defined speeds, namely, ω_b and ω_c as shown in Figure 2.8. Comparatively, two intermediate WSs are defined, WS_B and WS_C, whereas WS_{CI} and WS_{CO} are the two extremes. The linear region equations are evaluated using (2.4) and (2.5), while the non-linear curve between points B and C represents the function between PWT_m, WS, and C_p, as explained in Subsection (2.1.2). This modification improves the estimation accuracy of PWT_m at each WS. It is of note that each WTG has a family of curves, whereas each pitch angle is presented by a curve that has the same structure, but the points are shifted due to the changes in the C_p equation according to the pitch angle value.

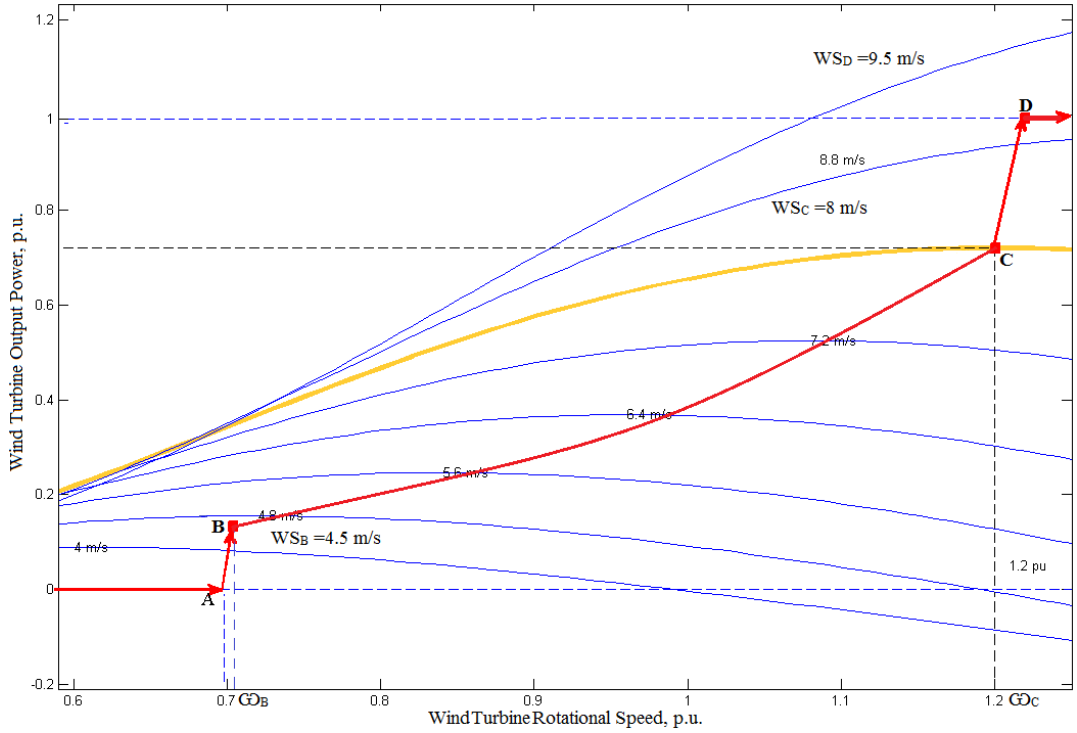

Figure 2.8 Modified normal operation curve with four regions

$$\omega = \left(\frac{\omega_B - \omega_A}{\mathrm{PWT_{m\text{-}B}} - \mathrm{PWT_{m\text{-}A}}} \right) \left(PWT_m - \mathrm{PWT_{m\text{-}A}} \right) + \omega_A \tag{2.4}$$

$$\omega = \left(\frac{\omega_D - \omega_C}{\mathrm{PWT_{m\text{-}D}} - \mathrm{PWT_{m\text{-}C}}} \right) \left(PWT_m - \mathrm{PWT_{m\text{-}C}} \right) + \omega_C \tag{2.5}$$

One interesting study examines the impact of different possible ranges of rotor voltage adjustments within the *d-q* modelling technique on the slip of a connected induction machine [34]. The main target of this study was to derive the extracted power as a function of the slip, the number of poles, and the ratio of the installed gearbox. The most attractive results were as follows: 1) $V_{r\text{-}d}$ is more suitable for use in machine control because it pushes the slip to the stable zone, 2) an increasing number of poles

leads to a wider stable operational range for the slip, and 3) increasing the gearbox ratio displaces the slip from the sub-synchronous region to the super-synchronous region. An advanced current control method is proposed by *Hu*, where both sides of the DFIG converter currents are controlled to mitigate third order harmonics in the WT generated electromagnetic torque during unbalanced grid voltage conditions [30]. This proposes a novel control scheme consisting of a proportional controller and a harmonic resonant regulator tuned at grid frequency. However, this research track is specialized for detailed control issues and their integration with PECs.

2.3. Wind turbines ride through and support algorithms

In relation to the wide research presented in this chapter, this section is mostly related to the core of the proposed algorithms and the associated research work described in this thesis. The ride-through algorithms are classified into two categories; low voltage and frequency drop ride-through algorithms (LVRT and FDRT respectively). Using an analogy with conventional units, LVRT depend on special reactive power and DC link voltage control techniques [35], whereas, FDRT build on controlling the PWT_m, mechanical torque (TWT_m) and/or the reference electrical power signal fed to the converter-generator controller (PWT_e). Frequency support algorithms are also related to the control of active power generated by a WT during frequency excursions. The major target of these algorithms is to provide an extra amount of active power from WTs in the case of frequency events, to accelerate the frequency drop elimination process. The next two subsections summarize the latest concepts in relation to LVRT and FDRT algorithms offered in literature. However, the focus is centred on frequency support, as this thesis is directed towards this research point.

2.3.1. Low voltage ride through – methods and aims

The possibility of a WT disconnecting under voltage drops depends on the location of the fault with respect to the point of common coupling (PCC), the drop duration, type and severity, the method of reactive power compensation, and the control algorithm of the WT. Most of the proposed solutions wander in the orbit of compensation or dissipation of the missing or extra KE caused by the voltage drop or rise. This can be executed by the wise control of rotor side currents, WT rotational speed, and the pitch angle [36]. LVRT research work is interested in detailed dynamic modelling for WTs and WFs; hence, the *d-q* reference frame is implemented. The DFIG has a unique advantage concerning its ability to control active and reactive power almost independently, which facilitates the task of providing excess reactive power during voltage dips [8]. The rotor current is controlled in such a way to reduce any DC link voltage ripples, especially during system voltage events [29]. However, the DFIG provides no support to mitigate the voltage drops, but the negative impact of wind energy integration is reduced. Another study proposed novel methods of connecting WTs to the grid. This method improves the voltage imbalance compensation, as voltage is injected in series with the transmission line to limit the fault currents as well as to balance the voltages [37]. The modifications are implied only on the grid side converter; thereupon, it is connected in series instead of parallel

installation. Additionally, the three-phase converter is replaced by three single-phase converters. Each converter is responsible for a certain regulating task, for example, the phase 'A' converter compensates for the voltage imbalance. Generally, when a short-term low-voltage fault occurs, the sudden imbalance between wind energy and injected electrical energy leads to transient excessive currents in the rotor and stator circuits. Therefore, suppressing the over-currents in the rotor and stator circuits should reduce the imbalanced energy flowing through the DFIG system. To achieve this suppression, the excess KE provided by the WT can be dissipated by accelerating the WT rotational speed by controlling the rotor side converter [28]. Similar work is applied to PMSG as well as DFIG WFs, to maintain rotor currents and DC link voltage levels [38]. The major change is that it reduces the active power fed by the WTG proportional to the incident voltage dip. Far from control algorithms, an integrated component called crowbar protection could be used to enable survival of the WT through such an event. A simplified explanation of the role of the crowbar, accompanied by a detailed case study using a hypothetical test system, is described in [39]. It is of note that voltage stability studies are not able to ignore transmission lines and transformers models, as shown in the considered case study in [39]. This highlights their influential impact on the accuracy and relevance of the obtained results, as they affect the reactive power flow throughout the whole system. This work emphasizes the role of the crowbar in causing the DFIG to behave as a conventional SCIG, when its controllability is temporarily lost. In the same vein, crowbar resistance is operated for a shorter time in the proposed strategy by [40], so that there is a shorter interval where there is no control on the DFIG. In addition, the energy losses in the crowbar resistors are mitigated. The proposed strategy is based on increasing crowbar resistors to a certain value that is a multiple of rotor equivalent resistance. The compensation for the short crowbar connection time is made through demagnetization of the stator; hence, the current oscillations are attenuated. A simple demagnetization method is applied through setting the reference signal of the rotor current's two components in the *d-q* frame to zero. However, this work is highly oriented to power electronics and machine theory, and is therefore very complicated to integrate with expanded power system analysis. In addition to the above, the crowbar is triggered for an interval 50% less than its usual duration, without adding any external devices [41]**.** In usual operation, the crowbar is released after a certain fixed time, where half of this time is implied to guarantee that the reference signals of the rotor side converter settle down to acceptable values. The research work in [41] eliminated this duration by applying a predetermined reference signal to the rotor side converter, taking into consideration that these signal values yield a reasonable power factor. However, these imposed values are provisional until real values are obtained; nevertheless, the earlier re-connection of rotor side converter is achieved. In the light of previous discussion, the aims of any LVRT can be summarized as follows: 1) to minimize the voltage drop at the generator through demagnetization techniques, 2) to divert or negate any rotor overrated currents to avoid damage to the converter, 3) to produce appropriate power during faults where the DFIG controller limits the rate at

which apparent power control can be restored during fault initiation and recovery. In such a way, DFIG compliance with the grid-code is fulfilled.

2.3.2. Frequency drops ride through and support - methods and aims

At present, WFs do not play a fundamental role in eliminating system frequency events, as most grid codes do not force them to provide any support during frequency excursions. However, in order to allow high levels of wind power penetration, system operators (SOs) will eventually require wind generation to have frequency control capabilities in future updated codes [42]. For example, SOs in Ireland are attempting to solve operational and infrastructure obstacles so that WFs cover 37% of the electricity demand. The outcomes of the 2010 Facilitation of Renewable (FoR) studies predicts deficits in system performance capability in terms of frequency control by the year 2020, as a greater number of the non-synchronous generation become integrated in the system. In terms of frequency control, analysis has shown that projected levels of synchronous inertia that will be available in 2020 will be less than amounts needed to meet system requirements.

Frequency control becomes more challenging at high wind energy penetration levels. As an illustration, the rate of change of frequency (ROCOF) protection relays shut down WTs under certain scenarios. Investigations are currently under way to either replace ROCOF protection relays on the distribution networks with alternative protection schemes or to increase ROCOF thresholds [43]. However, the main challenge is related to the supportive contribution of WFs during frequency events. Positive frequency deviations do not cause a critical influence, as they are always the result of a mismatch between generation and load demand where the generation rises suddenly beyond required load. In such scenarios, a portion from the WFs is disconnected according to the system status, and the WFs reconnection is then decided based on the system's new stable operation conditions. These manoeuvre methods have also been investigated to determine the optimum amount of disconnected wind energy according to the characteristics of frequency overshoot events and other factors [6]. However, when a system suffers a frequency drop, WFs are requested to compensate the deficit between generation and demand, similar to conventional generation. Conventional generators have governor controllers at different levels of complication and accuracy, and these provide a control signal to the source of mechanical power, the turbine, which in turn drives the synchronous generator shaft. For example, in steam generators, the most dominant type in conventional generation, the mechanical power is determined according to the flow rate of steam exerted on the turbines vanes. Thus, the governor controls the valve opening, such that the required flow rate of steam is injected to the turbine [10]. The governor operation is based on two major signals: the electrical power demand and the instantaneous frequency deviation (Δf). The Δf signal is responsible for the generation unit dynamic response in case of frequency excursions, whereas the droop parameter makes links between the amounts of increase/decrease in generated power according to the incident drop/rise in frequency deviation. The numerical value of droop ranges from 5% to 10%, for example if droop = 5% this means that for each 1 Hz change in frequency, the unit output changes from its capacity by 5% [44].

It is an essential prerequisite to find an acceptable method that guarantees the positive contribution from WFs during frequency drops, especially when WFs replace conventional units and penetrate power systems at high levels. The intermittent nature of WSs is the major obstacle facing electrical power engineers in this field, and in comparison with fuel used in conventional units, *WS* is unpredictable and cannot be controlled. For example, in a steam plant, the flow of steam is available and controllable at all times, as long as the fossil fuel used to produce the steam is available. Hence, the SOs perform previews of system operation, and expect certain reactions from these units during fault events. Such an advantage is completely absent in the case of WFs, because they completely depend on the coincidence between frequency drops and the nature of *WS* during the drops. For example, if a WTG is connected to a standard governor, such as the one connected to a conventional unit, which then orders a certain output from the WT, but the *WS* is insufficient to satisfy this reference output power, it is necessary to ascertain feasible solutions for such a dilemma.

Another challenge is related to the reduced inertia of power systems after the installation of WFs. Extended research has proven that grid inertia in seconds (H) is notably affected by the integration of WTGs. This negative impact is more remarkable in cases of variable speed WTGs [45]. The interpretation of this phenomenon depends on a comparison between synchronous generators used in conventional units and variable speed WTGs, whereas the fast response of WTGs, caused by the great developments in upgrading the speed of PECs technologies to milliseconds, makes the WTGs inertia-less [46]. This problem is partially overcome by using fixed speed WTs, but this reduces the harvested wind energy and WT efficiency [47]. It is of note that the inertia of conventional generators ranges from 3 s to 8 s, based on generator type and capacity [48]. The solutions offered in literature are concentrated in two directions: 1) running the WTG in an analogous manner to conventional units by defining a special droop controller [49]; 2) imposing virtual inertia to the WTG through unique control algorithms [50]; and 3) utilizing several types of storage banks to smooth WFs output, using the available stored energy. The storage process occurs when the generated wind energy is rejected by the system during trough load periods [51]. Expanded explanations and discussion concerning these solutions are presented within the next related chapters. The implemented concept to simulate the frequency response of the test systems in the next chapters is based on the aggregate bus criterion as explained in [52] [53]. The illustrative Figure 2.9 highlights the major four sub-models, namely, the conventional generation aggregate unit(s), the dynamic load, WF(s) and the system aggregate inertia. Actually, the most effective component of a conventional generation unit on frequency are the controller that sets reference power, the governor and the turbine as discussed in [52] [53]. The load dynamics are presented by load dependent and independent components with respect to frequency variations. The WF is composed from four major blocks, firstly, the operation algorithm that is responsible for setting ω, reference output power and pitch angle, as well as some special signals which differ from one algorithm to another. Secondly, the aerodynamics which determines how much mechanical power is extracted from wind power, thirdly, the mechanical model represented by Euler's

equation as shown later, and fourthly the dispatching and WS propagation method. Integrating the generated power and load demand through the proposed detailed model provides the system aggregate frequency response within certain duration. It is worth mentioning that each aggregate conventional unit represents a different type of generation (e.g., hydro or steam). In addition, all the signals are per unit to be sure that the response of several units having certain rated power is equivalent to the output of a single unit but with aggregated value (i.e., as long as the those are identical in their components and parameters). The losses, deviations, and delays caused by power electronics' devices are ignored.

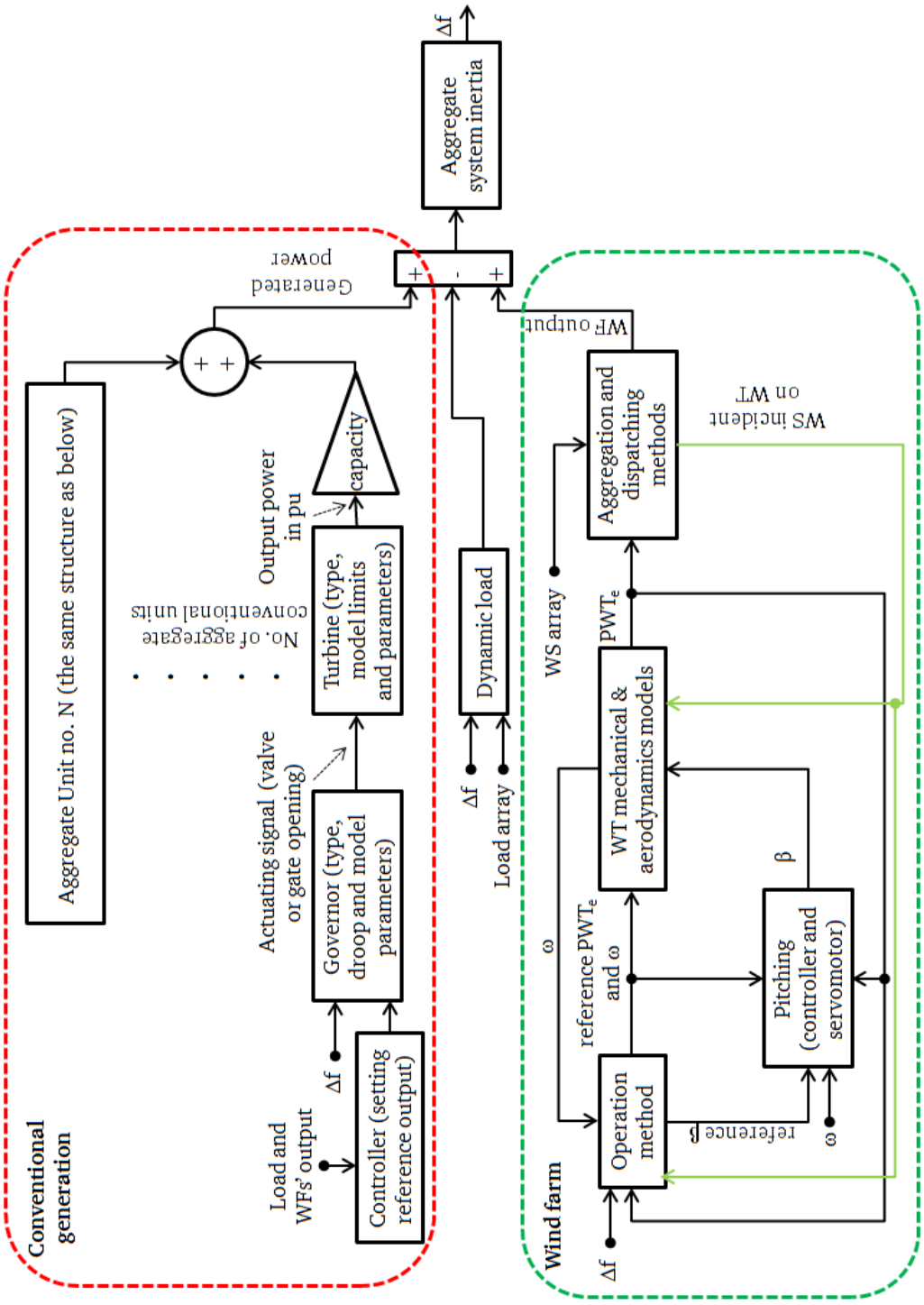

Figure 2.9 Major block diagrams of the implemented model of frequency investigation

As an illustration, the losses of power electronics are no more than 0.75% [54] and the time delays are in range of milliseconds. In addition, the reference signals and actual signals are almost typical (i.e., trivial deviations that do not affect the accuracy and the nature of proposed investigation) [55]. The aggregation and dispatching approaches are discussed later through the next subsections and also in each chapter according to the implemented case studies.

2.4. Wind speed prospects and simulation

The pre-assessment for wind energy integration in power systems is highly based on the accuracy and reliability of the integrated *WS* data and records, and the *WS* value is involved in the frequency studies in two ways. The first way considers a fixed *WS* in each case study, and the same case is then repeated at different levels of *WS* (low, moderate, and high). The classification of these WSs categories is mainly based on the WS_{rated} of the installed WTs [11]. The second approach acknowledges the dynamic variation of WS within the time frame of the case study [56]. This second approach is highly complicated and needs more computational efforts and a longer simulation time. However, the obtained results are always more accurate, especially in case of frequency drop studies. Literature utilizes two types of WS data: the recorded WSs in the WT or WF location, and different prediction and forecasting mechanisms for WSs. At times, the measured WSs are recorded in a low time resolution (i.e., there is a long time step between each two successive records as illustrated in Figure 2.10), but results do not then fit with the planned research targets. To overcome this problem, techniques for generating WS arrays are widely used to obtain modified WS arrays with higher time resolutions (e.g. few seconds). In particular, onsite recorded WSs data are implied in a WFs capacity evaluation, and the selection of WTs that match the WS conditions in a WF [57].

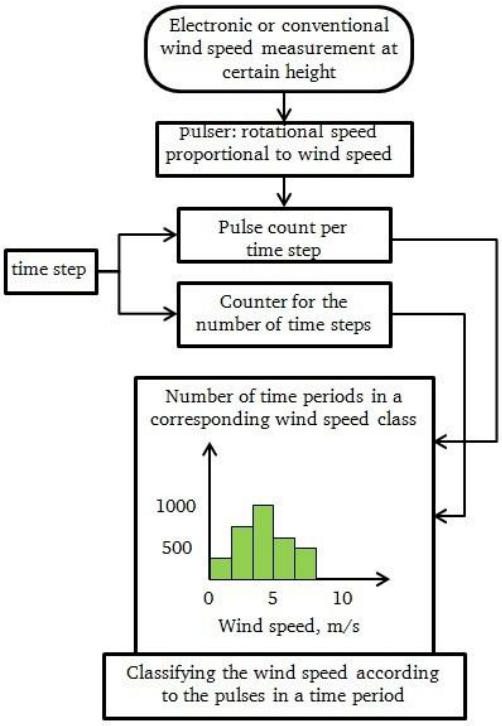

Figure 2.10 Wind speed classification process

Most research work interested in the reliability optimization of power system expansion tends to implement the Wei-bull probability distribution of WS. This distribution describes the occurrence probability of several categories of WS within a year. However, these studies require fresh WS data and their results are only guaranteed for a short time period [58]. Novel and comprehensive efforts in the field of wind power assessment based on WS time series prediction are offered in [59], where four different methods are investigated to predict the output power of a WF composed of 100 WTs. Firstly, a suitable 10 min WS series and an applied method were selected to forecast multiples of WS series at a point 10 min into the future. The same procedure was repeated for an hourly time series, and as expected, it proved to be less accurate. A tangible idea is performed using neural networks, as presented in [60]. The applied neural network was moderately complicated with five input delays, one hidden layer, five neurons in the hidden layer, and 100 training iterations. However, neural network integration is out of the scope of the research work presented in this thesis, but is considered as a topic for possible future work. Far from planning and previewing system performance before actual wind energy integration, other efforts have been directed to exploiting WS prediction techniques in the curtailment of WTs output power fluctuations [61]. The wind model used was a stochastic model from a certain block set for Simulink, which uses a white noise generator and filters to represent the main wind source, and another noise generator and filter for turbine tower shadowing effects. Additionally, WS is assumed to vary between one WT and another at the same instant, but this point has greater relevance to the information presented in the following section.

2.5. Wind farm aggregation

It is initially important to highlight the motives for investigating this issue. As previously stated, WS is the ‘fuel’ that runs a WTG; hence, all related concepts and facts pertaining to WS need to be covered and studied to achieve acceptable results in previewing, operating, and simulating WFs. It is impossible to say that concurrent WSs are identical in two different locations, even if such locations are only hundreds of meters apart. Therefore, claiming that all the WTs inside one WF facing the same WS magnitude and direction is a special approximate assumption. In addition, towers with a WTG assembly cause shadowing effects. These effects reduce the WS during its propagation in the WF, in comparison with the WS magnitude that reaches the first WTs at the WF. The influence of shadowing and wake effects is related to several parameters: tower height, land roughness coefficient (k_w), and the spacing between two successive WTs that impede the free WS stream [16, 62]. It is of note that these effects impose a time delay between the different streams of WSs propagating inside the same WF. For example, the WS at the first WT that is facing the initial wind stream, which reaches the WF, is ahead in time of the wind stream projected on the blades of the last row of WTs. This time delay depends on the spacing between the rows of WTs, and the wind stream’s initial WS just before passing through the WF [63]. Electrical power engineers have therefore been encouraged to propose a wide spectrum of solutions for the best modelling approach of a complete WF.

The level of complexity and details that are integrated depends on several factors, including 1) the target of the study implementing such a model; 2) the data available in relation to the WF's geographical layout and terrain nature; 3) the WTs numbers, and types; 4) the distribution of WTs inside the WF (are they spread in a regular manner or spread according to the terrain); and 5) the degree of accuracy and time resolution of WS records, as well as the number of points inside the WF where WSs arrays are recorded. Generally, the most accurate method to model a WF is to include a single independent model for each installed WT and the corresponding WS stream incident upon it. Thereafter, the overall output of the WF is the algebraic summation of all the installed WTs per each time step. This method requires huge computational efforts and time, besides large data storage to perform such simulations, especially if tens of WFs are considered and each one is composed of hundreds of WTs.

Aggregating the WF as a single rescaled WT is the simplest and most widely applied method [5]. The aggregated WF rating equals the name plate rating of a single WT multiplied by the number of connected WTs, and the WTG model is then typical of a single unit model. However, this method is only valid when all the installed WTs are of the same type and are made by the same manufacturer. Otherwise, perceptible deviations and errors would arise between the aggregated model and the actual performance of the simulated WF. The level of detail is enhanced by the authors of [64], so that they offered two different WF aggregation models, either for fixed speed SCIG WTs or for DFIG WTs. The first one depends on the grouping of WTs (in other words clustering), where the WTs that are facing almost the same WS conditions are presented by a single WT with a rating that is the summation of the aggregated WTs ratings. Because there would be some minor deviations between the WS at each WT, a simple equivalent WS is estimated that equals the average value of the WSs incident on WTs in the same group at the same time. This is considered to be a compromise between model accuracy and complexity, such that if the diversity between incident WSs is decreased the aggregated model is more precise. However, this method is restricted and is only applicable for WFs in which WTs are arranged in rows on smooth land, or offshore WFs, because the regular distribution of WTs helps to achieve the grouping criterion for WTs with a minimized error. In the aggregation of DFIG, an equivalent power equation is derived for the overall WT. The equivalent power is based on the summation of the output power of all the WTs at the same WS to form what could be termed a lookup table. Afterwards, the equivalent WS for an aggregated WT is obtained by inversing the power function. Recent work proposed in [65] also focuses on the possible aggregation of a WF based on the layout of the WTs distribution inside the WF. The clustering process is based on the probability that each group of WTs faces the same WS. Number of clusters and number of WTs per each cluster are related to the angle of the incoming wind stream. However, the assumptions are smooth ground at the WF, that the WTs are arranged in regular rows parallel to each other, and that there are a similar number of WTs in all rows.

Comparable efforts have been proposed by [**66**], where two methods for obtaining equivalent power curve models for a WF based on field measurements were examined. The first model used the single rescaled WT aggregation; however, the rescaling procedure was slightly modified because a new power curve was obtained for the aggregated WT based on the field measurements of each WT generation history. Such a method is unable to participate in any forecasting studies for the WF, because the WF must already be constructed to obtain the mentioned curve. In addition, it is more suitable for a regular distribution of WTs inside a WF, and for a limited number of WTs. The second method is similar to the clustering algorithm offered in [65], but the major difference is in the applied clustering technique (which is called support vector clustering). It is of note that the second case study of [66] is more complicated than that of [65], because it considers a WF with a highly non-uniform distribution of WTs inside a WF area, and there are a larger number of integrated WTs. In contrast, the detailed multiple wake effects are investigated in [67] to estimate the impact of the wake effects on the expected generated energy of the WF. Generally, ignoring WS variations and reduction through the WF can lead to medium or high errors in the capacity assessment of a particular WF, and hence, the results of executed economical pre-studies are questioned in relation to this. Therefore, the implemented WF aggregation methods and their related details and parameters are discussed independently for each case study throughout the next chapters.

2.6. Wind farms' dispatching

The participation of WFs in load coverage during normal operation, and WFs requested and expected participation in the elimination of frequency excursions, depends on the dispatching procedure implemented. This procedure decides how many WTs from each WF should feed the load in cases of normal operation, and how many should participate in the curtailment of frequency events. Generally, dispatching algorithm simulations are highly dependent on WF aggregation methods and the ability to cooperatively control all the WFs connected to the grid. Applying advanced dispatching techniques depends on the data acquisition between all WFs, which needs a coherent communication system that binds all considered smart grid components [68]. For example, a single WT aggregation method facilitates the dispatching process of the installed WFs. In words, WF aggregation methods and the implemented dispatching algorithm are two sides of one coin.

In normal operation, the dispatching process is guided by wind energy penetration borders adjusted by SOs. In other words, the participation of WFs in feeding the instantaneous load demand is limited because the SOs do not trust that the wind energy can take command of the grid, even during load valley intervals. Thus, there must be a minimum limit for the conventional generation contribution to the load supply, and this ratio is specifically mentioned in the modern grid codes and depends on the system reliability and the possibility of sudden fatal changes in load. Comparatively, certain normal operation dispatch algorithms consider an economical approach to be the first priority, and as an illustration, WF owners select their generation schedules based on expected wind energy prices. Therefore, they offer high wind energy supplements during peak and moderate load periods to

guarantee high financial incomes. For example, an economic load dispatch method is offered by [69] to achieve the best wind energy and load dispatching, based on a probabilistic approach for WS from which the expected available generated wind energy is estimated. The authors called their method a 'Here and Now method', as it is capable of determining the best ratio between thermal units and WFs. In other words, a compromise between economics and the SOs' requirements determines the final share of wind energy at any instant during normal operation. In addition, storage banks that are charged by the rejected wind energy during low load demand intervals are utilized to improve the load dispatching feasibility and to smoothen the generated power; and the mismatch possibility between generation and demand is therefore mitigated [70].

The second major target for dispatching is to decide how many WTs should be switched to the frequency drop mitigation algorithm (i.e., the frequency support). Some researchers have interpreted the dispatching of WFs during frequency excursions as a simplified droop controller that triggers a fault operation in the WT. Previous research efforts proved that switching all WFs between normal and fault operation modes during frequency excursions has a clear negative influence on generated power constancy [71]. However, according to the thesis author's knowledge, available literature does not carefully and intensively consider dispatching techniques that are able to solve such problems. In contrast, most of the focus is directed to dispatching wind energy either during normal operation or with economic initiatives in mind. Further discussion and investigations are provided in Chapter 7.

2.7. The integration of storage mediums

Through all the previously presented ride-through and support algorithms, the WT operation deviates from the MPT operation; hence, an amount of energy is wasted. In addition, the reaction of WFs is always ambiguous according to the WS conditions before, during, and just after frequency events. For example, at high WSs, the system is supported for longer times and the probability of occurrence of a second frequency drop is reduced. Conversely, the fluctuations in system frequency and the probability of suffering a second drop increase during poor WSs conditions. Furthermore, WT inertia and aerodynamics have a strong influence on the WT's participation in a system frequency recovery. Therefore, integrating energy storage methods to provide required power support in cases of frequency events appears to be a promising novel solution.

Literature presents several types of energy storage methods such as battery banks, hydro storage, hydrogen reservoirs, and flywheels [72]. An optimization technique that uses cost and low resolution WS data is performed using fuzzy logic and a simple artificial neural network [73]. A predetermined threshold value for the error between the forecast output of WFs and the actual output is selected to govern the charging/discharging process. An inspiring algorithm that depends on the same error definition in hourly forecasted power, but with a higher acceptable limit (i.e., up to 50%), is presented in [74], but the work of the study was not concentrated on storage size estimation. It focused more on minimizing any financial penalties that could be delivered to the owners of the WF, if the WF's output

power deviates beyond a certain limit. However, some literature has analysed the performance of internal parameters of battery bank cells, namely the current and voltage [75, 76]. Principally, this work implied firm constraints on cell voltage and the overall battery bank current, but did not apply any restrictions on the power variation between the forecasted and actual generated values. The most promising part implemented a detailed model for NaS (Sodium Sulphur) and Li-ion batteries; hence, the results were feasible and relevant. In the same vein, battery voltage was governed and the total number of cells was estimated, so that a maximum limit of charging – discharging power was maintained [77]. Moreover, the impact of discharge time on discharge power boundary and ampere-hour capacity was examined. Generally, the mentioned literature utilized battery storage as a solution only for the negative influence of the intermittent nature of WS in relation to output power fluctuations. However, no solid trial existed to exploit the battery banks as a backup source to provide power surges in cases of frequency excursions, or to provide positive support in relation to conventional plants reactions. Therefore, Chapter 8 of this thesis investigates this area through utilizing battery banks in the mitigation of frequency excursions.

3. Method 1: Wind turbine over speeding and kinetic energy extraction[1]

The positive contribution of WFs required by system operators basically depends on the amount of stored KE in the WTs rotating parts and how to manage this during the elimination of frequency deviations. This chapter presents an algorithm to estimate and control the quantity of extractable KE stored in a WF during frequency events. Moreover, it manages the release of stored KE within a given time span to achieve positive participation in frequency dips clearance. The proposed method is based on tuning the tip speed ratio before and during a frequency drop according to several factors. The impact of the proposed algorithm on the power system frequency is analysed through assessing the expected enhancement in frequency deviation. A hypothetical grid is considered as a benchmark, and includes detailed models of WSs, WTs, and WFs to prove the credibility of the results obtained. The simulations executed proved that applying the proposed algorithm neutralizes the wind energy penetration influence on the frequency response, and in addition causes solid improvements, unless the incident WS is too slow or the frequency drop is high.

3.1. Wind turbine rotor speed variations

This thesis deals with the wind energy penetration influence on system frequency during frequency drops in relation to sudden generation loss or step load increase events. The droop characteristics of conventional power plants and the inertias have a major impact on system frequency performance in the case of drops [10, 52]. Stored KE in generators' rotating parts act as a backup to cover the sudden increase in the demand for electrical power, which acts for few seconds until the governors respond and modify the output power control signals [52]. The generator inertia (H_G) determines the time needed to release a certain amount of its stored KE to cover the deficit between generation and demand. However, this process leads to generator speed deceleration; hence, it deviates from the nominal system synchronous speed imposing the system frequency deviation. Generally, the maximum allowed change in a generator frequency is 1%; otherwise, it may lose synchronization with system frequency [78]. Accordingly, integrating wind energy by replacing conventional plants with WFs needs to be applied after studying the potential effect on system frequency attitude.

Literature offers several algorithms for operating WTs and WFs during frequency drops, which either neutralize and eliminate any possible negative influences or support the system during its recovery from frequency deviations. As an illustration, a control strategy to regulate active power for DFIG under various operating conditions is offered in [79, 80]. It attempts to dispatch the WF's output power according to the operators request in a similar manner to conventional plants. It also highlights

[1]Major content of this chapter is published in IET journal of Renewable Power Generation as indicated in Related publications list

the possibility of running WFs as spinning reserves. In addition, [80] proposes an equation to estimate the wind energy capacity with the view of replacing that from a certain conventional generator.

WT de-loading is also a key solution to provide active power support within very short durations from the connected WTs [81]. In particular, de-loading techniques depend on pitch angle control or setting WT operating points that are retarded or advanced from the typical operation conditions according to WT aerodynamics [7]. As an illustration, a WT has an optimum tip speed ratio for every moderate WS at which C_p is optimum, as explained earlier in Subsection 2.2. Consequently, controlling the tip speed ratio is utilized to produce step increase in output power as soon as the frequency drop occurs. It is also of note that, some research efforts aimed to evaluate WT inertia (H_{WT}) in a similar way to conventional generators [82].

This chapter offers a novel technique for use in controlling and estimating the amount of stored KE in installed WTs, and how to exploit it during power system frequency drops. Subsection 3.2 explains the offered algorithm, and Subsection 3.3 describes the implemented benchmark power system, integrated WS data, and relates examined case studies. The highest relevant results and the most important comments are highlighted and summarized in Subsection 3.4, and conclusions are delivered in the final subsection.

3.2. Proposed algorithm

This chapter offers a technique for use in controlling the KE injection from rotating parts of WTs to the power system during frequency drop events. Injected KE is fed into the power system in the form of a steep rise in active power supplied by the WF. Accordingly, this extra active power contributes positively in any frequency drop elimination caused by unexpected loss in generation or sudden increase in loads. Control of the KE storage or its extraction is executed through control of the WT's rotational speed according to the WT's characteristics and the instantaneous incident WS. For example, during normal operations the WT runs at a higher rotational speed; explicitly, the tip speed ratio is adjusted to a higher value (λ_H) than its optimum value, which increases the amount of stored KE in the WT rotating parts. As soon as the frequency drop occurs, the WT's rotational speed is gradually decelerated to a certain threshold limit, extracting a given portion from the stored KE. In turn, this extracted energy is transferred to the system in form of a fixed step increase in the active power supplied within a predetermined support time (T_s). Applying this algorithm maintains a positive WT contribution in the system frequency recovery process. However, it should be mentioned that implementing such an algorithm requires WTs that are equipped with a variable speed generation system, either DFIG or full speed converters. Generally, variable speed WTs generators have upper and lower rotational speed limits, which are strictly defined by the manufacturer according to the specifications of integrated power electronic converters. In particular, the dominant range of WT speed variation starts from 0.7 to 1.3 pu with respect to the WT base rotational speed (GO_{base}) [5]. An examination of the proposed technique is based on transforming the injected KE into a given value of

frequency deviation improvement, using (3.1) at each simulation time step so that the updated value of $\Delta f_{improved}$ according to the Δf value (i.e., the frequency deviation at the previous time step) is evaluated. The derivation of this equation and other equations implemented in this chapter is illustrated in Appendix, Subsection 11.5:

$$\Delta f_{improved} = \mathrm{f_o} \cdot \sqrt{\left(\left(\frac{\Delta KE_{available}}{\mathrm{KE_{base}}}\right) + \left(\frac{\mathrm{f_o} + \Delta f}{\mathrm{f_o}}\right)^2\right)} - \mathrm{f_o} \qquad (3.1)$$

$\Delta KE_{\mathrm{available}}$ is the amount of stored KE in all the WTs installed in a WF at a certain instant. In other words, each WT injects a fixed value of extra active power, namely '$\Delta KE_{\mathrm{available}}/\mathrm{T_s}$', and thus the WF's overall output is equivalent to the aggregation of the output of the installed WTs. However, because $\mathrm{T_s}$ is relatively very short, it can be assumed that $\Delta KE_{\mathrm{available}}$ is linearly released within this interval. The value of $\mathrm{T_s}$ is determined by trial and error based on the type of WT by estimating the time required by a WT to reach the lowest threshold rotational speed (ω_{min} at the lowest allowed tip speed ratio (λ_{min})), and it also depends on the magnitude of the incident WS. On average, $\mathrm{T_s}$ is found to be 15 s for GE-77 WT [17]. It is considered that the actual value of $\mathrm{T_s}$ should be assessed for each WT model, because it is strongly related to the aerodynamic characteristics, installed generation system inertia, and the power rating. Thereafter, storing and releasing $KE_{available}$ is controlled using the following technique:

Firstly, the incident WS must be within certain range with previously calculated thresholds using (3.2), otherwise the proposed algorithm is deactivated:

$$\mathrm{WS_{min}} = \frac{0.8 \cdot \mathrm{R} \cdot \omega_{\mathrm{min}}}{\lambda_{\mathrm{min}}},\ \mathrm{WS_{max}} = \frac{\mathrm{R} \cdot \omega_{\mathrm{max}}}{\lambda_{\mathrm{H}}} \qquad (3.2)$$

Increasing λ_{H} increases the WT's de-loading ratio, so that the amount of wasted energy increases during normal operation, as the WT is operating at C_p that is farther from $\mathrm{C_{p\text{-}optimum}}$. Consequently, it is expected that SOs and governments will financially compensate WFs owners to accept this operation method, so that WFs support the grid during frequency drops. The increase of wind energy penetration levels in modern grids above certain limits will make this ancillary service mandatory.

Figure 3.1 shows the relation between λ and C_p in the implemented algorithm. It is of note that the impact of C_p on WT operation is investigated through the value of λ where $C_p = \mathrm{f}(\lambda, \beta)$, as previously explained in Subsection 2.1.2. However, the influence of the pitch angle is neutralized in this algorithm because it is assumed to be zero at WSs of less than, or equal to $\mathrm{WS_R}$. Otherwise, the incoming WS input is limited to $\mathrm{WS_R}$ if the WS's actual value in the integrated array is beyond the

rated value and less than WS_{CO}. In other words, it is assumed that the pitching control keeps the WT generating its rated output as long as the incident WS does not exceed WS_{CO}. The next step is then to calculate lower tip speed ratio (λ_L) at which the deceleration process stops. Evaluation of λ_L is based on WS and Δf at the instant of the drop initiation, using (3.3), but λ_L should not violate λ_{min}.

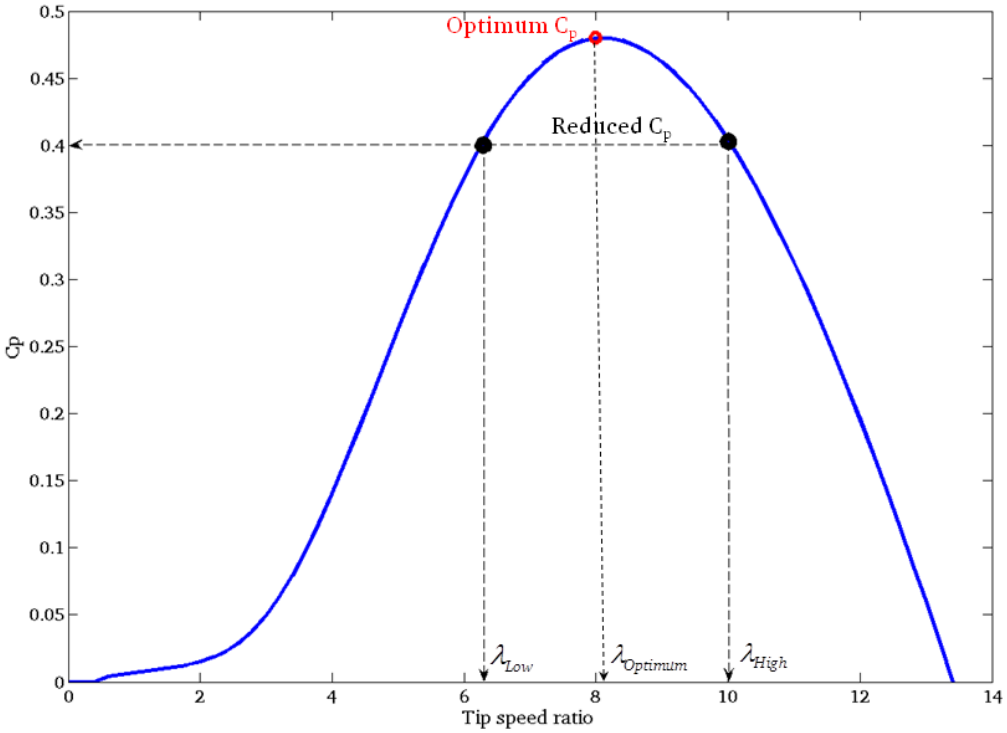

Figure 3.1 Example of the relation between C_p and the tip speed ratio

$$\lambda_L = \sqrt{\lambda_H^2 + \frac{M}{WS^2} \cdot \frac{2 \cdot H \cdot S_b \cdot R^2}{J_{WT} \cdot N_{WT}} \left[\frac{2\Delta f}{f_o} + \frac{\Delta f^2}{f_o^2} \right]} \qquad (3.3)$$

$$\lambda_H = 1.15 \cdot \lambda_{optimum}, \lambda_{min} = 0.85 \cdot \lambda_{optimum}, \; M > 0, \; \Delta f < 0$$

H and S_b are the power system inertia (in seconds) and the system MVA base capacity, respectively, and J_{WT} is the sum of the moments of inertia in the WT's shaft and masses, and R is the rotor radius. The value of N_{WT} equals the number of WTs affected by the same wind stream (e.g. if the WF contains 55 turbines and the wake effects are ignored, then the WS is typical in the whole WF; hence N_{WT}=55). Comparatively, when 'n' identical WFs are affected by similar WS conditions, then N_{WT} equals 'n' multiplied by the number of WTs per WF. However, consideration of shadowing and wake reduces N_{WT}, so that it equals the number of WTs subjected to the same WS. The parameter 'M' is basically related to the frequency deviation magnitude, and is evaluated using (3.4). Mathematically, 'M' is the ratio between a WF's extractable KE, and the KE required by the system to eliminate the frequency deviation. The value of 'M' has a great impact on the amount of λ_L retardation from λ_H; consequently, it affects the WF contribution in frequency drop mitigation. In particular, as M increases the λ_L

decreases (i.e., $(2\Delta f/f_o) >> (\Delta f^2/f^2_o)$ and $\Delta f < 0$). Thus, further deceleration occurs and more KE is extracted. However, the WS has also an impact on the retardation magnitude.

$$M = WS^2 \cdot \frac{\left(\lambda_{\min}{}^2 - \lambda_H{}^2\right) \cdot J_{WT} \cdot N_{WT}}{2 \cdot H \cdot S_b \cdot R^2} \cdot \frac{1}{\frac{2 \cdot \Delta f}{f_o} + \left(\frac{\Delta f}{f_o}\right)^2}, \text{ where } \Delta f < 0 \quad (3.4)$$

The 'M' parameter may have a fixed or variable value according to the operator's policy. When 'M' is variable, its value is updated every simulation time step using (3.4) with respect to continuously varying parameters, namely, WS and Δf. A variable 'M' mode tunes λ_L to higher values so that the WT speed deterioration is alleviated and extracted KE is reduced. However, this operation mode shortens recovery time (t_R), thus the WT has better opportunity of supporting the system during further consecutive drops, which might occur within a short time span just after the initial drop. However, when the operator aims to utilize all the available stored KE to overcome certain frequency drop, 'M' is adjusted to a constant value. According to (3.4), it is noticed that 'M' is almost proportional to WS, and inversely proportional to Δf. Meanwhile, the other parameters are constants or pre-adjusted (e.g., λ_H). To utilize a portion from the extractable KE, 'M' fixed value is reduced, thus estimated at deep Δf and low WS. This constant value is evaluated only once at certain pre-determined conditions, and is then fixed throughout the whole simulation process. In addition, fixing 'M' value at a low value shortens t_R; hence, WTs are able to provide support when the system suffers a second minor frequency drop while it is recovering from the main one. In conclusion, the choice of using either a constant or a variable selection for 'M' involves potential risks that should be analysed thoroughly by the operator.

As an illustration of the use of t_R, the WT should be partially unloaded for certain duration after the support period ends so that it has the opportunity to return to its normal rotational speed (i.e. returning to λ_H). In most literature t_R is treated as a constant duration. In contrast however, this research considers t_R as a variable that is proportional to WS and λ_L, and which can be considered as a merit. In particular, fixing t_R wastes more energy as it keeps the WT partially loaded, even if it has already recovered its default rotational speed. Therefore, estimating t_R each time the WT supports the system saves some energy and enables the WT to efficiently return to its normal operation. t_R is calculated just 1 s before t_S ends (i.e. at the end of the KE extraction interval) using (3.5). Whereas, C_F is a certainty factor greater than unity, and ensures that the rotational speed recovers to a normal value. The evaluation of $Slope_{WT}$ is made using (3.6), and is illustrated in Figure 3.2 according to the derived and predetermined value of t_s (15 s in this research work). Hence the corresponding slope ($Slope_{WT}$) is evaluated at WS_{min}, so that a tough case is considered ($Slope_{WT}$=0.0147 rad/s^2).

$$t_R = C_F \frac{WS\left(\lambda_H - \lambda_L\right)}{R \cdot Slope_{WT}} \quad (3.5)$$

$$\text{Slope}_{WT} = \left(\frac{WS_{min} \cdot (\lambda_H - \lambda_{min})}{R \cdot t_S} \right) \quad (3.6)$$

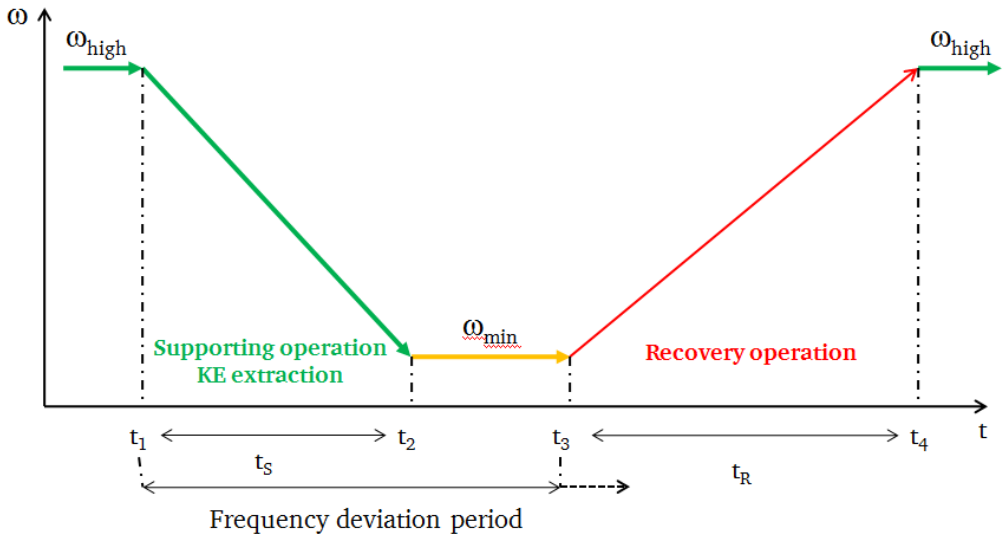

Figure 3.2 Rotational speed variations during frequency support and recovery phases

The main blocks of simulation model as well as a compact flow chart for the whole algorithm are depicted in Figure 3.3 and Figure 3.4 respectively. Although equations (3.1) and (3.5) may appear to be concerned with steady state conditions, they reflect frequency transients as they are evaluated every simulation time step to update the values of Δf, $KE_{available}$ and $KE_{required}$. $\lambda_{optimum}$ value is one of WT specifications provided by the manufacturer (aside from the proposed algorithm); most WTs are operated using a default of $\lambda_{optimum}$ to maintain maximum possible wind energy harvesting by tracing $C_{p\text{-}optimum}$. Further details are explained in the equations' derivations in Appendix Subsection 11.5.

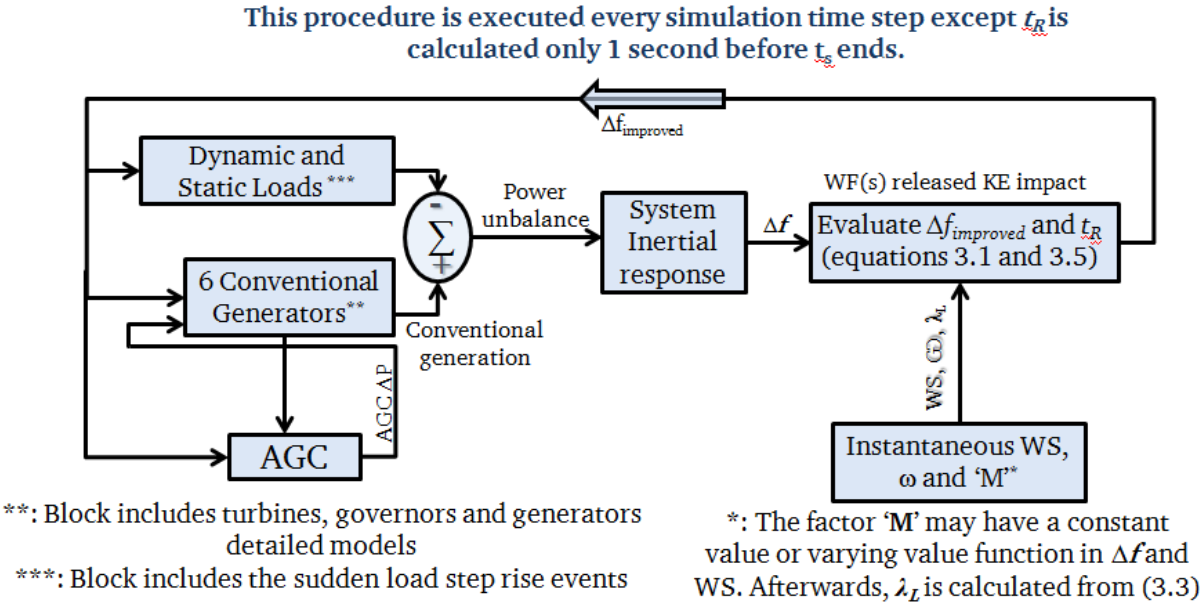

Figure 3.3 Proposed algorithm main blocks, input and output signals

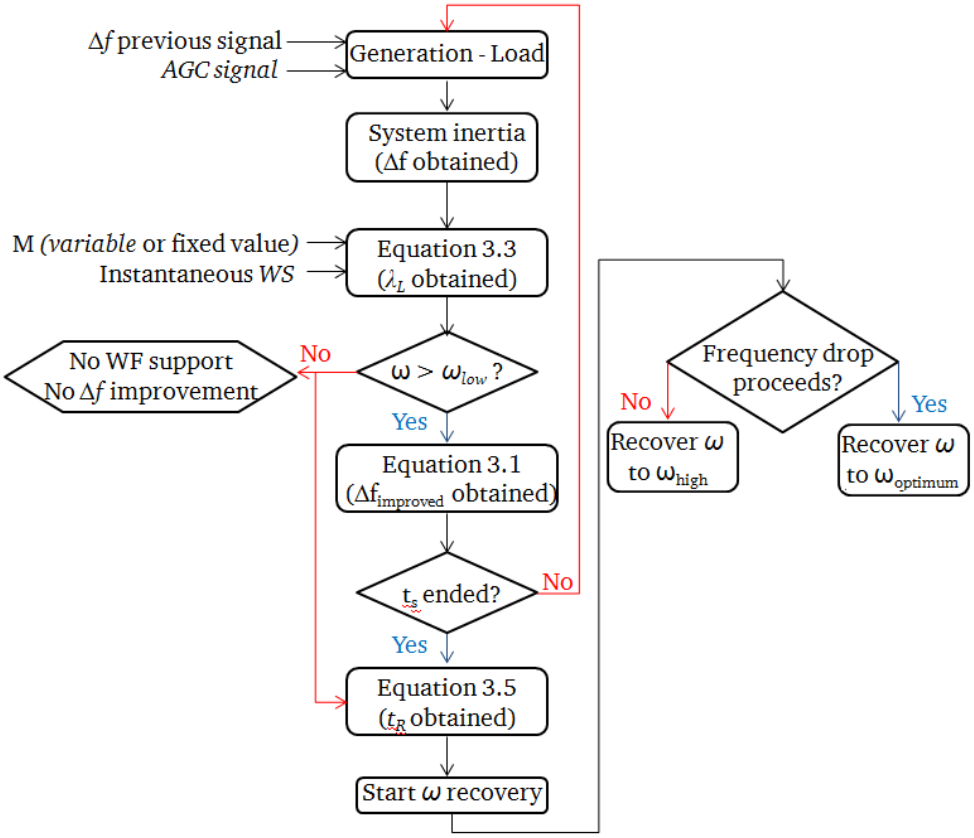

Figure 3.4 Compact flowchart for the proposed algorithm during support mode

3.3. Implemented benchmark system and case studies

The proposed algorithm is examined through time domain simulations implemented on a hypothetical system that has a medium generation capacity. The executed case studies cover major topics related to the aims of the proposed algorithm. In addition, they highlight the impact of WS conditions, the WF aggregation, and the algorithm parameter variations on the obtained results.

3.3.1. Benchmark system

The integrated system is composed of six different aggregate conventional power plants, as shown in Figure 3.5. Transmission lines and transformers are not included in this study due to their minor effect on frequency analysis [10, 52]. The models in [44, 83] are used to simulate the installed hydro and steam plants, including turbines and governors coupled with that of **[**84**]** which is used to model the gas turbine and its speed governor. Additionally, AGC **[**85**]** and a variable load regime are connected to the system so that most of power system generation and load components are considered. The system inertia block simulates the dynamic response of the power system to load changes, as explained in [52], and the resultant inertia of the connected conventional plants is calculated using (3.7):

$$H = \left[\sum_{i=1}^{m} S_{b\,i} \cdot H_i\right] \frac{1}{S_b} \qquad (3.7)$$

H_i and S_{bi} are the inertia and rated MVA of power plant (*i*) respectively, and 'm' is the number of connected conventional plants. The integrated WSs array is based on the readings obtained at the Za'afrana WF, on the Red Sea shore in Egypt [86], where WS data are arranged chronologically in one hour steps. Table 3.1 summarizes essential data in relation to the nature of WS at the chosen location during winter. However, the frequency studies require high time resolution data, and hence, the array steps of WSs need to be in the range of seconds. To overcome this problem, the algorithm offered in [87] is implemented, so that as seen in one of the case studies the WS average value is estimated every 25 s in addition to acknowledging wake and shadowing effects inside the WF.

Table 3.1 Wind speed statistics during winter at Za'afrana

Winter (08:00 to 21:00)		
Value (m/s)	**Actual (every 2 h for 91 days)**	**Generated array**
Average	6.31	5.15
Max	11.09	15.65
Min	2.71	2.884
No. of events WS>=WS_r	114/1183 (9.6%)	4290/46800 (9.2%)
No. of events WS<=WS_{CI}	15/1183 (1.3%)	562/46800 (1.2%)

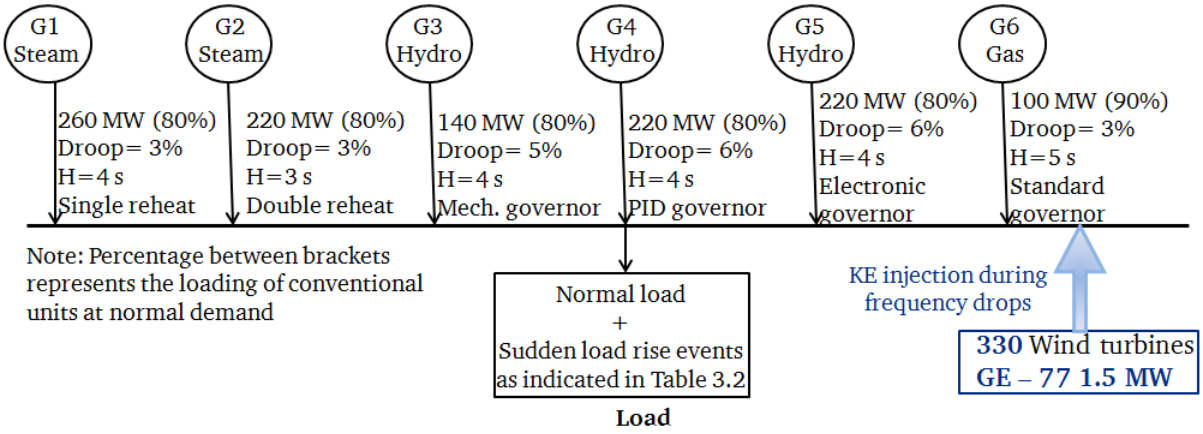

Figure 3.5 Implemented power system single line diagram

This research work has chosen to study system performance at a relatively variable WS, as this emphasizes the influence of the proposed algorithm and the implemented system. The duration of the simulation is 13 hours (08:00 to 21:00, which is equivalent to 46800s) throughout the winter season, as WSs achieve the highest levels during this period. The integrated WT is GE-77, and it has ($G\mathcal{D}$ vs. PWT_m) curves at several WSs, as previously presented in Figure 2.5. The moment of inertia (J_{WT}) of GE-77 is 543 kgm^2.

3.3.2. Case studies

The six case studies examine the wind energy integration impact on system frequency in different circumstances during the specified hypothetical load step rise events mentioned, wherein the magnitude of each step is stated as a percentage from S_b. The conditions examined include the integration of WFs, with or without any changes in conventional generation capacity, coupled with including or ignoring the wake effects. In addition, the proposed cases highlight the advantages and

disadvantages of fixing, or actively varying 'M' during the KE extraction process. The influence of delaying the AGC signal on the system frequency is also tested. A basic case study represents the response of the benchmark system with no integrated WF, and it is therefore used as a reference to compare and judge the results of other case studies. The default WF is composed of 55 GE-77 WTs. When the wake effect is considered, the WF layout is divided into 5 rows, and each one is composed of 11 WTs. The incident wind stream faces the WT blades directly in each row, if the stream orientation angle is zero with respect to the WT horizontal axis [87]. In addition, the WS magnitude changes from one row to another due to the shadowing effect from the towers and blades of the WTs in the row in front. In contrast, when the wake effect is ignored, all WTs inside the WF are subjected to identical WS. 'M' is considered to be the variable in all case studies excluding cases four and six, as explained in the following.

Case study 1: Single WF is integrated; wake effects and shadowing are ignored.

Case study 2: Single WF is integrated; wake effects and shadowing are acknowledged. For simplicity, it is assumed that the WTs are arranged in regular rows and columns inside the WF. The first row is subjected to the initial free stream of WS; afterwards the WS is reduced gradually in each row in relation to the shadowing and wake effects of the towers. The average wake WS is evaluated at each row using (3.8) depending on the WTs dimensions and other factors [87, 88, 89]. The thrust coefficient (C_t) is evaluated using an empirical formula. $WS(x)$ is the velocity in the wake at distance x; and WS_o is the free stream WS (i.e. the initial incident WS just before it hits the first WT and starts to propagate through the WF). It is of note that the distance between successive WTs (x) is inversely proportional to the reduction in $WS(x)$. As an illustration, an increase in x achieves a useful curtailment of the negative influence of the tower and shadowing on the WS magnitude projected on the next WT blades. The second factor is R, as its increase amplifies the impact of the wake effects. In addition, the time delay due to the propagation of the WS throughout the WF is included, as in (3.9) [63], where D_{row} is the distance between two successive rows and is assumed to be $12 \cdot R$ while $k_w = 0.08$. In particular, t_{delay} interprets the time required by the wind stream to travel from one row to another, thus WS_o and $WS(x)$ are asynchronous.

Table 3.2 Data of five step load increase events (percentage from S_b)

Value/Event	Event 1	Event 2	Event 3	Event 4	Event 5
Load step, MW	97 (10.5%)	84 (9.1%)	110 (12%)	80 (8.7%)	108 (11.7%)
Start time, s	3078	12160	22180	33230	42280
Duration, s	2938	3220	3190	3040	2840

$$WS(x) = \mathrm{WS_o} \cdot \left[1 - \left(\frac{\mathrm{R}}{\mathrm{k_w} \cdot x + \mathrm{R}}\right)^2 \cdot \left(1 - \sqrt{1 - \mathrm{C}_t}\right)\right],\ \mathrm{C}_t = \frac{3.5\ \mathrm{m/s} \cdot (2 \cdot \mathrm{WS_o} - 3.5\ \mathrm{m/s})}{\mathrm{WS_o}^2} \quad (3.8)$$

$$t_{delay}(x) = \frac{\mathrm{D_{row}}}{WS(x)} \quad (3.9)$$

Case study 3: A gas plant is replaced by a certain number of WFs with an equivalent generation capacity. It is well known that the annual average production of a WF is 20–30% of its nameplate rating [89, 90]. This chapter assumes that the considered WF generates 20% of its aggregate power rating (i.e. 55 · 1.5 MW · 20%=16.5 MW). However, the participation of the gas plant in load feeding is 90 MW, therefore it needs to be replaced by 6 WFs (6·16.5=99 MW). In this case, the production of the WFs (namely 99 MW), reflects 11% wind energy penetration of the total scheduled generated power. This penetration level is subjected to minor and major fluctuations according to the instantaneous WS (e.g. wind energy penetration reaches 38% when the combined WFs generate 70% of their aggregate rated output). This replacement procedure affects normal operation, in addition to system frequency response during frequency drops due to the continuous WS variations. Therefore, this chapter focuses on the WF contribution during frequency drop events. Note that the six WFs are aggregated as one WT facing the same WS, because it is assumed that the WS is similar in the six WFs. This case study also ignores the wake and shadowing effects.

Case study 4: This has similar conditions to Case study 3, and the only difference is that this study keeps 'M' as a constant value, which is calculated at 56% from the WF frequency deviation limit, namely, 1% from the nominal frequency (i.e. $\Delta f = (50 \cdot -0.01) \cdot 0.56 = -0.28$ Hz). This Δf value is selected because it is assumed that WFs do not contribute to frequency recovery if Δf exceeds this limit, but they operate normally to avoid loss of synchronization. In other words, the 'M' value evaluated at Δf = -0.28 Hz and at a moderate WS equals the average between WS_r and WS_{min}, namely, 6.5 m/s. Consequently, 'M' equals 4.4397 using (11.10) as illustrated in Appendix 11.5.

Case studies 5 and 6: Case study 5 has similar conditions to Case study 3, and Case study 6 is similar to Case study 4, except for the use of intended delay in the AGC signal in Case studies 5 and 6. The AGC signal is delayed by 40 s to emphasise the impact of the offered technique, to ensure that it does not merge with the reactions of the conventional generator.

3.4. Results and Discussion

The next two sub-sections summarize the basic comments and discussion obtained from the results, figures, and tables. The first subsection focuses on the system frequency response of all case studies, and the second subsection discusses variations in the parameters of the proposed algorithm.

3.4.1. Impact on system frequency response

The system frequency response for some case studies during events 2 and 3 are depicted in Figure 3.6 and Figure 3.7, respectively. Event 3 is characterized by a relatively high sudden load increase of 12%, and it thus emphasises the impact of the proposed algorithm on the elimination of frequency deviations. However, Case studies 1 and 2 are not displayed in Figure 3.7 because they devote very low wind energy participation levels, particularly in Case study 2, due to acknowledgment of the influence of wake and shadowing. System frequency oscillations increase in Case study 3, as illustrated by the WFs' medium penetration level, which leads to a considerable contribution in frequency drop clearance. Thus, switching the WTs from support mode to recovery mode and vice versa participated in this oscillatory response.

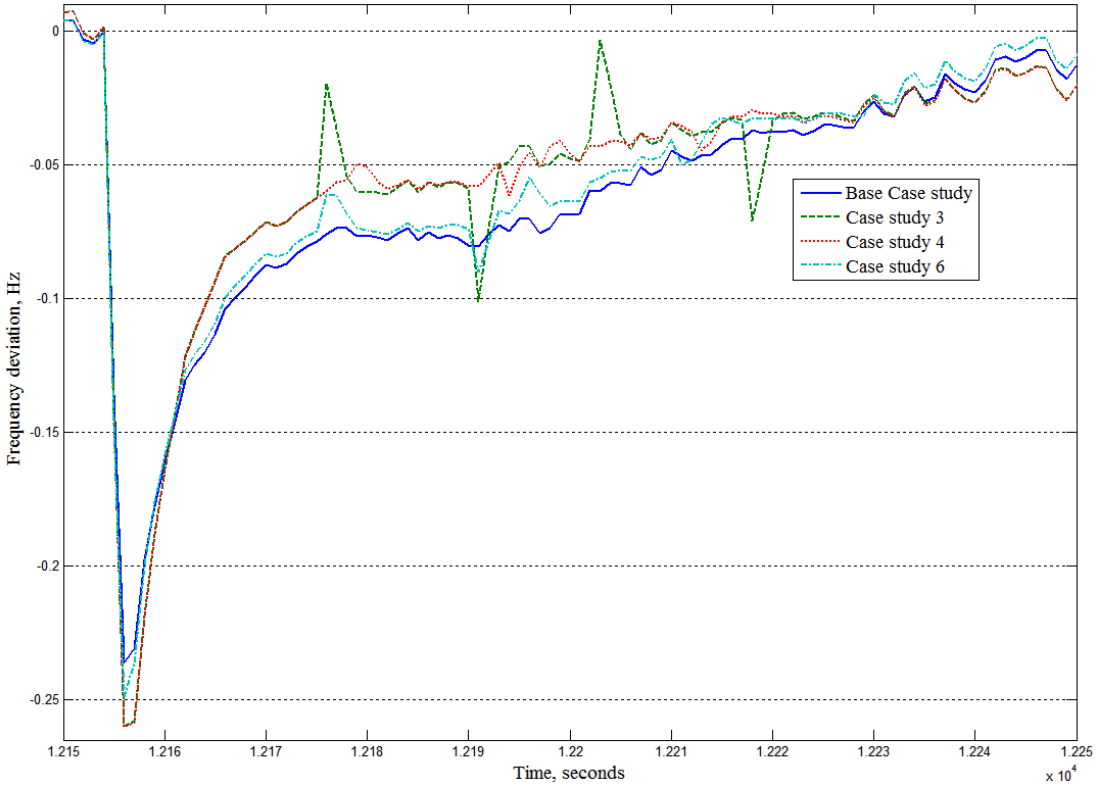

Figure 3.6 System frequency responses during event 2 in selected case studies

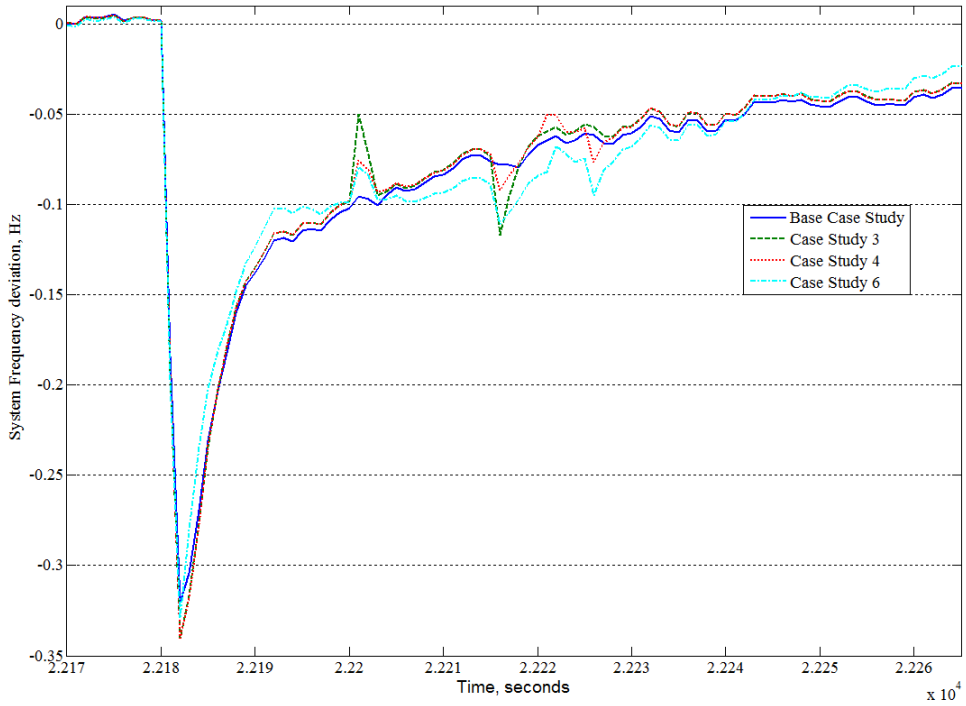

Figure 3.7 System frequency responses during event 3 in selected case studies

Nevertheless, this drawback needs to be fixed through an adequate dispatching method that organizes when WTs (inside each WF) switch between normal and fault modes during the curtailment of frequency drops. In Case study 4, mitigation of the contribution of WFs (i.e. because 'M' is fixed) is coupled with a delayed AGC signal, which extends the time required by the system to balance the 'generation- load' mismatch. To deepen the analysis of the obtained results, three special factors are evaluated at each event in all case studies, namely the maximum frequency drop (Δf_{max}), frequency deviation after 10 s from event initiation (Δf_{10s}), and the required time to reach the frequency safe margin (i.e. ±30 mHz) after the event occurrence (t_{SM}). In addition, the KE injected by WF(s) within four minutes of each event initiation is estimated. In event 1 in Case Study 1, the WF integration improves t_{SM} as it is shortened by 17 s in comparison with the time taken in the base case study, as shown in Figure 3.8. Meanwhile, Δf_{max} records negligible changes between the base case study and Case Study 1 in all events (as shown in Table 3.3) as a consequence of the low wind energy penetration level, because only one WF is integrated. The limited amounts of injected KE shown in Figure 3.9 are unable to mitigate Δf_{max}, but they reduce t_{SM}. In addition, in spite of the low WS, WF integration does not cause a decrease in t_{SM} during events 2 and 3, which is a merit for the proposed algorithm. However, high load step rises in events 4 and 5 overcome the positive contribution from the WF, causing an extension of t_{SM}. Case study 2 ensures the previous observations coupled with lower amounts of injected KE, because the wake effects reduced the incident WS on the WTs, leading to missed synchronization between the magnitudes of the WSs streams that were projected on each group of WTs. For example, a group of WTs may be subjected to a moderate WS that is efficient enough to run them at 50% of their rated power, while another group located on the other side of the huge WF,

may only operate at 35%, due to the lower incoming WS. In such a case, there would be a drop of about 60% of extracted KE during event 3 in comparison with Case study 1. This reduction is relatively high, and can be eliminated by applying more accurate methods for estimating the shadowing and wake effects. In general, however, the single integrated WF proved to have a neutral or barely positive impact on system frequency recovery, especially in Case study 1.

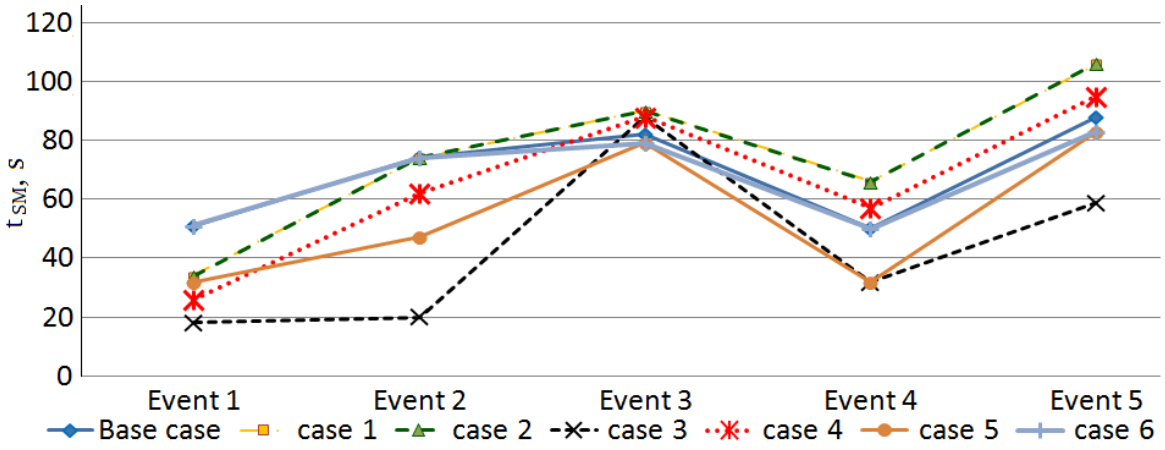

Figure 3.8 t_{SM} for all Case studies and events

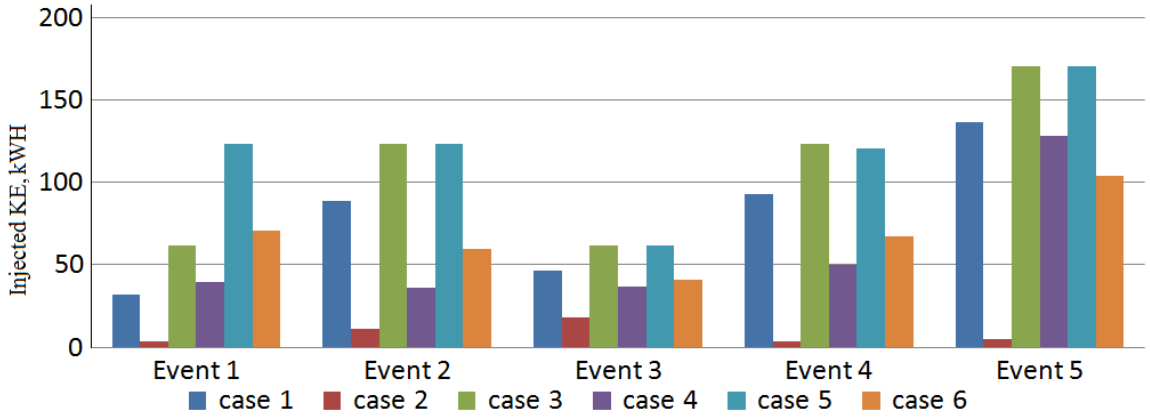

Figure 3.9 Overall released KE within 4 min after event initiation

In Case study 3, t_{SM} is reduced dramatically in event 2 and considerably in events 1, 4, and 5, as shown in Figure 3.8. Nevertheless, the amount of KE released is not four or five times the KE released in Case studies 1 and 2, as would be expected because the six WFs are integrated in comparison with the single WF used in Case studies 1 and 2. For example in event 4, 120 kWh is released by the WFs in Case study 3, and only 90 kWh by the single WF used in Case study 1. As an illustration, the short t_{SM} mitigates the WFs participation, as WFs release stored KE when the frequency drop violates the safe margin. Hence, reaching this safe margin faster terminates the WFs' supporting role by stopping the KE extraction process and starting the WTs' recovery stage. In addition, a comparison between Δf_{10s} in Case study 3 and the base case study shows that an improvement of 55 mHz and 47 mHz during events 2 and 5 respectively, as shown in Figure 3.10. In contrast, no solid improvement is achieved in Δf_{max} during the same cases, as the wind energy penetration level is still not high enough to sustain the earlier frequency deviation.

In Case study 4, the impact of 'M' is examined, and the obtained results reaffirm the discussion conducted in Subsection 3.3.2. Fixing 'M' reduces the extracted KE, as presented in Figure 3.9, so that all t_{SM} values are less than in Case study 3 (e.g. t_{SM} increased by 21 s in Event 4). In addition, Case study 4 showed the worst recorded Δf_{max} in all the events, as highlighted in red in Table 3.3. However, the fixed 'M' technique merits are not practically proven in this research work. In particular, the system should have suffered a second frequency drop just after any major event by 20 or 30 s to highlight the advantages of setting 'M' to a predetermined constant value. In summary, applying this scenario shows that WFs are still capable of playing a positive role by releasing the remaining stored KE, which is saved due to imposing a variable 'M' technique.

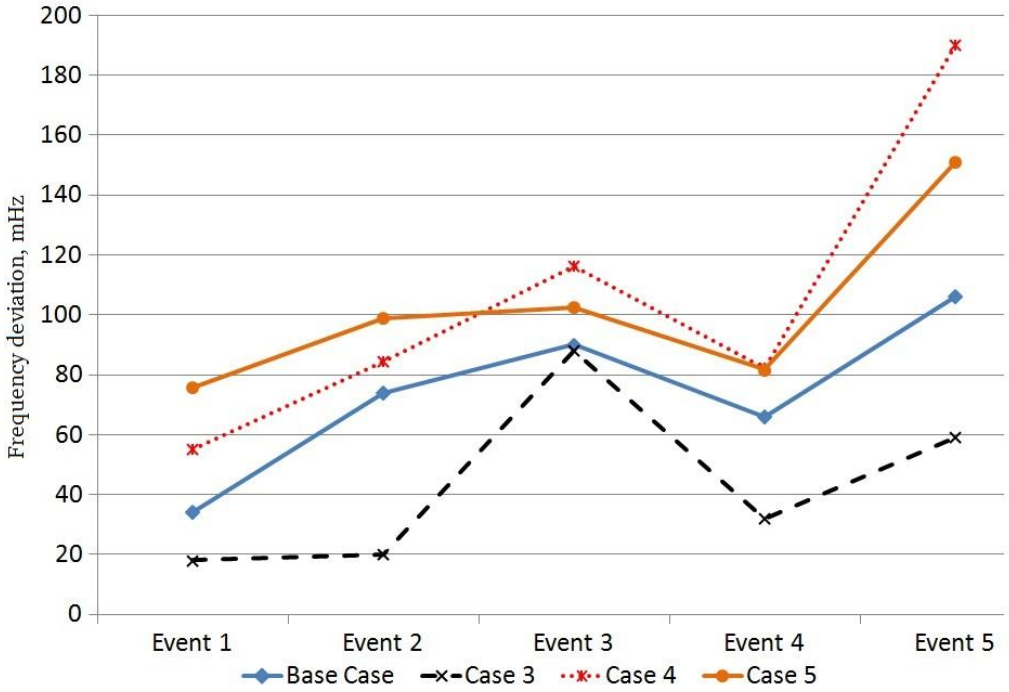

Figure 3.10 System frequency deviations after 10 s from each event initiation

Finally, the AGC delayed signal impact is tested in Case studies 5 and 6. Contrary to the obtained results, it was predicted that all parameters would deliver a worse result with respect to Cases studies 3 and 4 respectively. As an illustration, the delay of AGC signal mitigates the participation of conventional generators in eliminating the sudden imbalance between generation and load demand within this retard period (40 s). In contrast, proposed algorithm proved an acceptable validity as it has limited the delayed AGC signal's negative consequences. In particular, values of t_{SM} increased so that they were larger than those in the base case study, and during event 3, they improved by 3 s (as seen in Figure 3.8). It was interesting to find that highest extracted amounts of KE occurred in Case study 5 (during event 4 the KE was almost double that in Case study 4, as shown in Figure 3.9). As an illustration, the constraints in Case study 5 forced the WFs to utilize most of their extractable KE to compensate for the delayed conventional generation participation. However, imposing a fixed 'M' value in Case study 6 reduced the extracted KEs in comparison with that of Case study 5, during all

events. In addition, delaying the AGC signal exacerbated Δf_{10s} in Case study 5, compared to results in Case study 3, during all events. For example, Δf_{10s} decreased by 61 mHz and by 45 mHz in events 1 and 4 respectively, as shown in Figure 3.10, and the worst results occurred in event 5 (130 mHz) due to the highest load rise event. It is considered that the low wind energy penetration level (i.e., 11%), coupled with the low incident WS during some events cause this negative influence. It is illustrative to mention that Δf_{max} is almost similar in Case studies 5 and 6 throughout the five events, as shown in Table 3.3. This ensures that the evaluation method of 'M', using either a variable or pre-determined fixed value, has a neutral impact on the system response within such an early stage just after the occurrence of the frequency excursion.

Table 3.3 Max. Frequency drops in all cases (worst deviation at each event marked in red)

Case/Index	Max frequency drop, mHz				
	Event1	Event2	Event3	Event4	Event5
Basic	254.07	248.39	320.5	225.43	354.43
1	253.06	248.49	320.58	225.02	354.06
2	**253.06**	248.49	320.58	225.02	354.06
3	247.58	259.89	340.07	230.19	373.86
4	246.49	**259.95**	**340.08**	**230.98**	**361.39**
5	245.43	249.01	329.54	198.35	320.87
6	243.12	248.89	329.34	193.08	322.28

3.4.2. Attitude of the main parameters of the proposed algorithm

This subsection draws attention to the variations in the main parameters of the proposed algorithm, namely: WS, λ_L, and t_R, in addition to the expected improvement in Δf. It is of note that the displayed frequency values in the following figures represent the *improvement magnitude* and not the new deviation. For example, when Δf actual value is -0.6 Hz and the expected frequency improvement depicted in a figure is 0.06 Hz, this means that $\Delta f_{improved}$ is -0.54 Hz. Initially, it is important to explain why the frequency deviation improvements in Figure 3.11 and Figure 3.12 are constant, even though the WS and actual frequency deviation are continuously changing. Generally, the fixed frequency deviation improvement is related to the role played by the variable 'M' value, as it keeps the expected Δf enhancement constant independent from other factors. Consequently, power system operators are aware that the expected system performance and the integration of WF(s) will not lead to extremely unpredictable changes in frequency response. It is of note that the time delay of the electronic power devices is ignored, hence WF support starts just after the frequency drop occurs, as shown in Figure 3.11 (i.e., event 5 starts at $4.228 \cdot 10^4$ s). Before the KE extraction process starts, t_R and λ_L oscillate continuously, based on the instantaneous WS (as depicted in Figure 3.11(b) and (c) respectively). As soon as Δf violates the safety margin, the proposed algorithm records the λ_L value at the beginning of each t_S and keeps it fixed. In spite of integrating only one WF in relation to the moderate WS in Case study 1 event 5, the expected Δf enhancement was encouraging (6.5 mHz). Meanwhile the value of t_R was not very long (15 - 22 s), and thus it is considered that the WF could re-support the system if a second successive drop occurred a short time after the first one.

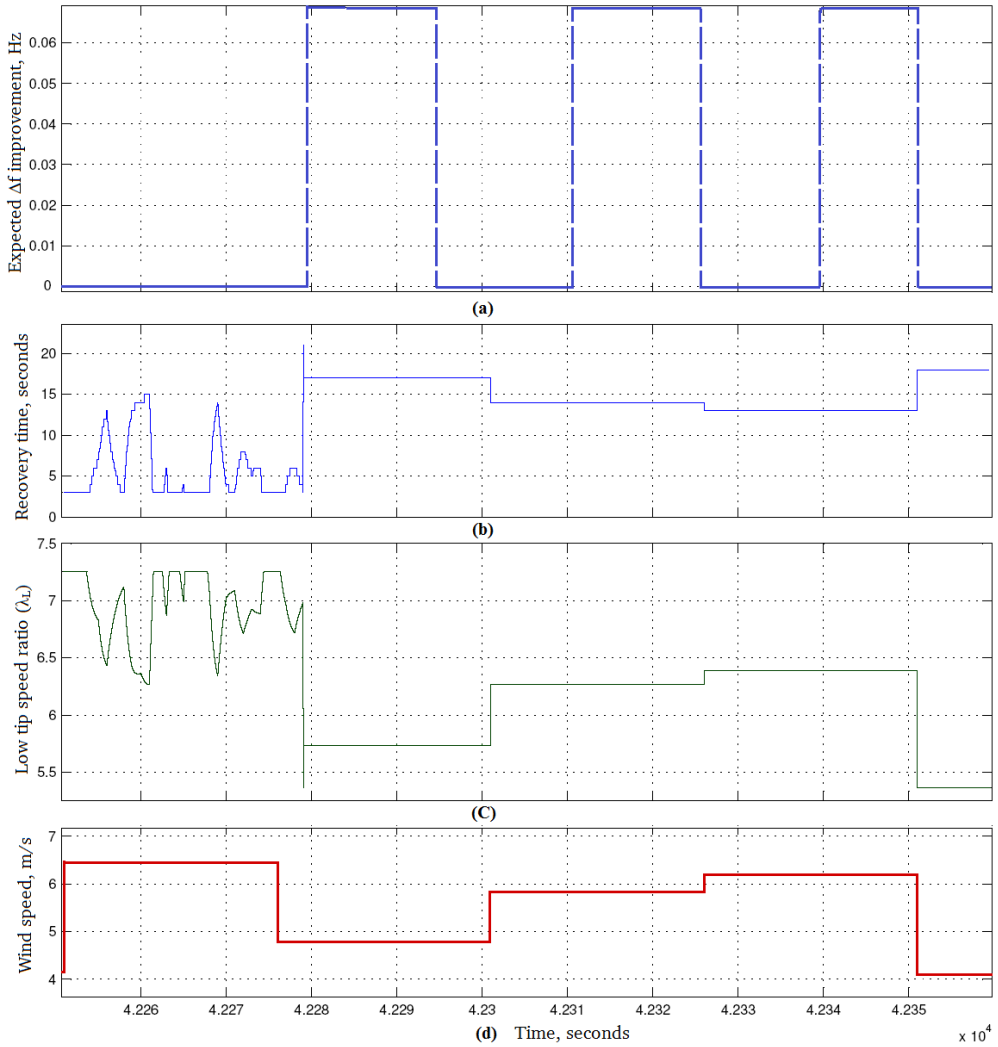

Figure 3.11 Case 1, event 5: a) frequency deviation improvement, b) t_R, c) λ_L, and d) WS

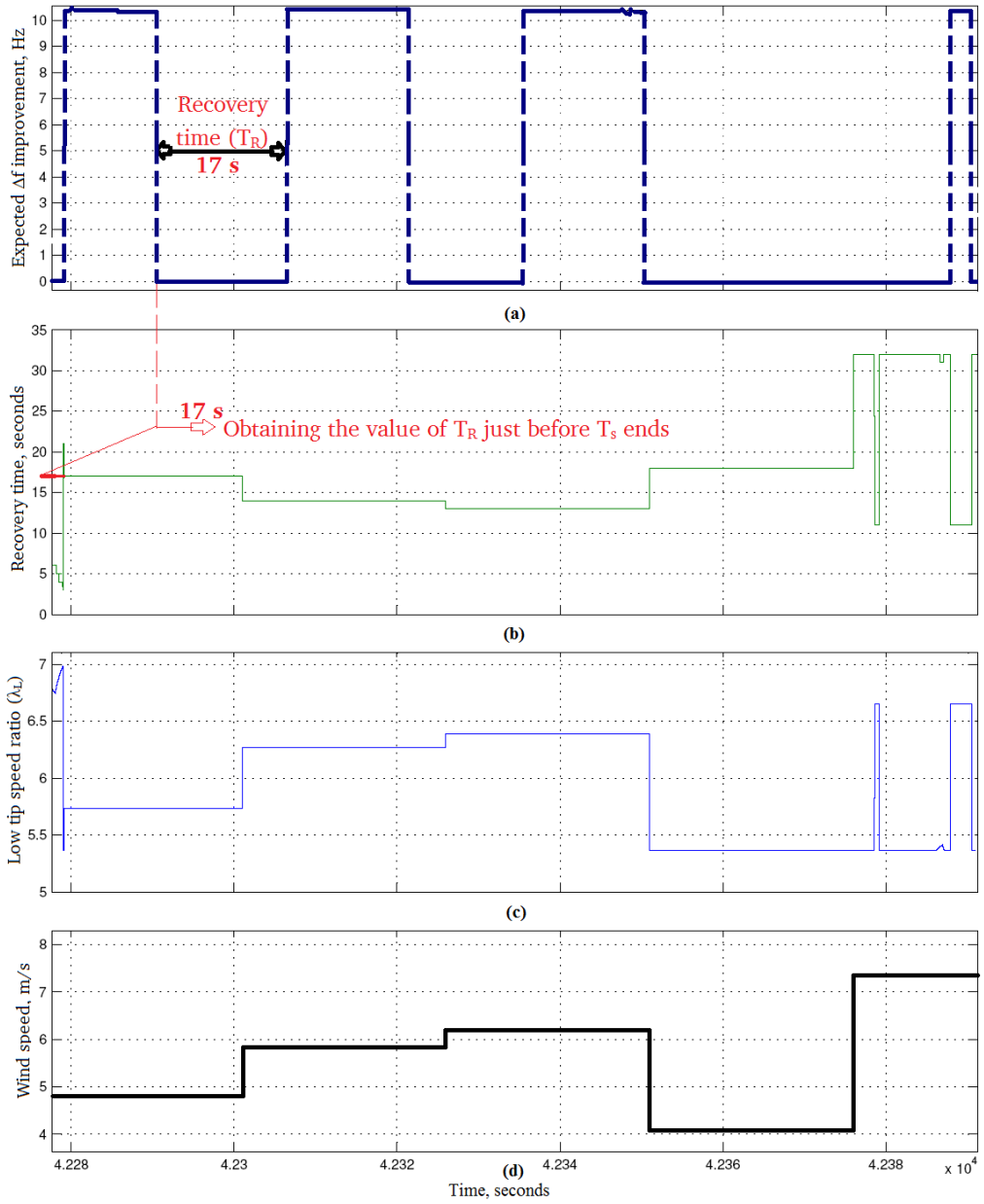

Figure 3.12 Case 3, event 5: a) frequency deviation improvement, b) t_R, c) λ_L, and d) WS

Figure 3.12 (a) shows that the expected Δf improvement increases after the gas plant is replaced by six WFs. This improvement is compared to the corresponding results achieved in [11], where two wind energy penetration levels were designated, namely 20% and 50%. This research work was selected for comparison because it integrated the same types of conventional generators, and was modelled in a similar method to that applied in this chapter. However, in [11], the 20% penetration level maintained a maximum improvement of 25 mHz for only 2 s. In contrast, the proposed technique reduced the frequency excursion by 11 mHz, but for about 10s at a lower WS and limited penetration level of 11%. Likewise, the 50% penetration caused only a 15 mHz improvement for 3 s.

It can be seen in Figure 3.12 (b and c) that lower values of λ_L (i.e., 5.3) caused a longer t_R (32 s) at a low WS. As an illustration, the gas plant replacement increased the burden on the WFs during the frequency drop elimination so that the WFs needed to inject more KE, hence the WTs speeds

decelerated to a lower λ_L. This forced the WTs into requiring a longer period of time to recover the default rotational speed at λ_H.

Figure 3.13 illustrates the different parameter variations in Case study 6, which focuses on the impact of applying a fixed value for 'M' and delaying the AGC signal. Consequently, it is preferable to concentrate on a short time range (e.g. ten seconds as in Figure 3.13) to emphasise the impact of λ_L variations on frequency deviation alleviation. Hence, displayed time interval is selected as it is characterized by a fixed moderate WS (7.8 m/s), so that proposed algorithm performance is analysed at constant WS. The essential difference between Figure 3.11 (a), Figure 3.12 (a) and Figure 3.13 (a) is the variation in the expected frequency deviation enhancement, because 'M' has a fixed value so that the frequency enhancement is totally dependent on WS and Δf signals. Generally, this would be considered to be a drawback for system operators, as they would be unable to forecast the WF's contribution during the frequency drop clearance process.

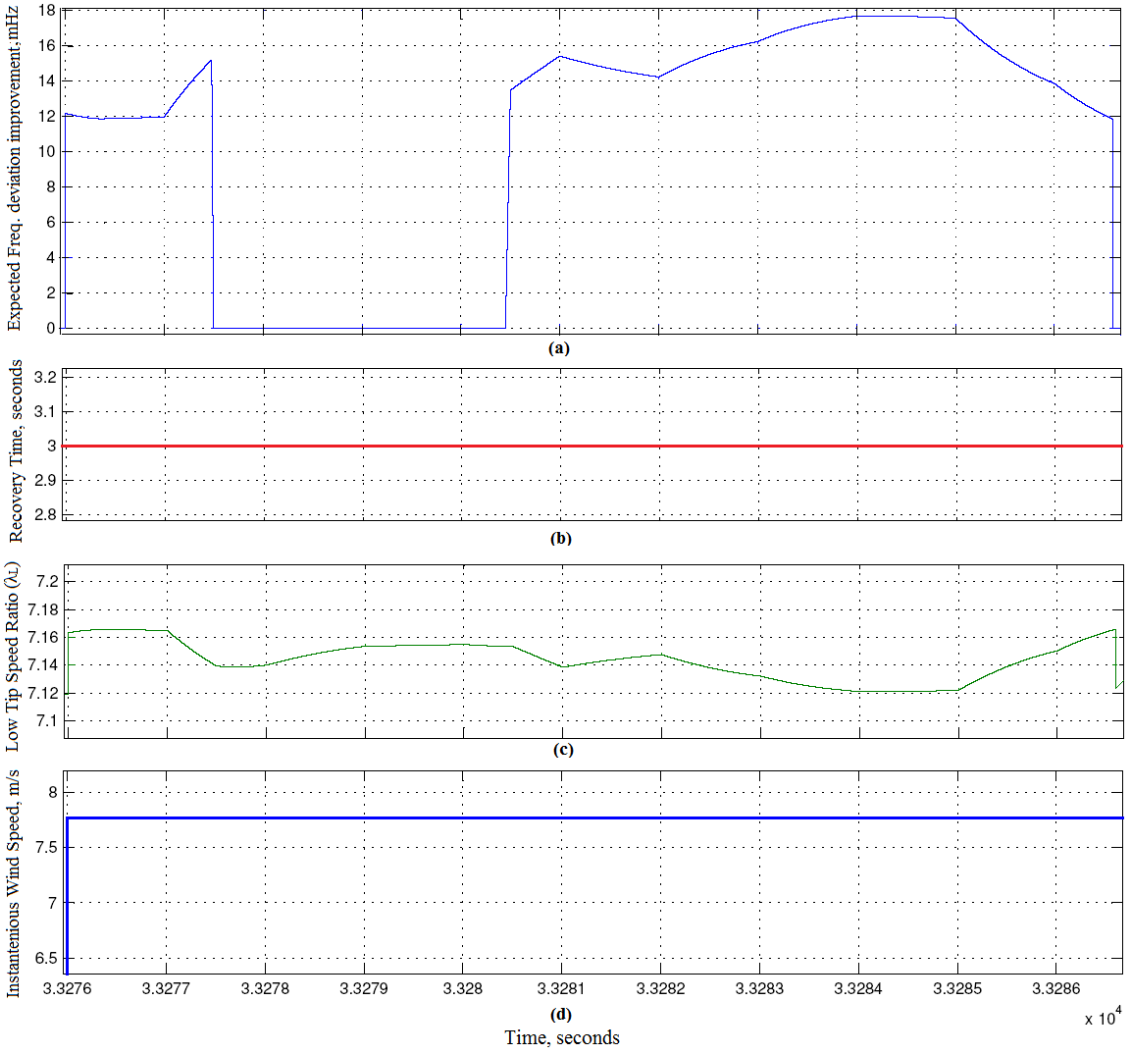

Figure 3.13 Case 6, event 4: a) Δf improvement, b) t_R, c) λ_L, and d) WS

Practically, this modification leads to higher amounts of extracted KE forcing the WFs to participate more positively in supporting the system during frequency drops, particularly when the fixed value of

'M' is reduced. Conversely, increasing the fixed value of 'M' saves a portion of the stored KE; hence, the WF(s) would be able to support the system if it suffered a second successive frequency drop after the major one within a very short time span. Moreover, the intended delay in the AGC signal could be an option for system operators if a system frequency drop incident overlaps with moderate or high WSs (i.e., relatively high WFs production), thereby attaining solid improvements in frequency excursion elimination and reducing stress on conventional units.

3.5. Summary

This chapter proposed an algorithm to control the extraction of KE during power system frequency drops, in addition to quantifying this KE and estimating the expected system frequency deviation curtailment. The offered algorithm integration with variable speed WTs proved to be feasible and practical, because it depends on special settings for the WT rotational speed. Moreover, some measurements signals are required as inputs, namely the instantaneous approximate WS and the system frequency deviation. The algorithm flexibility (i.e., it can be applied to any type of variable speed WT), coupled with its independency from pitch angle, are two acknowledged merits. The offered algorithm has been tested on a relatively medium capacity hypothetical system that includes the most dominant conventional generation types, in addition to detailed models of turbines and governors. More than 10% of the system generation capacity is replaced by wind energy in the four case studies. Results enable an insight into the feasibility of the offered algorithm, and reflect the achieved improvements in frequency response. In particular, wind energy integration has a positive impact on the system's response in most of the case studies, and in rare cases, it had a neutral or negative influence on some factors. The selection between constant or variable 'M' is a trade-off between reducing lost energy or triggering the optimum possible support (constant mode) on one side, and gaining a higher certainty in predicting system performance during frequency drops (variable mode) on the other side.

4. Method 2: Wind turbine de-loading/overloading[2]

The proposed algorithm has two operational modes, normal and support, which causes the WT to provide extra active power during frequency drops. The normal mode controls WT output through rotational speed and pitch angle adjustments according to the instantaneous WS category. Algorithm parameters are tuned based on WT specifications and average WS conditions in the WF location. The novel algorithm of normal operation ensures the positive contribution of WTs in the curtailment of frequency deviations, regardless of the instantaneous WS conditions. The innovative concept of merging pitch and rotational speed de-loading with overproduction deceleration is implemented to avoid continuous de-loading; hence, there is a reduction in the wind energy wasted. The WT generator is overloaded when a frequency deviation is accompanied by high WSs, and the amount of extra wind energy produced during frequency deviation clearance is then estimated at different WS conditions, including sever WS drops. An islanded medium capacity hypothetical system is then implemented to examine the proposed algorithm.

4.1. Proposed algorithm

WT operation is related to the rotational speed and pitch angle, with WS as the factor that is unable to be controlled. Controlled parameters are used in different operational regions so that the WT is always ready to contribute positively in the elimination of frequency drops. The operational regions are defined using certain WS categories with pivot values decided based on the WT type and the WS nature at the WF location. The WS categories are initially defined, and the normal and support operational modes in each operational region are then explained and illustrated using suitable figures and examples. The GE-77 embedded model in Simulink is applied, and it receives three inputs; WS, pitch angle, and rotational speed.

4.1.1. Wind speed categories

WS values that determine the operational regions of the proposed algorithm are defined according to the next procedure.

Firstly, the two main parameters are estimated, namely base wind speed (WS_B), and base mechanical rotational of rotor ($G\Theta_{base}$):

Base Rotational Speed ($G\Theta_{base}$)

This value is selected according to the WS nature in the WT location and is adjusted so that the WT produces the optimum allowed mechanical output power at the dominant WS conditions, namely the annual average WS in the concerned WF location (WS_{avg}). Note that values of $G\Theta_{base}$ are less than the

[2]Major content of this chapter is published in IET journal of Generation, Transmission and Distribution as indicated in Related publications list

maximum allowed GϽ according to WT specifications. In fact, the range of GϽ (in r/s) depends on the WT type and the installed converter specifications, as explained earlier in Subsection 2.2. In this chapter, WS_{avg} is 8 m/s and GE-77 has GϽ range from 1.15 rad/s to 2.51 rad/s [17]. Thus, maximum PWT_m at this WS is 0.47 pu, at $GϽ_{base}$=1.66 rad/s=1 pu. Thus, $GϽ_{max}$ = 1.51 pu and $GϽ_{min}$ = 0.69 pu.

Base WS (WS_B)

WS_B is the WS at which GϽ equals 1 pu and generating base power ($PWT_m = P_B$), which is less than 1 pu. P_B is assumed to be in the range of 0.65 to 0.75 pu at $GϽ = GϽ_{base}$.

Cut in WS (WS_{CI})

Below this value WS is too slow to run the WT, and therefore $PWT_m = 0$.

Low WS (WS_{low})

At this WS and $GϽ_{base}$, PWT_m is in the range of 0.2 to 0.25 pu.

High WS (WS_{high})

At this WS, $PWT_m \approx 1$ pu at $GϽ_{base}$ and a zero pitch angle. Note that, WS_{high} is not necessarily the WS_R mentioned by the WT manufacturer, as it depends on the suggested $GϽ_{base}$.

It is of note that based on comprehensive trials at different values for WS_B, it was found that $WS_{low} \approx 0.7 \cdot WS_B$ and $WS_{high} \approx 1.16 \cdot WS_B$. Numerical values for the imposed WS classes in this research work are presented in Table 4.1.

The offered algorithm is only applicable to WTs equipped with converters that allow rotor rotational speed variations and keep the grid connection at a fixed synchronized speed. It is therefore suitable for DFIG type 3, and full rated converter type 4 (e.g. Enercon 101).

Table 4.1 Major WS categories values in m/s

WS_{avg}	WS_{CI}	WS_{low}	WS_B	WS_{high}	WS_{CO}
8	3.5	6.5	9.5 (P_B = 0.7 pu)	11	25

4.1.2. Operational regions

This subsection explains the four operational regions that drive the WT according to WS classes, and each region has two modes (Normal and Support). The proposed algorithm makes a compromise between three methods to provide instant support during frequency events, namely pitch de-loading, decelerating overproduction, and temporary overloading. The levels of support in the first and second regions differ according to the WS conditions and WT specifications. Meanwhile, the overloading mode provides a fixed amount of power surge as long as the WS is above the predetermined threshold.

Pitch de-loading is illustrated by WT output reduction in relation to increasing the pitch angle. For instance, at a certain WS, WT output is 'X' at a zero pitch angle [91]. When de-loading is activated, the output power is adjusted to '$X \cdot (1-D_F)$', where D_F is the de-loading factor. Thus, the pitch angle is

adjusted through a closed loop controller, so that the WT output satisfies the de-loaded reference. In short, the de-loaded output is less than the 'zero-pitch' output (i.e., optimum power) by D_F%.

In addition, overproduction refers to forcing the WT to produce power exceeding the available PWT_m. The source of this extra power is the extraction of stored KE in the WT rotating parts. Therefore, overproduction leads to WT deceleration (i.e., GO decreases) and it must be stopped at certain critical GO_{min} to avoid loss of synchronism [80], or at a slightly higher value as explained later.

Region 1: WS < WS_{CI} or WS > WS_{CO}

The WT stops due to very low WS or to protect WT from excess mechanical stresses at very high WSs, consequently $PWT_m = 0$ in both cases.

Region 2: WS_{CI}<WS< WS_{low}

Normal mode

Pitch de-loading is deactivated ($\beta = 0$), GO =1 pu and PWT_m is evaluated using (2.1).

Support mode

Overproduction mode is initiated by adjusting the WT output reference to '$(1+2\cdot D_F)$ ·value of PWT_m at the initiation instant of support mode' at GO=1 pu. Using the D_F value in setting the overproduced power makes the size of the step increase in output power comparable to the corresponding rise in the case of de-loading mode commencement. It is of note that, no de-loading occurs in this category, and only the numerical value of D_F is considered. Overproduction continues until the frequency drop is cleared or until GO sinks to GO_{min}. Any deterioration of GO, and estimation of its instantaneous value, is described using (4.1). In brief, GO is fixed to 1 pu at normal operation and then starts decelerating just after the frequency drop occurs, which is accompanied by the steep rise in output power, as shown in Figure 4.1. After this, GO builds up again and returns to 1 pu after the WT is switched to normal mode. However, during the recovery process the WT output is reduced by 10% from the available PWT_m, so that the WT is able to accelerate to a GO_{base} as shown in Figure 4.1.

$$\frac{d\omega}{dt} = \frac{1}{J_{WT}}\left(TWT_m - TWT_e\right),\ TWT_e = \frac{PWT_e}{\omega} \qquad (4.1)$$
$$PWT_e = PWT_{m\ normal}\cdot(1+2\cdot D_F)$$

TWT_m and TWT_e are the mechanical and electrical torques respectively.

Region 3: WS_{low}<WS< WS_{high}

Normal mode

The output power is de-loaded by D_F calculated based on the required extra active power (ΔP_{WT}) from the WT during a frequency drop. Hence, it is preferred to calculate ΔP_{WT} at WS_{avg} to avoid worst-case

scenarios, if the actual WS is insufficient to produce the expected ΔP_{WT} when pre-estimated at a higher WS. Nevertheless, the value of D_F must not violate the SOs constraints. A compromised value is therefore reached to keep the WT support capability and maintain the output during normal operation at the required participation level by the SOs. Furthermore, reducing D_F mitigates any wasted energy and WT recovery time; whereas increasing D_F extends the positive impact of the WT on clearance of drops in system frequency. In addition, if WS exceeds WS_B then ω is allowed to accelerate up to ω_{max}.

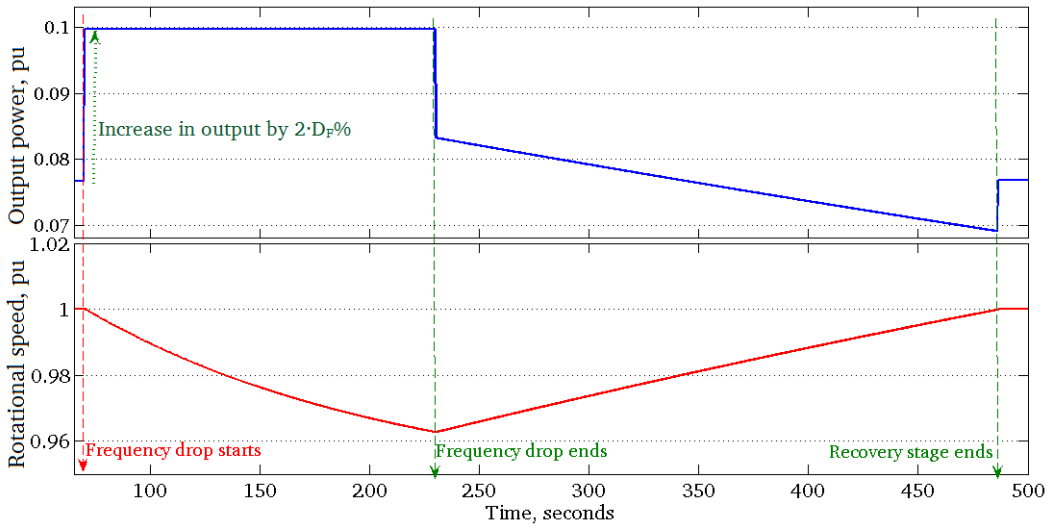

Figure 4.1 WT dynamics and production during support operation (WS=5.5m/s)

Table 4.2 Numerical values of pitch controller parameters

Parameter	K_p	K_i	K_4	Pitch rate, °/s
Value	4	40	0.25	8

$$PWT_{m\ pu\ \text{de-loaded}} = (1 - D_F) \cdot PWT_{m\ pu\ \text{normal}} \quad (4.2)$$

Thus, PWT_m increases, any wasted energy is reduced, and the amount of stored KE is increased (which is therefore considered as a strategic backup if the WS drops during support mode). In this research work, ΔP_{WT}=0.09 pu at WS_{avg} between WS_{low} and WS_{high}: namely, 8.75 m/s. Normal PWT_m at this WS is 0.59 pu at ω_{base}=1 pu, so therefore D_F should be 15%, as indicated by (4.2). The implemented pitch controller block diagram is shown in Figure 4.2, and its constants values are summarized in Table 4.2 [26, 92].

Support mode

De-loading is deactivated by setting the pitch angle to zero as soon as the frequency drop occurs. The most challenging part involved in this process is how the WT reacts when the WS drops within support mode operation. The solution depends on extracting the KE stored by the WT, so that former

output power is maintained for as long as possible until GƟ violates its threshold value. As an illustration, GƟ decreases until it reaches a lower value ($G\dot{\theta}_{stop}$), which is not by necessarily $G\dot{\theta}_{min}$. It should be highlighted that, $G\dot{\theta}_{stop}$ does not have a predetermined fixed value but is evaluated according to persisting conditions, (the new WS, the latest value of PWT_m, and the support ratio (S_R), as shown in Figure 4.3), whereas $G\dot{\theta}_{stop}$ is obtained using (4.3) in combination with the new value of PWT_m (i.e., PWT_m at slowest $G\dot{\theta}_{stop} \approx PWT_m$ at $G\dot{\theta}_{base}$ at the new WS) through the pre-obtained look-up table.

$$\omega_{stop} = S_R \cdot \omega_{stop} \text{ (slowest value obtained from look-up table at } PWT_m \text{ at the new WS)} \quad (4.3)$$

The term S_R decides how long the WT operates in the support mode; extracting a certain amount of the available KE, thereupon S_R is inversely proportional to the amount of extracted KE. Thus, increasing S_R ensures that $G\dot{\theta}_{stop}$ does not deviate far from 1 pu, which in turn mitigates the WT's role in eliminating the frequency drop by shortening the support time. In addition, the drop in output power is reduced so that possibility of a second minor frequency drop occurrence is limited. Accordingly, high S_R leads to a reduced recovery phase, as the WT requires less time to accelerate and settle again at $G\dot{\theta}_{base}$. This chapter particularly advocates unity S_R to achieve the longest support time during frequency drop elimination, and emphasises the influence of the proposed algorithm on the frequency recovery process. When the fault is not cleared and $G\dot{\theta} = G\dot{\theta}_{stop}$, the WT produces a non-de-loaded output to avoid a severe drop in supplied power during the fault (Path A, B, C and D). However, if the fault has already been eliminated, the WT returns to de-loaded operation mode (Path A, B, C and E) and accelerates to $G\dot{\theta}_{base}$. The variation in output power and rotational speed during a frequency drop at a fixed WS within the range $WS_{low} < WS < WS_R$ is shown in Figure 4.4. The pitch angle is adjusted to 2.4° to supply the required de-loaded power (0.32 pu). When the de-loading is later deactivated, the pitch angle drops to zero at the point of the frequency drop instant (support mode).

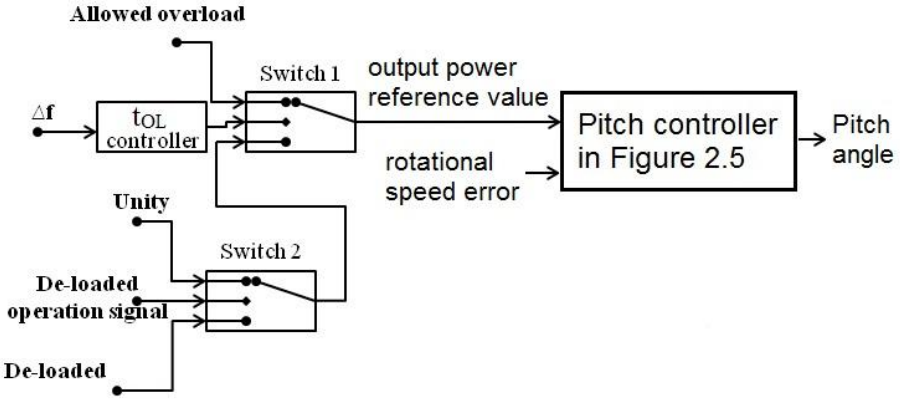

Figure 4.2 Implemented pitch controller

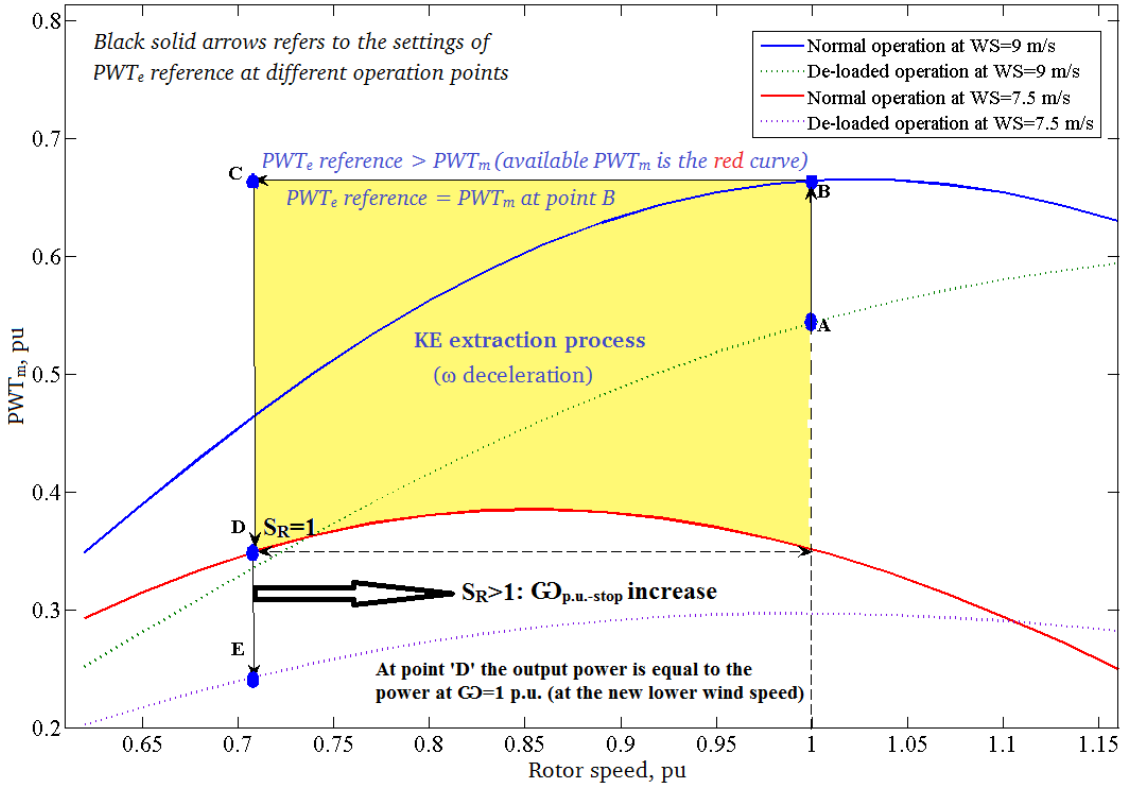

Figure 4.3 Operation algorithm during support mode if WS dropped (9 to 7.5 m/s)

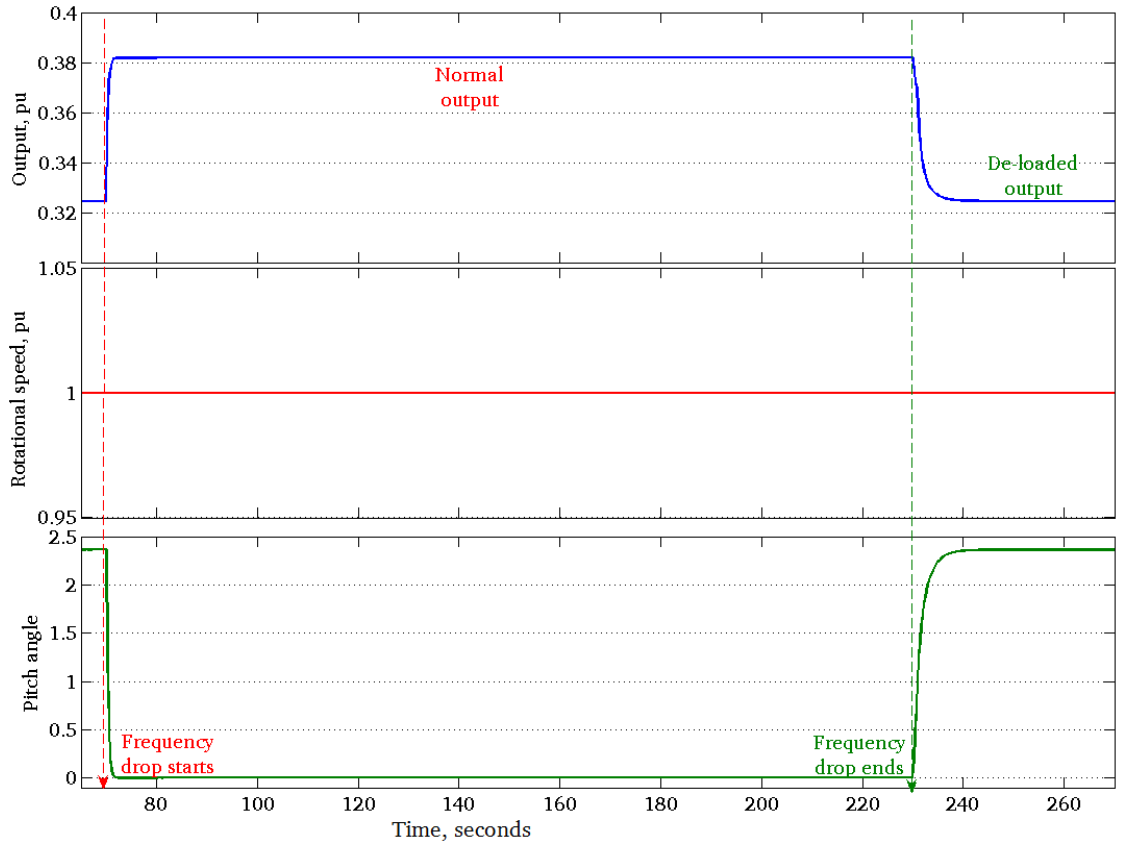

Figure 4.4 WT dynamics and output power during support operation (WS = 7.5 m/s)

Region 4: $WS_{high} \leq WS \leq WS_{CO}$

Normal mode

PWT_m is not de-loaded as there is sufficient WS to produce the WT rated power. It is therefore not preferable to waste energy by activating the de-loading technique. The WT is operated around ω_{max} and pitching is activated to limit the output power to 1 pu.

Support mode

At the start of the frequency event, the WT generator is overloaded by 10% to supply a power surge to the system for certain duration. This overload duration (t_{OL}) is predetermined by the SOs according to the generator specifications and its connections to the grid (t_{OL} is assumed to be 60 s in this chapter). An illustrative event is depicted in Figure 4.5, where the fault occurs at t=70 s, so that the pitch angle decreases until the output power is 1.1 pu. After t_{OL} ends, the pitch controller restores the mechanical power back to 1 pu by setting a suitable pitch angle. When the WS drops, the WT operates as described in the previous region's support mode. However, if t_{OL} ends before ω reaches the threshold value, the mechanical power is restored to 1 pu. (t=130 s) to avoid sudden drops in the supplied power. When the fault is cleared, or ω reaches the threshold value (t= 214 s), recovery stage starts. The recovery rate of ω depends on the new WS and the amount of reduction in output power (in this example output power is 90% of the available PWT_m). The WT needs about 300 s to accelerate to ω_{base}, afterwards β increases to achieve D_F (i.e., normal operation at the new WS region).

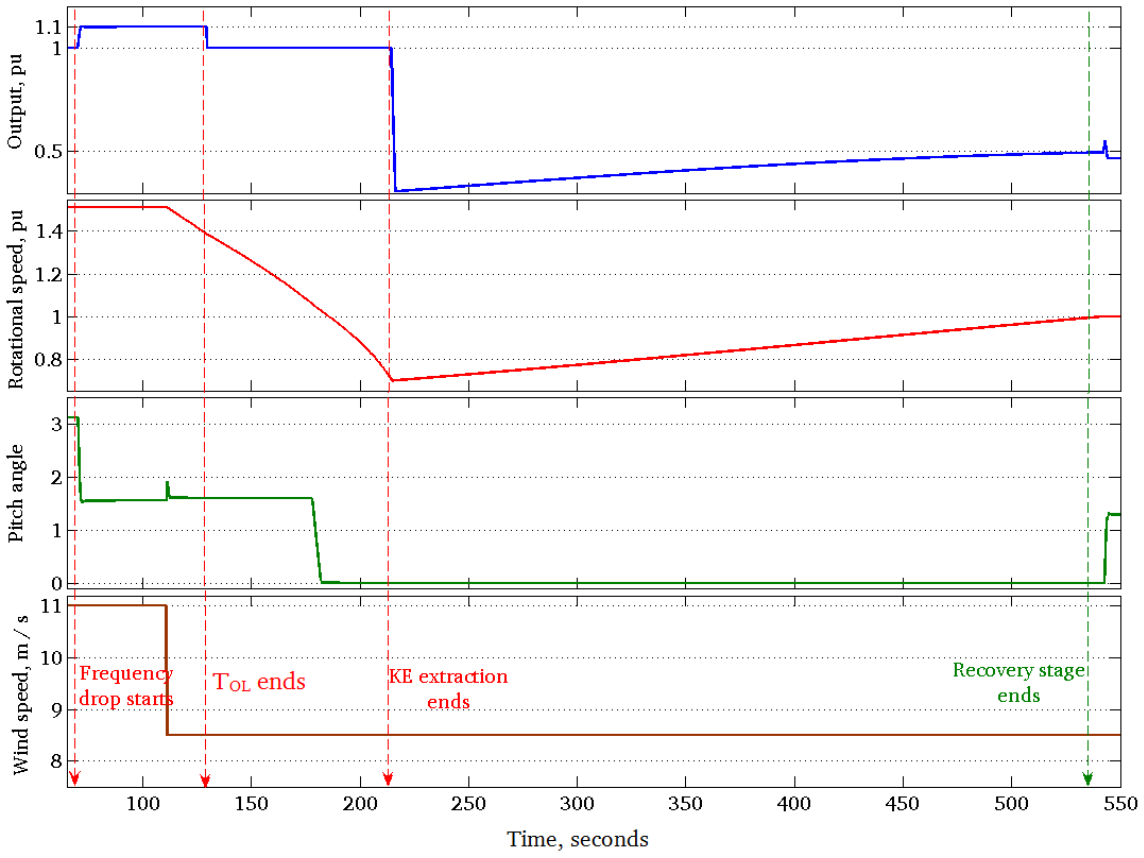

Figure 4.5 WT dynamics during support operation (WS =11 drops to 8.5 m/s at t = 110 s)

The major control stages and parameters involved in the offered algorithm, as well as the applied procedure to generate the prerequisite look-up table data, are presented in Figure 4.6. Construction of the two-dimensional lookup table is based on the least square polynomial fit and evaluation. The first step is to generate an output power array at a fixed WS, so that each output power corresponds to a given Ꞷ. The PWT_m and Ꞷ arrays are then input to the polynomial fit block to obtain an equation between the power and Ꞷ. Finally, a polynomial evaluation block is used in combination with a power array of increasing steps in pu (e.g. [0.1 until 0.7 in 0.05 steps), to evaluate Ꞷ corresponding to each point in the power array. This process is repeated for all WS values found in the range of the third operation region. In addition, the whole process is summarized in Figure 4.6 in the blue bordered area, and Figure 4.7 depicts a compact flowchart for the main stages of the proposed algorithm.

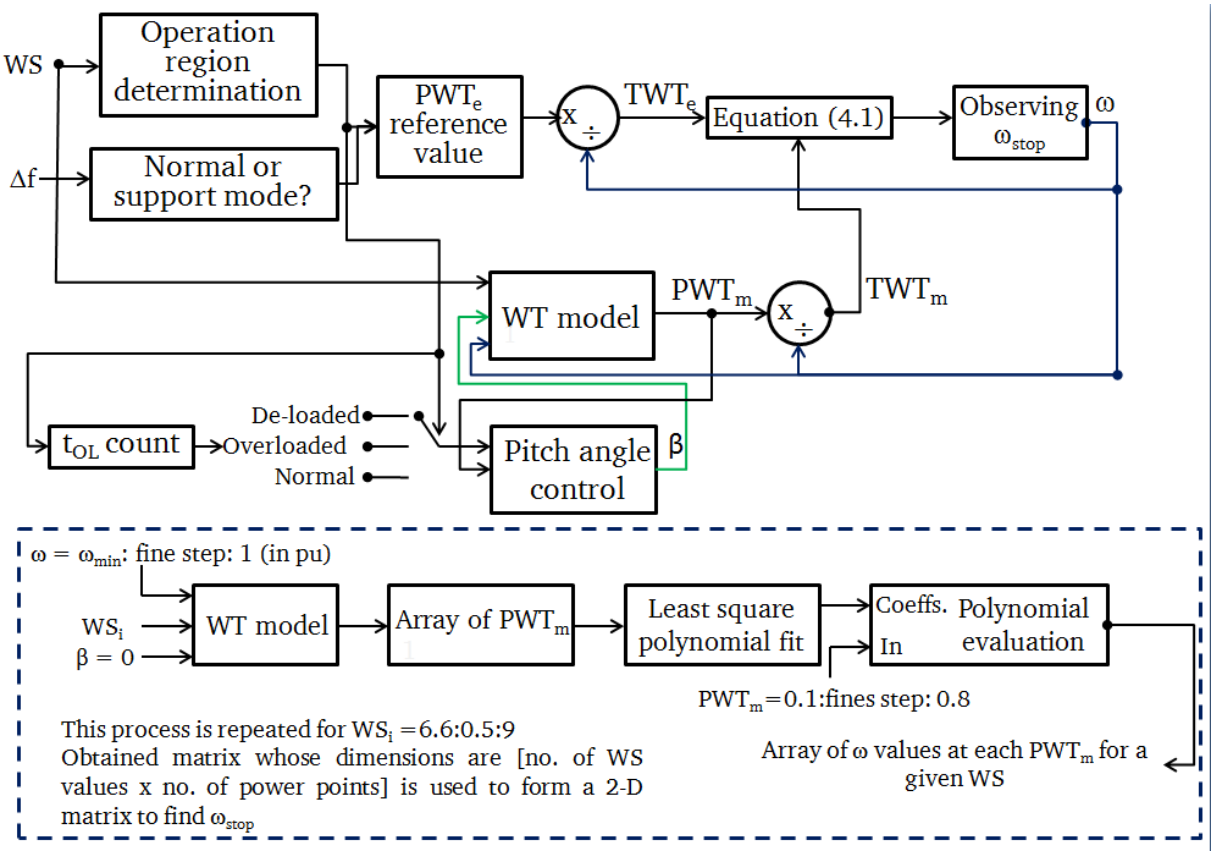

Figure 4.6 Control blocks integrated in proposed methodology

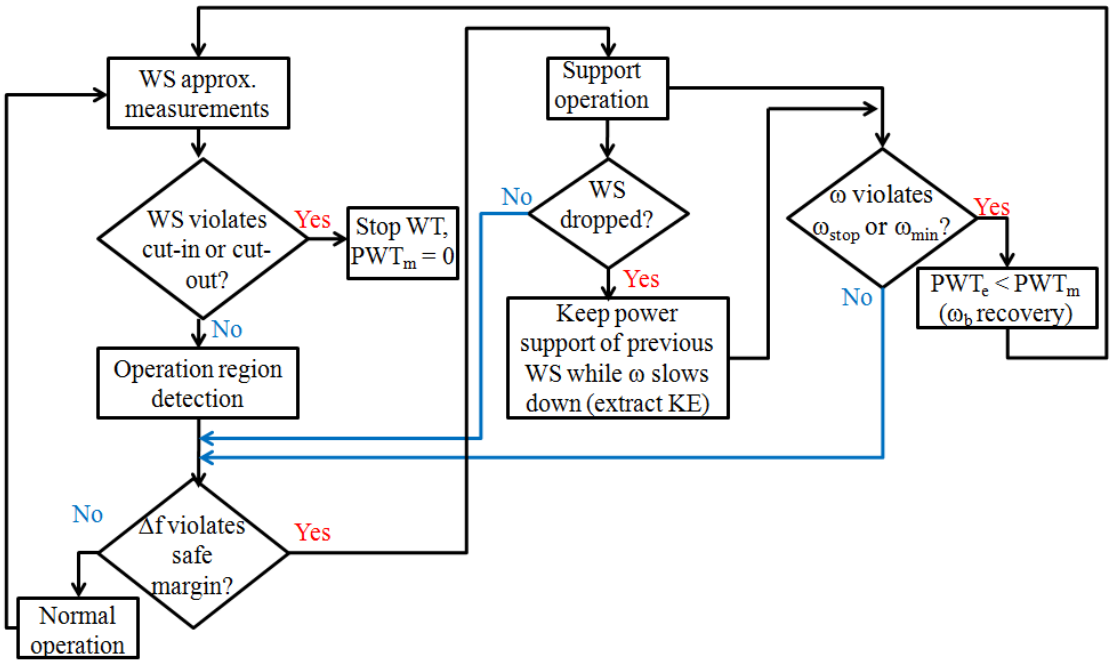

Figure 4.7 Algorithm main stages flowchart

In brief, the practical application of the proposed algorithm has no restricted limitations, as it can be applied to any WT type at any WF location. However, major disparities arise in the numerical values of the WT base rotational speed and values of pivot WSs, which represent the operation regions borders. It is of note that the presented algorithm partially depends on acquiring the incident WS magnitude, hence the impact of non-precise WS measurements should be acknowledged in future work. As an illustration, the WS value has two functions: firstly, to denote the operation region selection according to the category in which the instantaneous WS is located, and secondly to evaluate $GƆ_{stop}$. Therefore, slight errors (e.g. up to 10%) in WS measurement has no critical influence either on the two previous purposes or on the whole process. After all, the use of well placed, fast, reliable electronic anemometers that are well distributed inside the WF terrain would marginalize the possible errors, and could be considered as a valid and economical solution.

4.2. Case studies

This section presents a description of the examined case studies, and these are divided into two branches. The first branch deals with the impact of WS magnitudes and variations on the amount of extra supplied energy during the elimination of frequency drops. The second branch applies the proposed support algorithm to a WF connected to a hypothetical system of medium generation capacity.

4.2.1. Case study 1: Support energy estimation

This section evaluates the amount of extra energy released ($E_{support}$) by the WT in support mode using (4.4), where t_{start} and t_{end} are the beginning and end instants of the frequency support phase. The injected support energy is calculated within 90 s of the frequency drop initiation instant.

$$E_{\text{support}} = \int_{t_{start}}^{t_{end}} (PWT_{\text{support}} - PWT_{\text{normal}})\, dt \qquad (4.4)$$

This estimation is performed for all WS regions at specific WSs. Two events are used to examine the impact of WS variations on the amount of released energy, within the execution of the frequency recovery algorithm. The first event imposes a sudden drop in WS from 11 m/s to 8.5 m/s (i.e., WS drops down one category from the fourth to the third category) while the WT is already operating in support mode. In both cases, the WS changes after 40 s from the frequency drop occurrence. The 40 s duration is selected to be certain that the WT has depleted a high ratio from the stored KE at the former WS. In addition, it gives a suitable time span for the WT to stabilize in support mode of the initial WS before it switches to a new operation region after the WS drops. However, shortening or extending this period directly affects $E_{support}$.

4.2.2. Case Study 2: Implementation using a hypothetical system

Two power plants, namely hydro- and steam-plants represent conventional generators feeding a constant load, as in Figure 4.8. In all cases, the system suffers a typical sudden load demand rise of 10% from its normal load after 250 s, causing a moderate frequency deviation. The extra energy released from the conventional generators is therefore compared to the corresponding energy injected by the WF. Furthermore, the proposed support algorithm impact on frequency performance is analysed by comparing the system frequency responses in four case studies. **Case 2A** represents the default system without wind energy integration (conventional generators **ratings** are 300 and 200 MW as shown in Figure 4.8). The initial load is 360 MW and it is shared between the two conventional generators based on their ratings (i.e., steam and hydro plants feed 216 and 144 MW respectively, hence both plants are loaded by 72%).

In **Case 2B**, the conventional generation capacity is reduced by 25% (the new conventional generators ratings are indicated in Figure 4.8), and replaced by a WF. However, both technologies are not reduced by the same ratio so as to focus on the impact of a generation mix with dominant steam generation technology. The examined 'hypothetical' system is suitable for emphasising the impact of the proposed algorithm, but this system has relatively lower overall inertia compared to larger interconnected grids. This imposes a higher burden on the contribution of the WFs to frequency recovery. In addition, the system has a medium generation capacity; hence, a medium-high penetration level of WFs in an upgraded capacity could be achieved by a reasonable number of WTs. Most large interconnected systems are composed of a certain number of thermal- and hydro-generators, and thermal generators prevail; they therefore have a greater share in the generation capacity, which is similar to that of the proposed case study. The transmission lines and the transformers are always marginalized to reduce computational and simulation time and effort. In addition, the impact of these

components on system frequency is minor [10, 52]. Therefore, most literature involved in this research field prefers to model power systems as a single bus; focusing on precise simulating models for turbine, generators, governors, system inertial response, and load dynamics. However, due to the WS fluctuations, it is impractical to consider the full rated power of the WF within scheduled power generation. It is therefore assumed that the reduced capacity of the conventional generators equals 50% of the WF's rated capacity [5, 82]. As an illustration, the replaced conventional capacity is 130 MW; hence, a WF with an almost 260 MW rated capacity is required. In addition, the WS is assumed to be fixed through the whole WF terrain, and therefore the WF output is equivalent to the output of one WT multiplied by the number of WTs operating in the same mode.

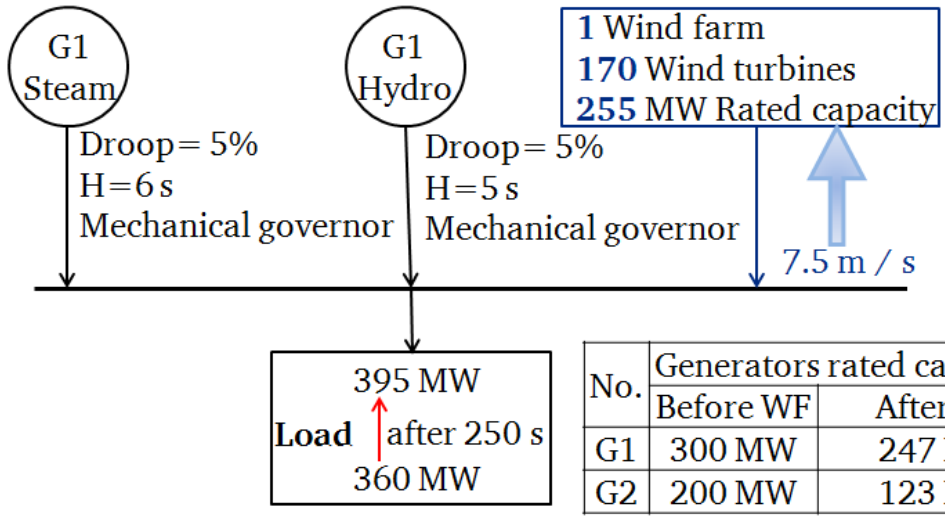

No.	Generators rated capacities	
	Before WF	After WF
G1	300 MW	247 MW
G2	200 MW	123 MW

Figure 4.8 Implemented test system, including the integrated WF

The WTs installed in the WF will be divided into two groups of normal and support mode operation according to the dispatching methodology (explained later in this subsection). However, in Case 2B the WF supplies a fixed output (i.e. at WS = 7.5 m/s, aggregated MPT output is 92 MW, equivalent to 26% of the supplied load) and is not equipped with the proposed support algorithm. It therefore does not react to frequency events. In contrast, in **Case 2C** the WTs follow the proposed algorithm but have no dispatching method. Finally, **Case 2D** implies a simplified dispatching method because the simulation curves in Case 2C showed that frequency undergoes tough oscillations as it approaches the safe margin. Therefore, applying a simple dispatching technique to overcome this problem is a prerequisite, although the proposed dispatching technique plays no role at normal operation. Thus, the entire output from the WF is injected into the system during normal operation.

The dispatching method has three levels: 1) when the frequency drop is worse than -0.1 Hz, and the whole WF is switched to support mode; 2) when the frequency drop is in the range of -0.075 to -0.1 Hz, and 30% from the WF is switched to support mode (i.e. almost 56 WTs); and 3) when the frequency drop is in the range of -0.055 to -0.075 Hz, and 10% from the WF is switched to support mode. This criterion is designed based on comprehensive trials, and frequency drops borders are considered as a heuristic selection. In all case studies, the incident WS is 7.5 m/s, which is the average

WS in many WF locations. Moreover, AGC activation is delayed by 13 s to emphasise the influence of the WF's participation in frequency deviation elimination. The same detailed modelling approach for conventional generation that is implied in the previous chapter is applied.

4.3. Results and Discussion

The results of case studies are analysed in separate subsections where the major comments and outcomes are summarized and discussed.

4.3.1. Case study 1

$E_{support}$ at a given WS reflects a WT's capability of contributing sufficiently during frequency drops curtailment. According to Table 4.3, the maximum $E_{support}$ is achieved when the WS drops from 11 to 8.5 m/s. The applied algorithm forces the WT to keep generating power at the level reached at the initial WS (i.e. 11 m/s in this case) for certain duration, depending on ω_{stop}. This overproduction stage depends on extracting a portion from the stored KE in the WT. In brief, the proposed algorithm releases the full amount of extractable KE when the incident WS drops which explains why it is preferable to run the WT at the highest allowed ω. As an illustration, running the WT at high ω gives the opportunity for the WT to store more KE, which then acts as useful reserve if the WS drops during support operation mode, so that the WT supplies the former output power for as long as possible, regardless of the new lower WS. These outcomes reinforce the claim of the author that the negative impact of WFs integration on system performance during frequency events is neutralized, and even barely improved, if the WS drops during frequency recovery, although the level of improvement depends on the severity of both the frequency excursion and WS drop.

At 5.5 m/s, the WT produces extra electrical power proportional to the available mechanical power during support mode. The low amount of available mechanical power causes a low step rise in the support output. Therefore, the amount of released KE is reduced, and ω requires a longer time to slow down to ω_{min} as in Figure 4.1. Nevertheless, it is possible to increase the amount of KE extracted by setting the support electrical power to a higher value, but this can only be sustained for a shorter time due to the rapid deterioration of ω.

At 11 m/s, the WT supplies its rated output, and it is therefore theoretically unable to support the system in the curtailment of frequency drops. Nevertheless, the overloading principle can be used as a practical solution during such a condition. The permitted overload ratio and duration play a basic role in determining the amount of delivered support energy. However, the amount of injected KE in this case is almost similar to the amount of support energy when the WS is 7.5 m/s. The major advantage in cases of high WS is the sustainability of injected energy, as it can be supplied as long as the incident WS is high enough. Another advantage is that it avoids any slowing down of ω, so that the WT retains its normal operation directly after frequency drop clearance.

In general, these results do not mean that WT participation in frequency excursions is more satisfactory if the WS drops during support mode operation. On the contrary, the proposed algorithm targets mitigate the drawbacks of a drop in WS while the system is suffering a frequency deviation. This problem is solved for a limited duration, which is the time consumed by the WT to inject the available support energy. Afterwards, the system faces two possible risks, namely, a further drop in WS or a second consecutive influential frequency deviation. If one of these two risks (or both) occurs, the WT will be unable to offer any positive contribution in the elimination of the frequency deviation. In other words, the presented results ensure the merits of the proposed algorithm if the incident WS drops within a short duration just after the initiation of the frequency excursion, for example at 90 s or longer based on WS conditions and WT specifications. This duration is considered to be critical in eliminating a frequency drop, as most of the primary and secondary responses of conventional generation occur within this time span, and any redundant disturbance in supplied power causes further frequency excursions.

4.3.2. Case study 2

The tolerated frequency deviation in this case is about 0.1% of the nominal frequency (i.e. ±0.05 Hz) [93]. A comprehensive comparison between the frequency responses of Case studies 2A to 2D is conducted in Figure 4.9. Δf_{max}, Δf_{10s}, t_{SM}, and the root mean square value of Δf within 180 s (Δf_{RMS}) are evaluated. These parameters clearly reflect the impact of wind energy integration on the frequency responses in the examined cases.

The frequency curves are displayed in Figure 4.9, and the considered parameter values are gathered in Table 4.4. It is obvious that the worst response occurred after the WF was integrated without any support provided (Case 2B). This case has the worst Δf_{RMS}, Δf_{10s} and Δf_{max} and longer t_{SM} in comparison with the base case. The replacement of conventional generation with a power source that is incapable of supporting the system during frequency excursions caused these problems. However, use of the proposed algorithm improved the performance, in particular values of Δf_{10s} and Δf_{max}.

The fast response of the pitch controller, which switched the WF output from de-loaded condition to optimum condition, reduced Δf_{max} by 39 mHz, and Δf_{10s} by 13 mHz. It should be highlighted that the WF provided a 12.42 MW power step within about 1 s, which is the time taken for the pitch angle to drop to zero. This power step represents 34% of the load step that caused the frequency event. In addition, this support is provided when Δf violated the safety margin, and not immediately at the instant of the load sudden increase. The WF provides optimum output until the Δf enters the safe region (i.e., the support lasts for t_{SM}). The frequency curve suffers considerable fluctuations in Case 2C when Δf approaches the safe margin. As an illustration, switching the whole WF at the same time from support mode to normal mode causes further minor frequency drops. Hence, the frequency violates the safe margin again, thereupon the WF switches to support mode again, and thus Δf returns back to a safe region. This sequence is repeated until the conventional generation governor and the AGC signal

settle down to the new settings that are suitable for the new higher load. In contrast, the simplified dispatching method obviously suppressed these fluctuations. However, it caused a minor drop at 253 s when Δf crossed the -0.1 Hz border, hence 70% of the WF switched to de-loaded mode so that the support power dropped to 3.73 MW. In spite of the fluctuations in Case 2C, t_{SM} is not as late as it is in Case 2A, and is shorter by 2 s than Case 2D, due to the full support of the WF and not only from certain dispatched sections within it. According to the results of t_{SM}, the WF support plays a major role within the first 10 s; hence, Δf_{max} and Δf_{10s} are the parameters most affected. Meanwhile, t_{SM} is not as influenced by the WF support algorithm (i.e. Cases 2B and 2C have the same t_{SM}). In general, the replacement of conventional generation with WF extends t_{SM}, but if the WF provides suitable support then the severity of the frequency drop is mitigated. On the other hand, it is noticeable that there are minor differences in the Δf_{RMS} values between the case studies, and the highest values are recorded in Case 2B, as expected.

Table 4.3 Values of examined parameters

WS, m/s	5.5	7.5	11	11 drops to 8.5
$E_{support}$, kWh	0.87	2.15	2.5	13.6

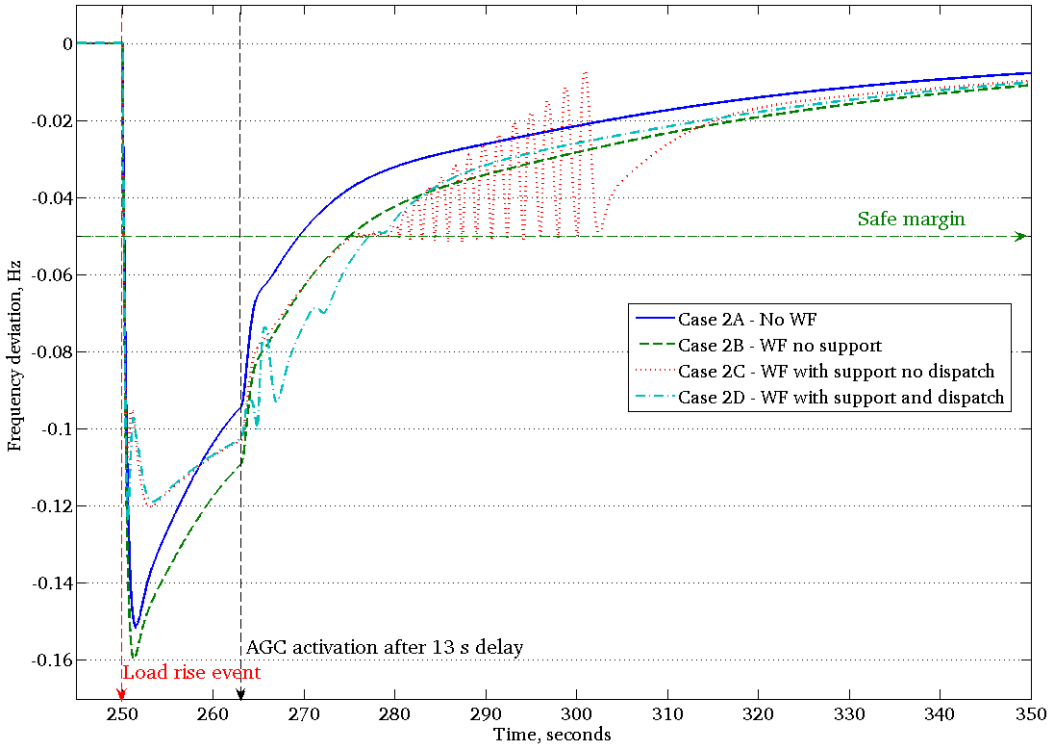

Figure 4.9 System frequency responses of all case studies

Table 4.4 Parameter values examined

Case study	**Case 2A**	**Case 2B**	**Case 2C**	**Case 2D**
Δf_{max}, mHz	151	159	120	124
Δf_{RMS}, mHz	37.43	43.18	39.36	39.74
Δf_{10s}, mHz	108	121	108	106
t_{SM}, s	20	23	23	25

Finally, it is interesting to compare the amounts of extra energy supplied from a steam plant and a WF within t_{SM}. These amounts of energy are thus compared to the normal energy supplied by each source within the same duration. The WF supplies normal energy of 82.76 MW at the given WS, which means 574.72 kWh within t_{SM}. In addition, it supplies 99.45 kWh of extra energy to participate in frequency drop curtailments; hence, its contribution is 17.3% of the nominal generation within the frequency drop high-risk period. Likewise, the steam plant participates 5.9% from its nominal production. Consequently, the proposed algorithm gives the WF a better capability of anticipating frequency excursions, corresponding to that of a conventional plant, particularly during its early risky stage. Moreover, the incident WS determines the support power step magnitude and the maximum duration within which the WT can sustain this power step.

4.4. Summary

This chapter offers a detailed algorithm for making a positive WT contribution to the elimination of system frequency excursions. This algorithm relies on several modifications within the dominant normal operation of a WT. In particular, three different approaches are implemented: de-loading, overproduction, and overloading. The triggering of each technique depends on the incoming WS according to predefined categories. Results prove that the extra supplied power is sufficient to enhance the system performance during frequency drops. In addition, it reduces the negative impact of the WS slowing down during support mode operation, and therefore accepted support is guaranteed regardless of poor WS conditions. The proposed algorithm was proven to be useful when the WS immediately fell from a certain category to a lower one, as the sudden decrease in the WS is shown to be neutralized and does not aggravate the frequency excursion. Moreover, the proposed algorithm partially solves the problem of wasting high amounts of wind energy using traditional de-loading techniques, by the continuous operation of the WT in de-loaded mode, because the de-loaded operation is activated only at certain WS category. Implementing the proposed algorithm on a hypothetical system showed a clear enhancement of system performance during its recovery from a moderate frequency deviation. In addition, a comparison of the contributions between a WF and a conventional generator reflected the WF efficient contribution.

5. Comparison of proposed support methods

The supportive role of WTs during frequency drops proposed by many algorithms causes the WT to deviate from delivering optimum power generation. Special operational methods drive the WT to guarantee the availability of reasonable power support when the system suffers frequency deviations. This chapter compares the two algorithms offered, as well as the standard de-loading technique widely proposed in literature. Wind turbine power curves for each algorithm are then derived, and a comparison is conducted from the point of view of wasted energy with respect to optimum power generation operation. This analysis is performed in two locations that are considered to be promising candidates for WFs construction in Egypt, and uses an integration of two different types of WTs.

5.1. Maximum power tracking operation:

The WT output power depends on three variable parameters; rotational speed, WS, and pitch angle, as illustrated before in Subsections (2.1) and (2.3). Consequently, the optimum tip speed ratio that achieves an optimum C_p of each WT type is determined. The WT rotational speed is adjusted so that C_p tracks its optimum value at all times. This constraint is fulfilled by continually adjusting the value of rotational speed so as to maintain the optimum tip speed at all WSs. The question now is how to simulate the estimation of the optimum power value at each WS according to MPT operation. This chapter represents two different approaches for obtaining WT performance curves that fulfil the MPT.

5.1.1. Manufacturer power curve (MPT 1)

The WT fabricating company provides a standard power curve for each WT type where the WT output at each WS is indicated within a margin between WS_{CI} and WS_{CO}. These power values are based on continuous monitoring for WT performance, and are the average of several records taken at each WS. The power curve data can then be manipulated into a lookup table using an appropriate interpolation method; hence, the optimum WT output can be estimated at any WS. The most critical region in this curve is between WS_{CI} and WS_R, elsewhere the output is rated (i.e. 1 pu), or zero, according to the WS.

5.1.2. Optimum power evaluation using C_p equation (MPT 2)

This method aims to minimize possible errors in MPT 1, and relies mainly on the WT model and C_p equation constants. It is well known that a variable speed WT has a certain range of rotor speeds that are predetermined by the manufacturer. Therefore, the control algorithm derived for the WT should not violate these limits by any means in order to avoid any possible loss of synchronism or physical damage. In this proposed algorithm, the output power at a certain WS is evaluated using (2.1) and (2.3) at all feasible rotor speeds. Thus, the maximum (i.e. optimum) possible output power is determined at each WS starting from WS_{CI} until WS_R. However, the step between two successive WSs (i.e. the WS class; for example if the WS class equals 0.5 m/s the examined WSs are WS_{CI} + 0.5, WS_{CI}

+ 2×0.5, WS_{CI}+ 3×0.5,…., WS_R+ 0.5) contributes to the accuracy of the obtained look-up table. In other words, reducing the WS class mitigates the role of the applied interpolation method, thus reducing error. Illustrative Figures are provided in Subsection 5.5, based on the considered case studies.

It should be highlighted that application of the MPT algorithm makes the WT incapable of providing additional active power support during frequency excursions. However, alternative solutions depend on energy storage mediums, as discussed later in Chapter 8.

5.2. Frequency Support techniques

This section briefly explains the WT's operation during over-speeding (Method 1), de-loading, and the proposed innovative partial de-loading support technique (Method 2). In addition, it explains the method used to construct the WT performance curves in normal operation according to each algorithm.

5.2.1. Over-speeding operation (Method 1)

As mentioned before, the contribution of a WT in frequency drop curtailments may rely on the amount of stored KE in its rotating parts. The algorithm offered in Chapter 3 maintains a higher value for the tip speed ratio, hence the rotor speed increases, and in turn, the available KE is enlarged. In particular, λ_H evaluated in (3.3) is applied. In sequence, the WS, rotor speed, and pitch angle are used to estimate WT output using (2.1) to (2.3). It is of note that over-speeding is valid only in the range of ($WS_{CI} < WS < WS_R$). As an illustration, starting from WS_R the WT operates around its maximum rotor speed, thus it is unable to cause the WT to over-speed or to violate the rotor speed limits.

5.2.2. Standard de-loading operation

A WT is operated so that the WT output is less than the optimum available power. Thus, the deficit between the actual output power and the optimum output is considered as a strategic reserve to support the system during frequency deviations. As mentioned in Subsection 2.3.2, de-loading can be applied, mainly by using two techniques:

- Running the WT at a rotational speed higher than the optimum speed (note that the optimum speed is the speed which leads to $\lambda = \lambda_o$). This method is called WT over-speeding.
- Activating pitch control at all WSs so that the output is reduced according to the implied pitch angle. This technique is applicable for any WT equipped with pitch angle controls. However, pitching is a slower alternative due to the mechanical response of servo motors controlling each blade pitch angle.

In both techniques, a predefined de-loading factor (D_F) is selected by SOs according to their requirements of the WFs contribution to mitigating frequency drops. In this chapter, D_F= 15% and the minor differences between the two sub-techniques are ignored (i.e. WT de-loaded generated power is the same in both sub-techniques).

5.2.3. Partial de-loading algorithm (Method 2)

The major merits and uniqueness of this algorithm appear in three factors: 1) it is adapted with the WT and WS conditions within the WF location; 2) the de-loading is activated only within certain ranges of WS, as explained in Subsection 4.1.1 (de-loading is applied in the following conditions: 1) WS_{low}< WS < WS_R and 2) normal PWT_m is less than 1 pu; and 3) its capability of handling WS drops intersecting with frequency events, thereby reducing the negative impact of such sudden dips in WS.

5.3. Wasted energy assessment

This section explains the method used to estimate the amount of generated energy by a WT within a certain time span, according to a given chronological WS array. These energies are estimated to judge how much energy is wasted in the discussed frequency support algorithms. WS chronological arrays in certain locations are considered as an input to the constructed look-up tables, so that the amount of generated wind energies within the concerned time spectrum is estimated using 5.1 to 5.4 (i.e. WS chronological array must be available within a considered interval). E_{MPT1} and E_{MPT2} stand for generated energies within a considered time span (T), when the WT operates based on MPT through the methods explained in Subsections 5.1.1 and 5.1.2 respectively. E_{OS}, E_D, and E_{PD} stand for the generated energies when the WT operates using over-speeding, de-loaded, and partially de-loaded strategies, respectively. The time step (i.e., time duration between each two successive WS records) of the available chronological WS array is t_{WS}, and N is the number of WS records within T. WT output is evaluated based on the performance curves of the WT type and the acknowledged operation algorithm. However, the transients occurring during the shift from one WS to another are ignored because they have a minor impact on the overall energy generated. Generally, energy is the integration of power during time. As the time deficit between each two successive WS records is fixed (i.e. t_{WS}), the energy produced at each WS record is equivalent to the product of PWT_m and t_{WS}. Meanwhile, PWT_m is de-loaded all the time in a continuous de-loading operation; hence it equals '$PWT_m \cdot D_F$'. Consequently, equation (5.2) is valid. The amount of wasted energy is calculated with correspondence to E_{MPT2}, for example the difference between E_{MPT2} and E_D represents the wasted energy due to integration of the continuous de-loading algorithm.

$$E_{MPT1} = \sum_{n=1}^{N} PWT_{m-MPT1\,n} \cdot t_{WS},\ E_{MPT2} = \sum_{n=1}^{N} PWT_{m-MPT2\,n} \cdot t_{WS} \quad (5.1)$$

$$E_{OS} = \sum_{n=1}^{N} PWT_{m-OS} \cdot t_{WS} \quad (5.2)$$

$$E_{D} = E_{MPT2} \cdot (1 - \frac{D_F}{100}) \quad (5.3)$$

$$E_{PD} = \sum_{n=1}^{N} PWT_{m-PD} \cdot t_{WS} \quad (5.4)$$

5.4. Case studies

To emphasise the impact of WS conditions and WT types on the wasted energy in each operation algorithm, two different locations and two WTs types, namely Gameza-90 (G - 90) and GE-1.5 MW (GE-77), are involved in the presented analysis. The power performance curves of both types in the case of MPT are displayed in Figure 5.1. Two locations are selected from WF candidate sites according to the Egyptian authority of new and renewable energies, namely Nabq and Ghareb. These two sites are dissimilar in WS conditions; Ghareb is characterized by high WS_{avg} in contrast to the Nabq location, as indicated by Table A.5 in the Appendix. The energies generated from the two different types of WTs are estimated to calculate how much energy is wasted using continuous and partial de-loading techniques. Available WS data are the average WSs recorded every 10 min within one year (i.e. 52560 WS records/year in each location), hence T = 1 year and t_{WS} = 10 min.

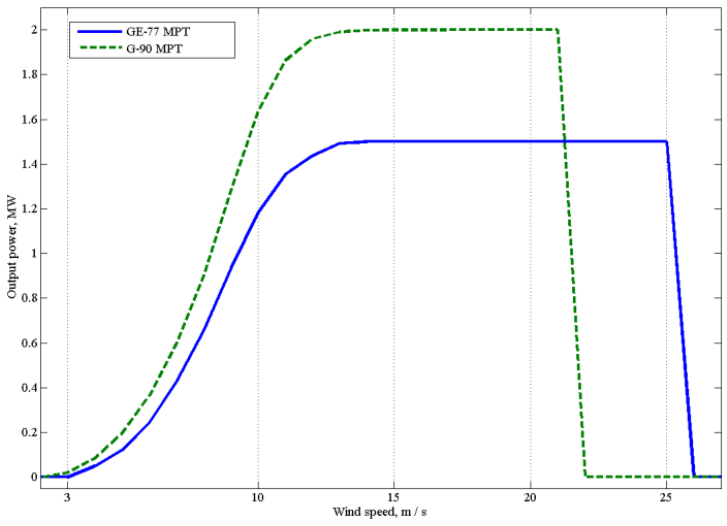

Figure 5.1 Manufacturer power curves of GE-77 and G-90

5.5. Results and discussion

5.5.1. Performance curves comparison

Firstly, the pivotal parameters of the proposed partial de-loading algorithm clarified in Subsection 4.1.1 are investigated in the two locations with respect to the two WTs types. Because no large difference exists between the dimensions and ratings of the WTs, no huge deviations are seen in the parameter values, as depicted in Table 5.1. For example, the difference in ω_{base} between G-90 and GE-77 is only 0.09 r/s, in favour of G-90. Likewise, the WS_B of G-90 is slower because it has a greater rotor diameter. It is of note that pre-analysis of the Ghareb site showed that ω_{base} for G-90 should be 2.08 rad/s (i.e. the highlighted value in Table 5.1). However, this value already exceeds the maximum allowed speed of G-90; hence, ω_{base} is adjusted to the WT speed ceiling and becomes 1.99 rad/s. In addition, the higher WS_{avg} in Ghareb enables the WTs able to run at a high ω_{base} without dissipating energy. However, values of WS_B are less in comparison with values at the Nabq site, because the high rotational speed enables the WT to reach P_B at a slower WS. For a further explanation, the performance curves of GE-77 in the considered locations using the partial de-loading algorithm are shown in Figure 5.2. The breakpoint of the curve at Nabq is seen at 12 m/s, because beyond this WS, the ω can increase above its base value without decreasing PWT_m and PWT_m actually increases. Conversely, this breakpoint occurs at a slower WS at Ghareb (10 m/s), due to the higher ω_{base}.

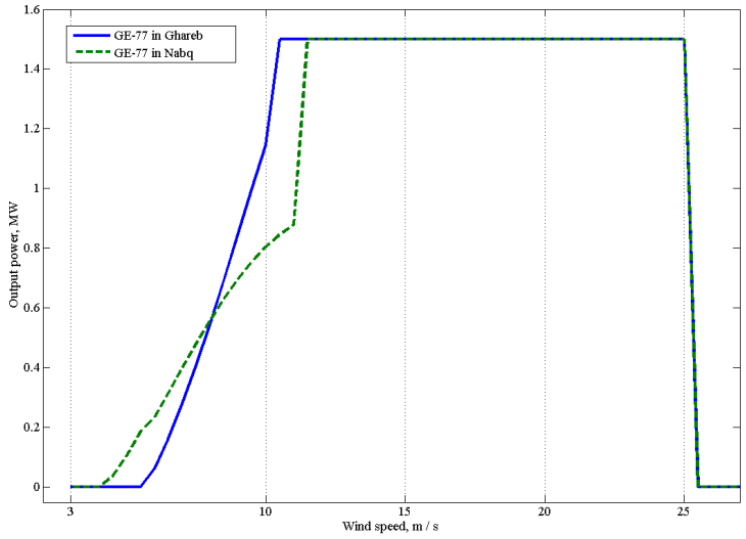

Figure 5.2 Partial de-loading performance curves for GE-77 at both sites

Table 5.1 Proposed algorithm parameters in two locations

Location	Nabq		Ghareb	
WT type	GE-77	G-90	GE-77	G-90
Parameter				
Base rotational speed, rad/s	1.45	1.54	1.96	1.99 (2.08)
WS_B, m/s and base power (P_B)	10 (0.63 pu)	9.5 (0.63 pu)	9 (0.66 pu)	9 (0.65 pu)
WS_{low}, m/s	5.6	5.3	5.04	5.04

A comparison of the use of a partial de-loading technique between GE-77 and G-90 in Ghareb is depicted in Figure 5.3. Both WTs reach their rated output at almost the same WS, although their default WS_R deviates by 3 m/s. For extended clarification, Figure 5.4 displays all the G-90 power curves implied in this chapter. Firstly, the manufacturer power curve is compared to the obtained MPT 2 curve. The two curves are almost typical, except for the dissimilarity at WSs just before the WT reaches its rated output. In fact, according to the MPT 2 curve, PWT_m is higher through this WS range. Likewise, a minor discrimination occurs at relatively low WSs just beyond WS_{CO}. The interpretations of these deviations depend on the recording methods applied to determine WT power curve by the manufacturer. It is clear that the precise values of aerodynamic model constants have a considerable impact on the MPT 2 curve.

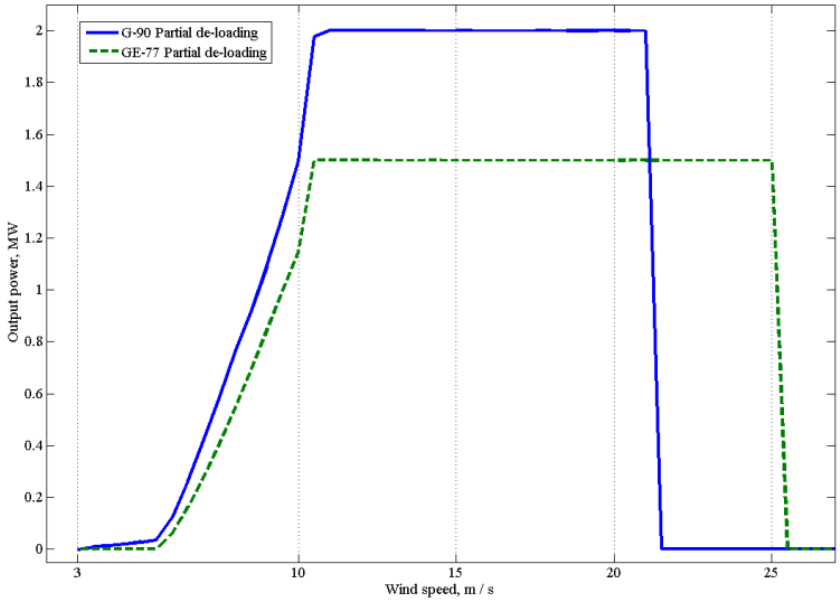

Figure 5.3 Partial de-loading performance curves for both types at Ras Ghareb site

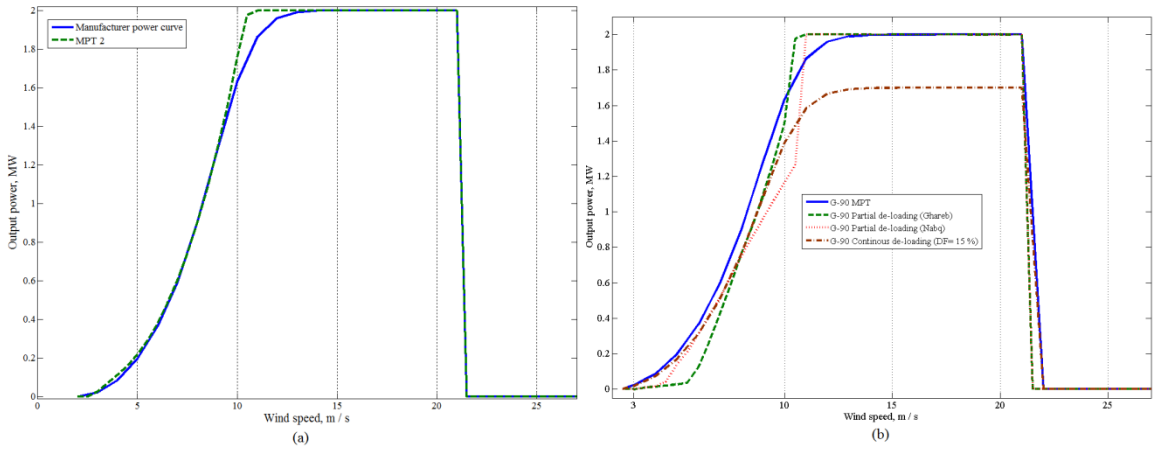

Figure 5.4 Performance curves for G-90 in all conditions and at all sites

Secondly, the breakpoint of the Nabq curve lags behind that of Ghareb. This is related to the low WS_{avg} at Nabq, and hence, $\dot{\Omega}_{base}$ is slower. In turn, the WT speed exceeds its $\dot{\Omega}_{base}$ without reducing its output at a higher WS. Thirdly, at very low WSs, the Nabq curve yields a higher output compared

to that of Ghareb, but this situation is reversed at medium WSs. As an illustration, the de-loaded operation parameters are adapted for lower WS_{avg} in Nabq. Finally, MPT and the continuous de-loaded curves are typical in attitude. However, MPT is only reduced by D_F factor to produce the power curve of continuous de-loaded operation (e.g. rated output is de-loaded to 1.7 MW).

5.5.2. Wasted energy analysis

The generated electrical energy over one year (i.e. according to available WS arrays in each location) from one WT in all cases is gathered in Table 5.2. The results show that the MPT 2 curve reveals better operational points for a WT, which is why E_{MPT2} is higher than E_{MPT1} in all cases. Nevertheless, the deviations between the two values fluctuate according to the WT type and WS nature in the considered locations. In particular, Ghareb has better WS conditions compared to Nabq, hence the impact of the difference between MPT2 and the standard power curve increases (i.e., in Nabq E_{MPT2} is higher by 270 MWh compared to 380 MWh in Ghareb). Although the rating of G-90 is more than GE-77, the difference between E_{MPT2} and E_{MPT1} in Ghareb is higher in favour of the GE-77, by 200 MWh. This could be justified by the accuracy and the nature of aerodynamic models of both WT types.

Implementation of the over-speeding technique causes less energy to be wasted, (refer to Table 5.2 and Figure 5.5). This merit is achieved by the over-speeding technique because 1) it reduces PWT_m by a small margin; and 2) it has a limited activation range compared to the continuous de-loading technique (i.e., over-speeding is valid only for $WS_{CI} < WS < WS_R$). However, the provided active power support from this algorithm is less compared to that of the other two methods, and it depends completely on the amount of extracted KE.

Additionally, this algorithm must decelerate the rotor speed during frequency deviations clearance, which increases the rate of usage of the electronic converters and the risk of loss of synchronism. Moreover, the rotor speed needs to recover its default value after the support period, thus PWT_m is reduced to allow rotor speed acceleration until it again reaches the height of the tip speed ratio. However, E_{PD} is more than E_D in all cases. At the Ghareb site (with GE-77 installed), the partial de-loading technique wasted only 7.5% with respect to E_{MPT2}, compared to 21% wasted by the continuous de-loading method. However, the advantage of partial de-loading is reduced in Nabq, as continuous de-loading wasted 21.9% while partial de-loading wasted 21.4%. This might be seen as trivial, but if the price of kWh based on Egyptian tariffs is acknowledged, it means that a single WT wastes about 2390 € annually when it is continuously de-loaded (0.5% x 4.78 GWh x 0.1 €/kWh). This value is enormous if multiplied by the number of WTs in each WF.

Table 5.2 Amounts of annual generated energy (GWh) for each operational algorithm

Location	Ghareb					Nabq				
Annual energy production, GWh / WT type	E_{MPT1}	E_{MPT2}	E_{PD}	E_D	E_{OS}	E_{MPT1}	E_{MPT2}	E_{PD}	E_D	E_{OS}
GE-77	8.63	9.21	8.5	7.34	9	4.78	5.21	4.09	4.07	5
G-90	11.77	12.15	11.35	10	12	6.63	6.9	5.78	5.63	6.9

The results of G-90 emphasise the great losses that occur due to continuous de-loading, as the rating of the WT is greater and hence more energy is wasted (remember that D_F is a percentage from PWT_m not a fixed power amount). For example, in the lower WS site (Nabq) partial de-loading wastes 16%, that corresponds to 18.4% when continuous de-loading is applied. In brief, installing greater WT ratings in sites characterized by a high average WS, amplifies the amount of wasted energy by using both de-loading techniques. Nevertheless, the partial de-loading technique has merits and mitigates the wasted energy.

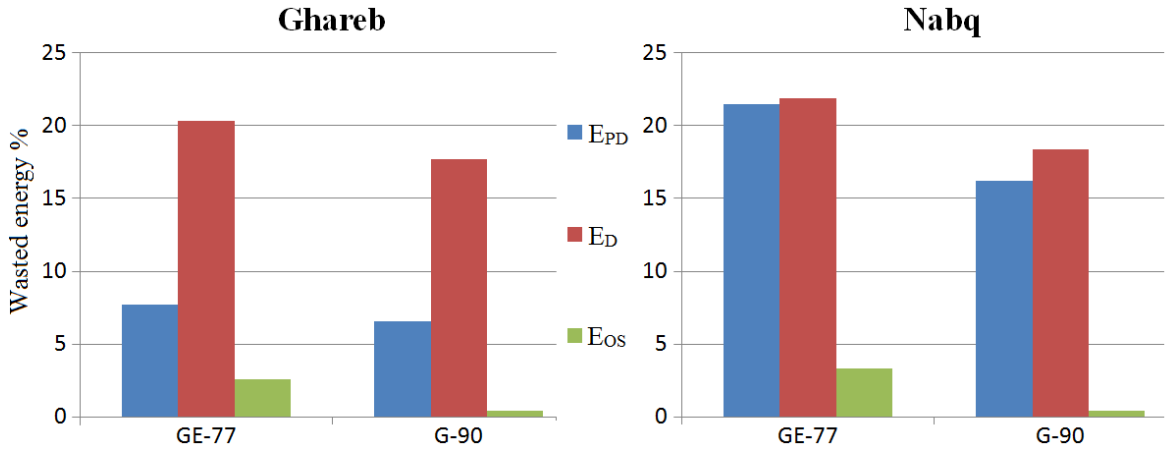

Figure 5.5 Ratios of wasted energy using all support algorithms compared to MPT2

5.6. Summary

In power systems, the supportive response of WTs during system frequency drops is mandatory at high levels of wind energy contribution. Additionally, the replacement of conventional power plants with WFs applies strict requirements from WFs during frequency events. In light of these facts, this chapter compares two support methods offered earlier in the previous two chapters. However, both algorithms have advantages and disadvantages. When considering the de-loading operation, a certain amount of wind energy is wasted in the normal mode. However, decelerating the WT increases the risk of loss of synchronism in addition to disturbing the recovery period required by the WT to return to its default operation. This chapter also investigated two different methods for acquiring the MPT curve, and analysed the differences between the two methods. Results show the considerable differences between the two derived MPT curves and their effect on harvested energy estimation. In addition, partial de-loading proved to have advantages as it mitigates wasted energy and fluctuations in WT rotational speed.

6. Wind farm energy production assessment – an Egyptian case study[3]

This chapter investigates a critical problem in relation to the estimation of the average expected wind energy production and penetration level in a given power system. This issue has a deep influence on system frequency response and the expected performance during frequency excursions. This chapter therefore presents an innovative method, based on the algorithm discussed in the Chapter 4 of evaluating the amount of conventional generation that could be replaced by certain WFs. This evaluation depends on the WS prospects in each WF location as well as the implied operation algorithm in the integrated WTs. Additionally, the types and specifications of installed WTs in each WF have a considerable impact on such analysis, hence all details need to be considered to ensure better accuracy of the obtained results. The practical application of the proposed method of assessment is then conducted on the Egyptian case.

6.1. Replacement of conventional generation by WFs

The considered replacement of conventional units is directly related to the forecasted annual energy production of the WF. Some literature assume that a WF should be able to generate an annual average value of 40% from its aggregated rated power capacity due to the intermittent nature of WS, and this has already been applied in the two previous chapters [80, 90]. However, a simplified innovative method to estimate the actual WFs capacities is also proposed, although the lack of geographical data concerning the area of suitable land at each proposed WF site forced the author to apply two certain assumptions. Firstly, all WFs have the same number of WTs; 100 WTs. Secondly, the shadowing and tower effects on WS propagation through the WF is interpreted by an overall reduction of 10% of the WF's overall annual produced energy, and this de-rating ratio is inspired from the results obtained in [87].

Three modern types of WTs of various sizes and ratings: Enercon 101–3.05 MW, Nordex 117–2.4 MW, and Gameza 90–2 MW, are integrated in this chapter. The main technical data related to each are summarized in Table A.1 in the Appendix [21, 94, 95]. The integration of several types of WTs emphasises the influence of the proposed method on the current state of wind energy expansion. Although, it is essential to apply relatively accurate models for the considered WTs, it is difficult to gain access to the technical specifications of manufacturer's models of integrated WTs. Hence the author coefficients values found in [18] are implemented. These generic models have the same structure of the accredited generic model of GE-77 embedded in the Simulink power system library. However, the constant values alter according to the considered WT type, and these values are found in Appendix 11.2. The outcomes of the energy production assessment procedure are utilized to match

[3] The major content of this chapter is published in IEEE 4th International conference on power engineering and energy as indicated in Related publications list

both the WT types and the location of the WFs, keeping in mind a homogeneous distribution of the presence of three types of WTs among the considered locations.

6.1.1. Annual energy production assessment

The annual available energy produced by each WF, founded on WS records in a WF location, is the concept used for the presented assessment procedure. For instance, the annual energy produced by each WT at each site is calculated in relation to the assigned operation algorithm that was offered in Chapter 4. It is of note that this assessment procedure assumes no wind energy rejection (i.e. all the available wind power is fed to the intended grid).

According to Method 2, three critical values are evaluated at each site for each WT type: WS_{low}, WS_{rated} and WS_b. For simplicity, WS_{CI} is assumed to be similar for all WT types and equals 4 m/s. These three major values are calculated as explained in Subsection 4.1.1. It is important to mention that de-loading techniques are suspended in this chapter to prevent any energy losses caused by de-loading. Thus, the highest wind energy production is estimated. Early trials to simulate the output power of each WT model at each location during the whole year in seconds (31,536,000s) required tremendous computational efforts and storage capacity, in addition to the extremely long execution time involved. Therefore, a minor approximation is applied to evaluate the expected annual wind energy production using reduced computational efforts. However, this algorithm retains an acceptable level of accuracy and does not ignore the produced energy within WT transients during WS transitions.

Firstly, the WS records need refining, and the time span between each two successive readings is identified (t_{WS}) in seconds so that each WF location has its own array(s) of WS records. Sometimes, a single WF has more than one WS array because the WS is inspected in different regions across the WF area. Thus, the presented procedure is repeated in each region, taking into consideration the possible (or the intended) number of WTs that should be installed in the region. t_{WS} is divided into two intervals: the first 25 s within which WT transients occurs due to the WS shifting to a new value (the integral part of equation 6.1) and the second is ($t_{WS} – 25$), where PWT_m is assumed to be constant (transients stabilize) and equals the last value reached in the first interval (i.e. PWT_m (WS_i, 25) where i = 1 to 52560). The instantaneous PWT_m array is obtained using the Simulink WT model operated by Method 2, using the continuous time domain simulation. In other words, the energy generated at a certain WS reading number 'i' starting at time = t_i and continuing for $t = t_i + t_{WS}$, is obtained using (6.1). This equation also emphasises how the output power array is obtained. This process is repeated ($31536000/t_{WS}$) times to obtain the overall generated annual energy by a given WT type in a certain WF location.

$$\textit{Energy within } t_{WS} \textit{ at } WS_i = \int_{t_i}^{t_i+25} PWT_m(WS_i, t)\, dt + PWT_m(WS_i, 25)\cdot(t_{WS} - 25) \tag{6.1}$$

The produced output power arrays are integrated with the chronological method offered in [96] accompanied by major modifications, so that the new conventional power capacity is obtained in MW (CC_{new}). One of the major modifications is the criterion used to select appropriate load data. As an illustration, it is hard to analyse the whole annual load; therefore, the load chronological values are arranged in descending order so that peak load points are on top. Thereupon, only the first 10% of the load array points are considered. These load array points are synchronized with the corresponding output power arrays to investigate the WFs power generation during the occurrence of each load level. In addition, it is preferable to make the time resolution of the integrated load array lower than the resolution of the WSs arrays, and this will be greater-clarified in the considered case study. Additionally, it is evident that events characterized by load demand that is less than the wind power generated, are excluded, although this is nearly impossible to achieve when peak load points are imposed in the offered algorithm. Finally, an average value for the conventional generation contribution values at the considered load demand points is estimated; hence, CC_{new} is evaluated using (6.2). For instance, N_L is the number of considered load points, K is the number of WSs events that exist during the implied load level number (i). N_p is the number of points in the output power array corresponding to the WS record number (k), X is the number of connected WFs, and N_{WT} is the number of WTs in the WF number (x). The losses in the generated wind power due to shadowing and tower effects on WS propagation through the WF are interpreted by increasing CC_{new} actual value by 10% as depicted in (6.2).

$$CC_{new} = \frac{\sum_{i=1}^{N_L}\sum_{k=1(i)}^{K(i)}\sum_{n=1}^{N_p}\left(Load_i - \sum_{x=1}^{X} PWT_m(k,n)\cdot N_{WT}{}^{x}\right)}{\text{Total no. of points} = N_L \cdot K \cdot N_p}\cdot 1.1 \tag{6.2}$$

6.1.2. Matching wind turbines with wind farms locations

Selecting the appropriate WT type from the three considered types mentioned earlier is intimately related to the estimated annual energy produced by each type at each WF location. In addition, the annual energy is divided into four sections based on the season so that the first three months represent winter, the next three months are spring, and so on. This classification should give a broader view of the WSs and the corresponding harvested energy with respect to the integrated WT type. Focus is also on the implemented pitch controllers, so that two models of pitch controllers are implemented in this chapter; the first one considers only the output power deviation signal as an input [26], and the other considers deviations of both the output power and the rotational speed from their reference values [27]. Further details of this topic have already been discussed in Subsection 2.2. The seasonal or annual energy efficiency for each WT type in each WF location is calculated using (6.3), where 8760

is the number of hours per year. The estimated generated energy is compared to the obtained annual energy if the WT operates at its rated power constantly. In addition, homogeneity between the presences of the three WT types is maintained to examine the influence of integrating several types of WTs in the same grid.

$$\eta_{\text{energy}} = \frac{\text{WT total annual output energy (in MWhr)}}{\text{WT}_{\text{rated power}} \cdot 8760} \tag{6.3}$$

6.2. Egypt - grid and wind energy prospects

6.2.1. Egyptian grid

Steam and gas power plants represent 86% of the Egyptian grid generation capacity, which is 19.72 GW at 50 Hz nominal frequency [97]. The approximate number of steam and gas units is 133 with ratings ranging from 25 up to 341.25 MW. Thermal plants are constructed on the circumference of rural areas with a high population density. Hydro energy covers the remaining 14% from two dams, the famous High dam and the Aswan dam. The currently installed contribution from WTs is almost neglected with respect to the system capacity. Further basic specifications for certain conventional power plants are summarized in Table 6.1. Similar to the benchmark system of the previous chapters, typical values for governor and turbine model parameters are implemented to enhance the accuracy of the results. The annual hours count for different demand levels are depicted in Figure 6.1.

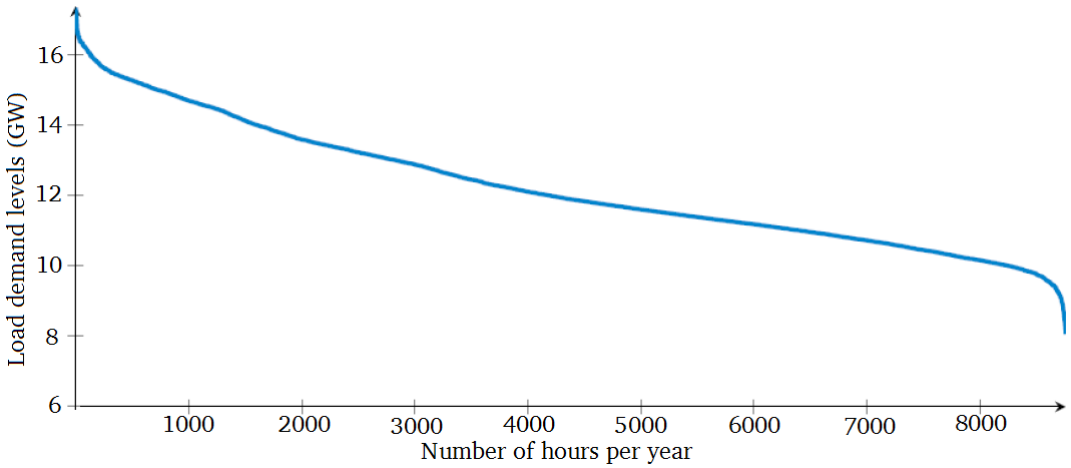

Figure 6.1 Number of hours within which different load levels occur per year

6.2.2. Promising locations for wind farms

Egypt has wide variety of renewable energy resources (e.g. solar, hydro and wind), and this chapter considers wind energy prospects in the Egyptian grid. Specifically, thirteen sites dispersed in Egyptian terrain are considered, as shown in Figure 6.2 [98]. Implemented WS data are obtained from in-site measurements, which yielded average chronological WS records in ten minutes steps (i.e., 52560 readings/year) at a 3% standard deviation. The annual average WS in these sites varies between 7.5 to

10 m/s, where the highest averages are recorded in Gulf of Suez area and the lowest (5.5 to 6.5 m/s) are found along the northwest coast. The ratios of corruption of available data range from 0.4% up to 34% of the total number of readings in each location, and the corrupted slots are replaced with an equivalent number of slots from the previous or latter records (e.g. if there are 500 corrupted points in a certain WS array they are replaced by the 500 previous points). The general specifications of WS data at the considered sites are depicted in the Appendix Tables.

6.3. Implementation of proposed algorithm

Firstly, the operational parameters of Method 2 (offered Chapter 4) are tuned to each WT in the considered locations. The evaluation of these parameters is based on the WT model and WS_{avg} at each site. A sample of the numerical values of these parameters is summarized in Table 6.2, and the values of all the concerned WFs are found in the Appendix Tables. As expected, $Ɠ_b$ is relatively higher in locations characterized by high WS_{avg} (e.g. Ras Ghareb), but in some cases it possibly violates its maximum limit to fulfil the conditions of the proposed algorithm.

Table 6.1 Samples for the types of conventional plants in Egyptian grid

Power Plant	High Dam	Koraymat	West Cairo
Type	Hydro	Steam	Gas
No. of units	12	2	3
Total Capacity, GW	2.1	1.25	0.33

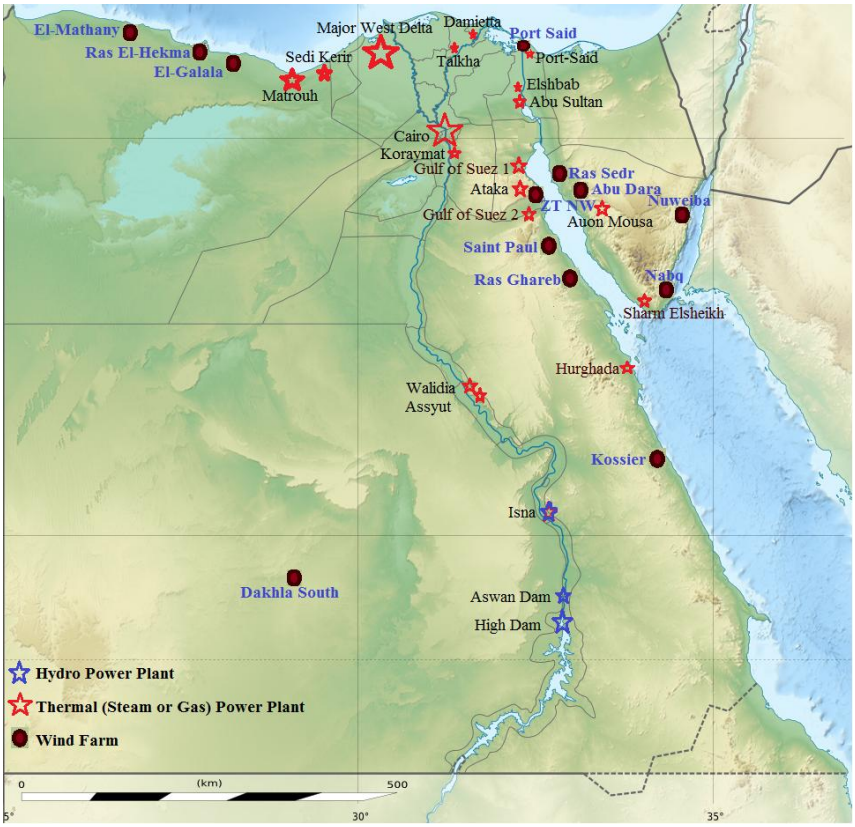

Figure 6.2 Map of Egypt showing recommended WFs and conventional plants

Therefore, ω_b is adjusted to its maximum value; the highlighted values represent the examples of such cases. This problem appears only with N-117 and E-101, as they have a lower maximum limit for ω_b in comparison with G-90.

The second step is to generate the output power arrays for the three WTs in all locations, as explained earlier. The instantaneous output power of some WTs in some locations, and the corresponding WSs, are displayed in Figure 6.3. The energy efficiency of each WT type in each location is then evaluated, as explained in Subsection 6.1.2. A sample of the obtained results is presented in Table 6.3 and Figure 6.4, and the complete results are included in the Appendix Tables. According to these outcomes, N-117 has the best record at all sites due to its aerodynamics characteristics, which serve to obtain a higher output power at lower WSs. In light of the evaluated η_{energy}, WT types are matched with WF locations. However, the same type of WT is not integrated in more than five locations to guarantee a homogeneous mix between WT types and locations. The final allocation of WT types is found in Table 6.4.

The next step is to calculate CC_{new} in relation to the Egyptian grid annual load and available WFs output power arrays. The available Egyptian grid annual load is in the form of 1 h steps, and the WS records are in 10 min steps. Thus, the WS has six different values during each load step. However, the annual load array points are arranged in descending order, and only 10% are included in CC_{new} evaluation.

Table 6.2 ω_b, WS_{base} and WS_{rated} at certain WF sites

WT Location (WS_{avg})	El-Mathany (5.75)			Ras Elhekma (6.52)		
WT model	E-101	G-90	N-117	E-101	G-90	N-117
ω_b (rad./s)	0.9	1.3	1.0	1.0	1.5	1.1
WS_{rated} (m/s)	16.9	15.8	9.6	14.6	12.4	10.1
WS_{base} (m/s)	15.0	14.0	8.5	13.0	11.0	9.0

WT Location(WS_{avg})	Ras Ghareb (9.77)			Saint Paul (8.25)		
WT model	E-101	G-90	N117	E-101	G-90	N-117
ω_b (rad./s)	1.5	1.7	1.4	1.3	1.6	1.4
WS_{rated} (m/s)	11.0	11.3	9.6	11.3	11.8	9.6
WS_{base} (m/s)	9.8	10.0	8.5	10.0	10.5	8.5

The Egyptian grid load levels and their corresponding durations of occurrence are depicted in Figure 6.1. For instance, each WF is aggregated as one single WT, so that the WT output array is multiplied by the number of WTs inside the WF (i.e., 100 WTs in this study). The power arrays of WFs are synchronized with the time span at which the load point (*i*) occurs.

For example, the maximum load point (i.e., 17.3 GW) occurring at hour number 7663 is equivalent to the WS readings starting from record number 45978 (7663·6) to 45983 (7663·6 + 5). Thus, each load time span includes 6 different WSs (k=1 to 6). The value of parameters used in (6.2) are K = 6, N_L =

876 and N_P = 600. Integrating the above-mentioned givens by substituting in (6.2) yields CC_{new}=15.75 GW, such that 13 WFs composed of 1300 WTs have replaced 20% of the conventional capacity. Nevertheless, as this value is estimated according to peak load points, it is perhaps a generous solution. Values of CC_{new} will therefore be more accurate when the average load points are implied but with slight increase in risk.

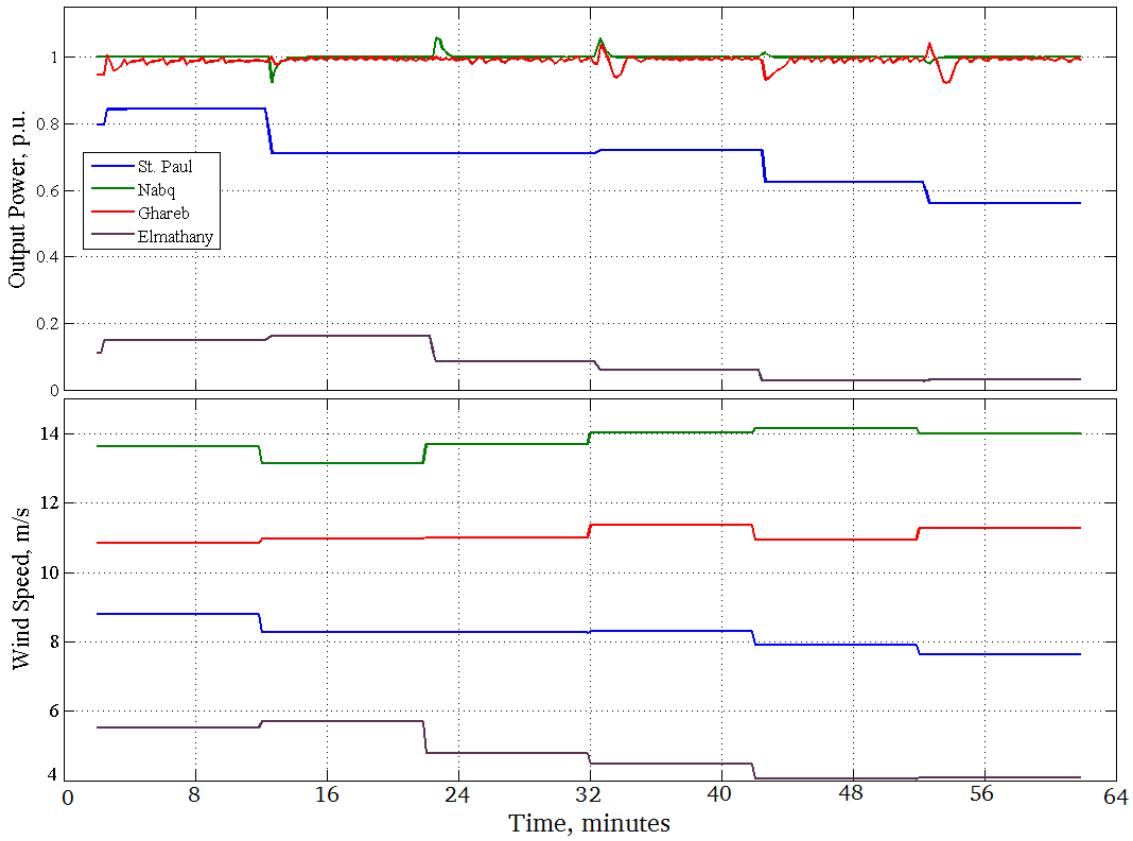

Figure 6.3 WSs and WTs outputs in four locations during peak load hour

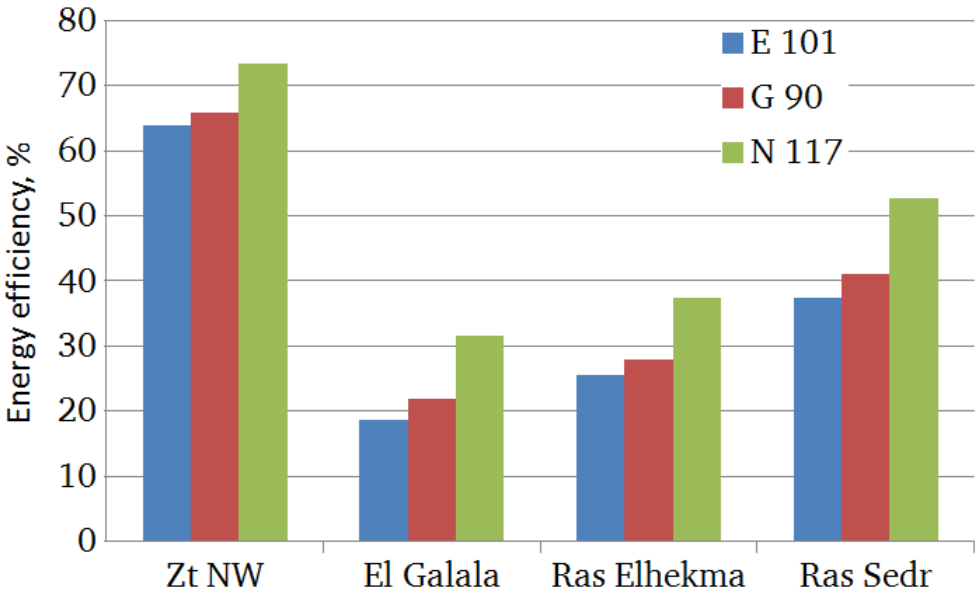

Figure 6.4 Annual energy generation efficiency in 4 locations

Table 6.3 Seasonal energy in GWh and η_{energy} in % in certain locations

Location		ZT NW (10 m/s)			El-Galala (6 m/s)			Ras Sedr (7.4 m/s)		
Season/WT		E-101	G-90	N-117	E-101	G-90	N-117	E-101	G-90	N-117
Winter	Energy	5.8	3.9	4.9	1.1	0.8	1.4	3.5	2.5	3.8
	η_{energy}	87.3	88.1	94.0	15.9	18.2	27.1	53.1	57.9	71.4
Spring	Energy	4.6	3.1	4.1	1.1	0.8	1422.3	2.6	1.9	2.9
	η_{energy}	68.7	71.0	78.2	15.9	18.6	27.1	39.3	43.3	55.1
Summer	Energy	2.3	1.7	2.5	1.6	1.3	2152.7	1.2	0.9	1.6
	η_{energy}	34.1	37.8	47.7	24.5	28.8	41.0	17.6	20.3	30.3
Fall	Energy	4.4	2.9	3.9	1.3	0.9	1.6	2.6	1.9	2.8
	η_{energy}	65.4	66.8	73.4	18.7	21.4	30.9	39.4	42.8	53.5

Table 6.4 Final matching of WTs to 13 considered wind farms sites

Location	WT type
Abu Dara	E-101
Dakhla	E-101
El-Galala	N-117
El-Mathany	G-90
Kossier	N-117
Nabq	E-101
NW ZT	E-101

Location	WT type
Nweiba	N-117
Port Said	G-90
Ras El-Hekma	G-90
Ras Ghareb	G-90
Ras Sedr	N-117
St. Paul	N-117

6.4. Frequency response during normal operation

6.4.1. Test system description

The system frequency response is examined before and after wind energy penetration through a continuous time domain simulation. To achieve this target, the construction of a test system is required that represents the main features of the Egyptian grid that have a direct impact on the frequency response. According to [10, 52], the modelling of transmission lines and transformers is minor and does not have a deep impact on frequency stability studies. Therefore, the implemented test system highlights in detail the conventional generators and connected WFs. The model includes complete models of hydro-, steam, and gas generators, as well as their governors. The models of the governors are similar to those used earlier in Chapters 3 and 4. For simplicity, it is assumed that each conventional generation technology is presented by one aggregated power plant that has a contribution of CC_{new}, which is proportional to its real ratio in the Egyptian grid. For example, hydro generation participates 14%, hence the hydro generator capacity before wind integration is 2.76 GW (i.e., 14%·19.7 = 2.76 GW) and after the connection of WFs is 2.2 GW. Similarly, the thermal generation capacity is split into 75% steam and 25% gas power plants. Consequently, the steam generation capacity before and after the WFs are connected is 12.7 and 10.16 GW, respectively. A single line diagram of the implemented test system is shown in Figure 6.5, taking into consideration the integrated WFs described in Table 6.4, where each WF is composed of 100 WTs of the above-mentioned types. The wake and shadowing effects are ignored in this chapter. During simulation, the power references of conventional generators governors are adjusted continuously based on the WFs changing outputs as in (6.4):

$$P_{ref\ i} = (load - WFs\ output) \cdot \text{Generator Capacity}_i \quad (6.4)$$

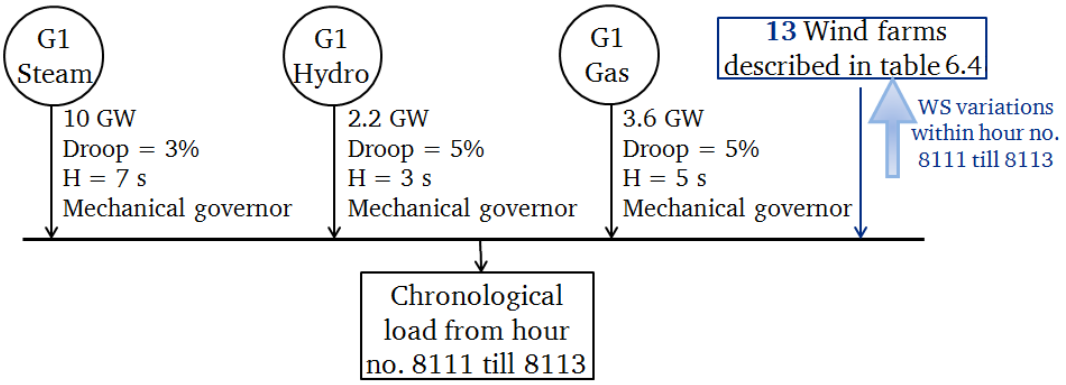

Figure 6.5 Single line diagram for the implemented test system after integration of WFs

The total simulation span is selected to include the hour of highest wind energy contribution during the selected top 10% of peak load hours. The simulation duration is then extended to start one hour earlier, at hour no. 8111 and ends one hour later, at hour no. 8114 (the simulation time span is 3 h through a 1 s step continuous dynamic simulation). The performed analysis reveals that the highest wind energy participation is 16.2% from the total load demand; 15 GW occurs at hour no. 8112.

6.4.2. Frequency response analysis

The simulations proved that frequency deviations occurring during WS variations are not severe, in the range of 30 mHz, as shown in Figure 6.6. As expected, the frequency deviation is nearly zero in between WS variations, because there are no variations in either load or generation. Consistent with the hourly load variations, a frequency excursion occurs every hour. It is a fact that WS does not change in such a synchronized manner in all WFs, but this case is considered as a worst-case scenario. Nevertheless, the obtained results give a reasonable overview of the system's performance, in spite of some virtual conditions. The worst frequency drop (i.e., 58 mHz) occurred at the instant of transition to peak load; hence, frequency response during this drop is magnified in a separate graph, as shown in Figure 6.6. In addition, steam and hydro generation curves, as well as WFs output, are displayed during this relatively high frequency excursion. Comparing before and after the WF integration, it is noted that the deviation in system frequency response is very slight, and that the overall attitude is almost similar in both cases. The major drawback is in the deeper frequency drop after wind integration, but the recovery time is nearly unchanged (i.e., 10 s). This relatively high frequency deviation returns with a sudden rise in load of 210 MW accompanied by a 200 MW decrease in the WFs generation. At the instant of the load rise, the conventional generation participation jumps by 0.03% from its rated capacity. Most of this escalation is covered by the steam plant, as it has the highest share in the conventional power capacity.

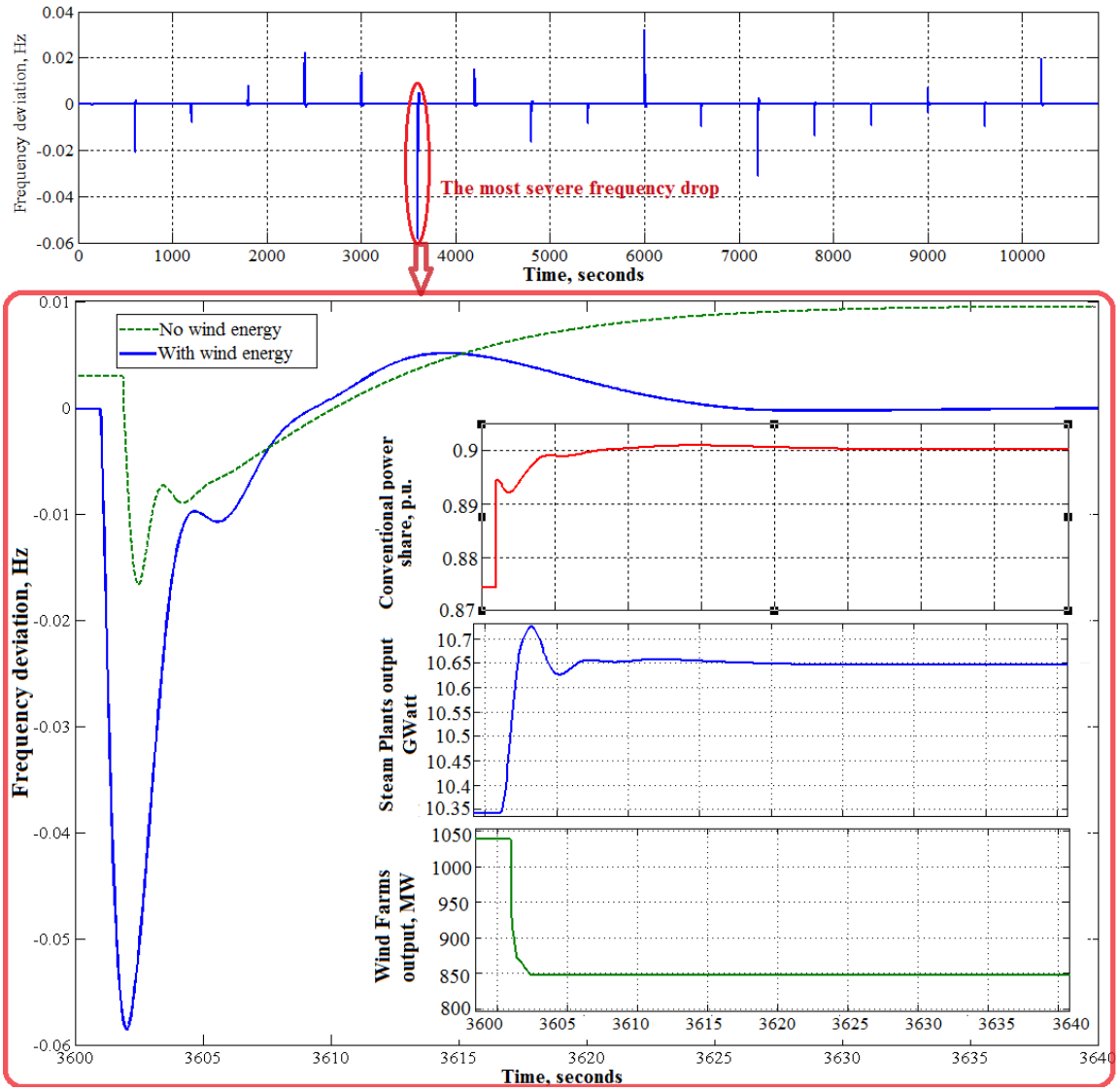

Figure 6.6 Grid frequency responses in the two case studies

Thus, conventional plants achieved an acceptable reaction to rapidly recover the system to steady state operation (i.e., t_{SM} = 35 s). In fact, the governors' parameters have a considerable impact on enhancing and accelerating the recovery process.

Results showed that all integrated WFs participated by an average of 10% from the load demand during the selected peak load hours. Most of these peak load points occurred in the last quarter of the year (i.e., autumn season) which overlaps with the low records of WSs in the majority of the selected locations. In contrast, higher wind energy participation levels are expected in summer and winter. Generally, the suggested WFs installations caused a beneficial reduction in conventional capacity by 20%. In addition, the amount of fuel used throughout the whole year, and the operational hours of the installed conventional stations, would be mitigated during periods of high WSs. Thus, failure probabilities, running costs, and pollution rates would be noticeably mitigated. The dependence of conventional generation power control on the supplied wind power proved to be valid, but it caused moderate and low fluctuations in generated power.

Consequently, events of mismatch between generation and demand were produced, leading to major and minor frequency excursions. Therefore, a dead-band for variations in reference power signals needs to be installed, and hence the fine frequency deviations are ignored. The same frequency analysis procedure is repeated at the lowest load hour (8.05 GW) and one hour before and after (i.e., hours: 2316 to 2318). The severest frequency deviation occurred at 3600 s in the form of an overshoot with a peak value of 0.43 Hz. It was caused by the sudden drop in load by 1.4 GW (7.76 GW to 6.34 GW) and a minor rise in the overall production of the WFs by 70 MW. At this instant, conventional power participation was about 49%, and it dropped to 41% and t_{SM} is 30 s after very limited oscillatory behaviour.

6.5. Summary

This chapter evaluates the possible wind energy integrated capacity in the Egyptian grid and its impact on frequency response during critical events of load variations. A detailed algorithm is implemented to estimate the expected wind energy annual energy production and the corresponding replaced conventional capacity. According to this algorithm, annual energy productions of each WT type in thirteen different locations are evaluated. The new conventional generation expected capacity is then calculated through a genuine procedure. Complete real data and models for conventional turbines and their governors, as well as WSs records, are included in the implied compact grid simulator. Results reveal an accepted system performance after the wind energy medium penetration level. This delivers valid suggestions for wind energy development in the Egyptian grid based on a solid grounding of detailed modern analysis.

7. Wind farms dispatching during frequency drops[4]

This chapter focuses on dispatching WTs inside each WF during the mitigation of frequency drops. The proposed algorithm integrates several factors to determine the number of WTs that are required to contribute to system frequency recovery. The WS nature in the WF location, the installed WT types, and their numbers are used as examples. However, the dispatching process is instantaneous, and it therefore relies on other dynamic factors (e.g. the average WS at the WT and the frequency deviation severity). In addition, conventional generation is controlled based on WFs reactions during frequency drops, also during normal operation. A chosen zone from the Egyptian grid is integrated as a benchmark for applying the offered algorithm, and real data of WS records and the specifications of generation plants are applied.

7.1. Proposed algorithm

In principle, this algorithm describes a simplified and efficient method for controlling the switching process of WTs between normal and support operation modes according to the estimated participation of each WF. This algorithm could be applied on all installed WFs in a grid regardless of support algorithms integrated in WTs; in addition, every WF could have a different frequency support technique installed in its WTs. The dispatching algorithm offered depends on dividing every WF into a defined number of clusters (Ni_c). These clusters can be classified according to several parameters, such as WS, WTs rating (i.e., when the installed WTs inside the same WF are not typical), and other parameters; nevertheless the classification method has a minor impact on the adequacy of the proposed algorithm. For instance, this chapter classifies clusters according to WS variations inside the WF, and this classification acknowledges changes in WS magnitudes due to the shadowing and wake effects related to the towers. For simplicity, it is assumed that WTs are arranged in regular rows and columns inside the WF. The first row is subjected to the initial free stream WS; thereafter the WS is reduced gradually in each row according to the shadowing and wake effects of the towers. The average wake WS is evaluated at each row as previously explained in Subsection 3.3.2. It should be mentioned that the main target in integrating WS wake effects is to examine the idea of WF clustering based on incident WS on each row of WTs.

The number of WTs in each row is related to the number of WTs inside the WF, so that the total number of WTs is the product of numbers of the rows and columns; consequently, the number of clusters equals the number of rows. For simplicity, and to focus on examining the proposed algorithm's leverage, the number of installed WTs is typical in all WFs (100 WTs), so that each WF has 5 clusters and 20 WTs/cluster; thus each cluster is aggregated as one WT with a rating that is 20 times that of a single WT. In brief, the main target of the algorithm is to convert the required active

[4] The major content of this chapter is published in Elsevier International journal of electrical power and energy systems as indicated in Related publications list

power to recover the system frequency to a given number of clusters/WF participating in the recovery process, by switching the WTs included in these clusters to support operation. The following subsections explain the three stages of the proposed algorithm in detail, and discuss all related equations and assumptions.

7.1.1. Estimation of required overall active power support from installed WFs

WFs participation in the mitigation of frequency dips is emphasized by the certain rise in supplied active power as soon as the event starts. This power surge is guided by several conditions and it should have a maximum defined limit, either for all the connected WFs or for each WF independently. This participation is converted to per unit, so that it is easier to understand the role of each WF in frequency support, and also to facilitate implementation of the proposed dispatching algorithm.

The first stage evaluates the required step rise in active power from all the connected WFs ($\Delta P_{WFs\ total}$), using (7.1) to contribute to eliminating the stirring frequency deviation (where 'm' is the number of integrated WFs). Generally, this power step is limited so that it has certain predetermined threshold value, which is calculated in pu.

$$\Delta P_{WFs\ total\ max} = \frac{\sum_{i=1}^{X} \Delta P_{WF\ max\text{-}i}}{\sum_{i=1}^{X} S_{WFi}} \cdot s_f \qquad (7.1)$$

The maximum stable available power step from a WF ($\Delta P_{WFi\ max}$) is estimated at a particular WS, namely WSi_{avg}, which is incident on the first row; hence, the WSs hitting the following rows are calculated using (3.8). A frequency deviation signal is implied to trigger the installed support algorithm. The rise in active power supplied from WFi ($\Delta P_{WFi\ max}$) at these specific conditions is then recorded. The previous process is repeated for each WF, so that its $\Delta P_{WFi\ max}$ is considered as a fixed predetermined factor. The constant 's_f' is an up scaling factor in the range of 10–20%. As an illustration, $\Delta P_{WFi\ max}$ is evaluated at WS_{avg}; therefore its final value is multiplied by 's_f' to compensate for any possible wasted margin in $\Delta P_{WFi\ max}$ regarding the probability of a higher WS occurrence during frequency events. S_{WFi} is the rated output of the WF number "*i*", and it equals the aggregation of the installed WTs rated powers and X is the number of integrated WFs.

Two frequency control methods known as droop and inertial controllers are integrated. These two methods are widely implemented in conventional generation plants, but they still do not have a clear integration approach with WTGs. The major input for this stage is the frequency deviation in pu with respect to the system nominal frequency, as shown in Figure 7.1. A dead band between (± 0.05 Hz) is included to avoid undesired oscillations at minor frequency drops. However, this band should not violate the constraints of the SOs stated in the grid code. The applied case studies will examine the

influence of droop and inertial controller constants (K_{Droop}, $K_{Inertia}$) on the performance of the proposed algorithm.

7.1.2. Estimating the required power step from each WF

$\Delta P_{WFs\ total}$ is distributed among the connected WFs so that the contribution of each WF (ΔP_{WFi}) is calculated through (7.3); thereafter the number of participating clusters in each WF is determined according to ΔP_{WFi}. The weight of WF number '*i*' (WFi_{weight}) is a fixed parameter estimated before running the algorithm for each WF using (7.2). In other words, WFi_{weight} value is static and independent from other dynamic factors such as the frequency deviation severity and WS. WFi_{weight} is the major parameter deciding the contribution of each WF according to the mentioned static factors and is evaluated in (7.2) through an algebraic summation for the weights of all WFs installed in the studied system. The implemented distribution process is based on static and dynamic factors, yet the only dynamic factor applied in this chapter is the instantaneous approximate free stream WS magnitude at each WF (*WSi*), so that the WSi_{inst} is directly proportional to the WF contribution to curtailment of the frequency excursion. In addition, the fixed parameters are WSi_{avg}, installed WT rating in WFi (WTi_{rating}), and its rated WS (WSi_{rated}). As an illustration, WSi_{inst} is compared to the average value of WSi_{rated} and WSi_{avg}, as depicted in (7.3). It is of note that the final amount of ΔP_{WFi} is multiplied by $S_{WFs\ total}$ to convert it to MW. Thereafter this obtained value in MW is divided by S_{WFi} to calculate ΔP_{WFi} in pu on the basis of the considered WFi.

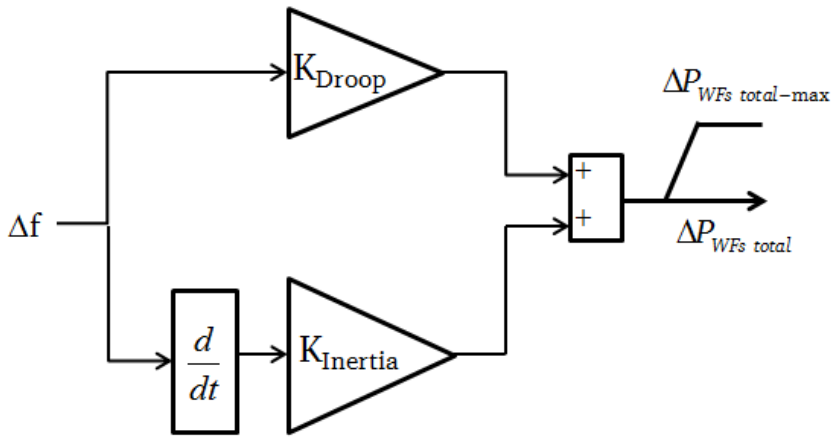

Figure 7.1 Stage 1 (Droop-Inertial) controller block diagram

$$WFi_{weight} = \frac{WSi_{avg} \cdot WT_{i\ rating}}{WSi_{rated}},\ WFs_{total\ weight} = \sum_{i=1}^{m} WFi_{\ weight} \tag{7.2}$$

$$\Delta P_{WFi\ pu} = \Delta P_{WF\ total\ pu} \cdot \left(\frac{WFi_{weight}}{WFs_{total\ weight}} \cdot \frac{WSi_{inst.}}{0.5 \cdot (WSi_{avg} + WSi_{rated})} \right) \cdot \frac{S_{WFs\ total}}{S_{WFi}} \tag{7.3}$$

7.1.3. The evaluation of the number of participating clusters in the support process

The overall contribution of a certain WF (as estimated in the previous stage) is interpreted into a certain number of WTs that are switched to a support algorithm. However, it is difficult and

impractical to control each WT singularly, thus the WF is split into a certain number of clusters (Ni_c). It is possible to base the clustering process on certain different approaches; one is wind-free stream propagation inside the WF, which is used in this research work. As an illustration, the proposed algorithm assumes a simplified relation (in particular, the number of participating clusters (Ni_{pc}) is directly proportional to the ratio between the requested power step and the maximum allowed power step as indicated by (7.4)).

$$Ni_{pc} \approx \mathrm{Ni_c} \cdot \frac{\Delta P_{WFi\ pu}}{\Delta \mathrm{P_{WFi\,max}}} \tag{7.4}$$

The obtained value for Ni_{pc} is always rounded to the lower digit, excluding values that are less than one. As an illustration, all connected WFs have to participate in the frequency deviation mitigation; thus, the minimum value, Ni_{pc}, during frequency events is 1. In addition, the value of Ni_{pc} is updated every time frame (t_f), which is assumed to be 5 s in this research work. Applying t_f avoids unexpected fluctuations and high transitioning rates between normal and support operation of WTs in the same cluster. The cluster involvement priority is decided according to the incident WS at each cluster, for instance, the first cluster facing the wind free stream has the highest priority (i.e., because WTs in this cluster are subjected to the highest WS, hence the produced power is higher compared to that of the WTs in other clusters). In general, the priority classification of clusters depends on the implemented clustering theory. In relation to the three stages of the offered dispatching algorithm, the first stage is almost identical to the conventional generation attitude during frequency drops, whereas the second and third stages are unique to WFs and are coherently dependent on the WF's layout and the WTs' specifications, as well as WS conditions and the imposed clustering technique. To facilitate the understanding of the proposed algorithm and to highlight its coherency and feasibility, Figure 7.2 provides a flowchart for all stages.

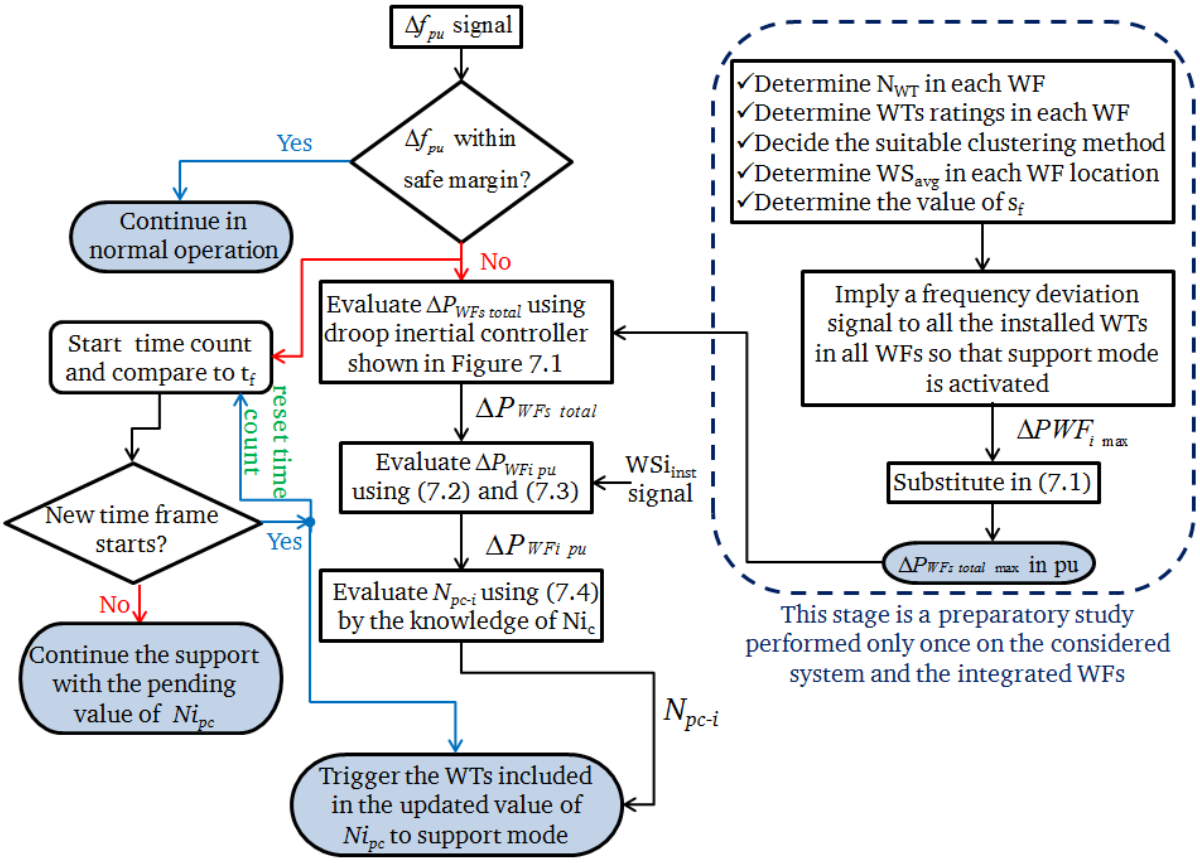

Figure 7.2 Flowchart for the proposed dispatching algorithm

7.2. Test system and case Studies

7.2.1. Test system

In this chapter, a zone from the Egyptian grid is selected as a benchmark (as clarified in Figure 7.3), and the type and capacity of each conventional plant is shown in Table 7.1. The total conventional capacity of this sector is 3825 MW, and it represents 21.25% of the total generation capacity of the Egyptian grid. As in the previous chapters, the typical values for conventional generators governors, turbines models, and parameters are implemented in the frequency response analysis. This system sector is selected due to the presence of the high number of possible WF locations, which are geographically concentrated in a relatively small area so that they can easily communicate with each other. In this chapter, it is assumed that the nine WFs are integrated, and that each WF is composed of 100 WTs of the same type, (a description of the WFs is shown in Table 7.2). According to Chapter 6, the expected wind energy penetration in the Egyptian grid is about 20%, but this percentage relies on several parameters: WFs areas; number of WTs per WF; the types of installed WTs in each WF; and the implemented operation algorithms. It is thus assumed that each WF produces on average 45% of its rated power acknowledging WS fluctuations. For example, the first WF contains 100 Enercon-101WTs, hence its overall rated power is 320 MW and the expected average output is 320·0.45 = 144 MW. Implementing this rule on the rated capacity of the installed WFs yields an average output of

1040 MW, consequently the modified (i.e., reduced) conventional capacity in the considered zone is 2785 MW.

7.2.2. Case studies

Six case studies are performed to examine the influence of the proposed algorithm main parameters settings on the integrated power system frequency response, which is obtained by the time domain simulations methods explained in [52]. The considered power system zone is modelled by two compact generation plants: steam and gas as shown in Figure 7.4. An arbitrary single load is applied with a sudden steep rise from 3262 MW to 3653 MW after 300 s. Therefore, a moderate frequency excursion will occur as a consequence of the load sudden increase, and the WFs will react to support the system during its recovery. However, the system frequency responses differ according to the parameters that control the WFs' frequency support operation, including the offered dispatching algorithm. The base case study simulates the system without any wind energy penetration; in other words 3825 MW of conventional generation. Thereafter, the conventional generation is reduced to 2785 MW in all the case studies described in Table 7.3. The frequency deviation and the power reference signals fed to the conventional generators governors are delayed by 25 s (i.e., at t = 300 s a fault occurs and the control signals actual values are delayed by 25 s, therefore conventional generation starts reacting at t = 325 s) to emphasis the role of WFs in clearance of the frequency drop.

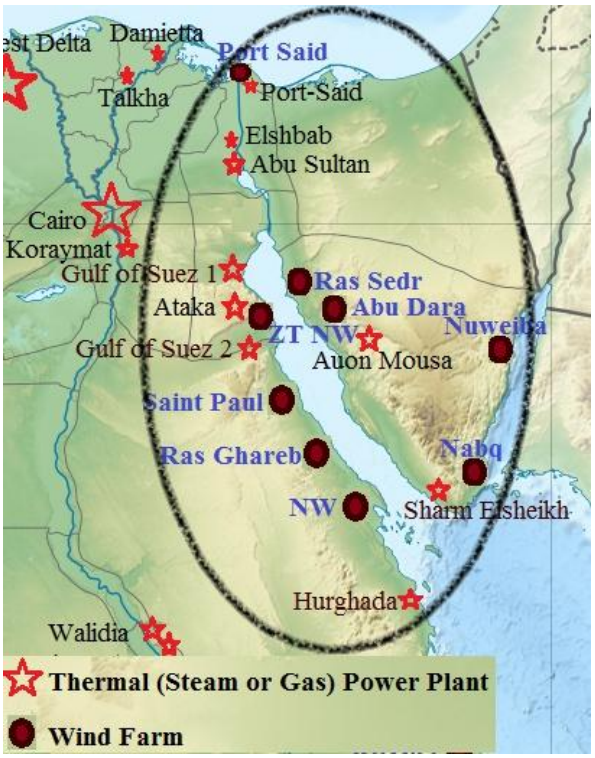

Figure 7.3 Egyptian conventional power plants and most promising locations for WFs

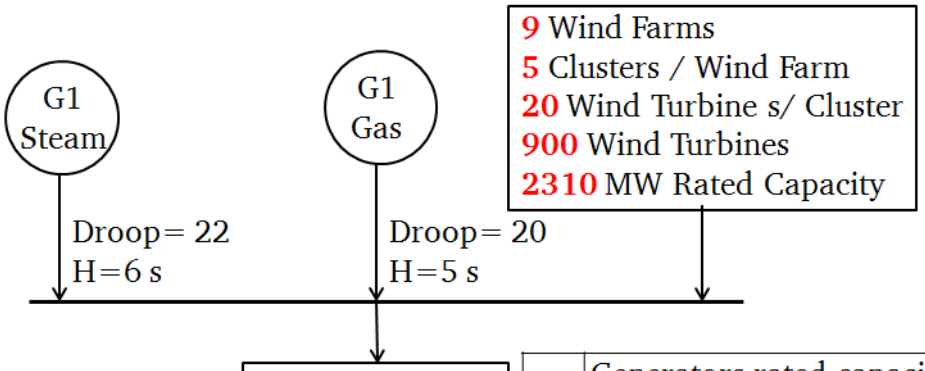

No.	Generators rated capacities	
	Before WF	After WF
G1	3480 MW	2534 MW
G2	345 MW	251 MW

Figure 7.4 Benchmark system diagram before and after connection of wind farms

Table 7.1 Conventional power plants connected in the considered zone

Plant Location	Type	Capacity, MW
Port Said	Steam	682
Abu Sultan	Steam	600
Gulf of Suez 1 and 2	Steam	682
Ataka	Steam	900
Auon Moussa	Steam	640
Sharm Elsheikh	Gas	178
Hurghada	Gas	143

Table 7.2 Specifications of installed WFs

No.	WF location	Location $WS_{avg.}$	Installed WT type
1	Abu Dara	8.2 m/s	Enercon-101 (3.2 MW)
2	Nabq	6.8 m/s	Enercon-101 (3.2 MW)
3	NW	10 m/s	Enercon-101 (3.2 MW)
4	ZayT NW	10 m/s	Gameza-90 (2 MW)
5	Ras Ghareb	9.8 m/s	Gameza-90 (2 MW)
6	Port Said	4.7 m/s	Gameza-90 (2 MW)
7	Ras Sedr	7.1 m/s	Nordex-117 (2.5 MW)
8	St. Paul	8.5 m/s	Nordex-117 (2.5 MW)
9	Nuweiba	5.5 m/s	Nordex-117 (2.5 MW)

Table 7.3 Examined case studies

Case Study	Conventional Capacity	Wind Speed	K_{droop}	$K_{inertia}$
Base Case	3825 MW	No wind energy integration	----	----
1	2785 MW	$1.2 \cdot WS_{avg.}$ in each WF	20	40
2	2785 MW	$0.8 \cdot WS_{avg.}$ in each WF	20	40
3	2785 MW	$1.2 \cdot WS_{avg.}$ in each WF	2	40
4	2785 MW	$1.2 \cdot WS_{avg.}$ in each WF	40	40
5	2785 MW	$1.2 \cdot WS_{avg.}$ in each WF	20	4
6	2785 MW	$1.2 \cdot WS_{avg.}$ in each WF	20	80

7.3. Results and discussion

7.3.1. System frequency responses

This section delivers a discussion related to the obtained system frequency response curves in the previously described case studies (Cases 1-6). This discussion is based on the examination, inspection, and comparison of three pivotal parameters: 1) the maximum frequency deviation (Δf_{max}); 2) the time at which the safe margin of ±0.05 Hz is reached (t_{SM}); and 3) the frequency deviation 10 s after the frequency event initiation (Δf_{10s}). Firstly, the system frequency responses are compared whether the control signals to the conventional plants governors are delayed or not, as in Figure 7.5. As expected in the case of delay, the frequency deviation continues for longer, thereby providing a better opportunity to study the reaction of the WFs and focus on their role during this critical period. An illustrative comparison is then made between the three parameters values concerned in the selected case studies, and this is shown in Figure 7.6.

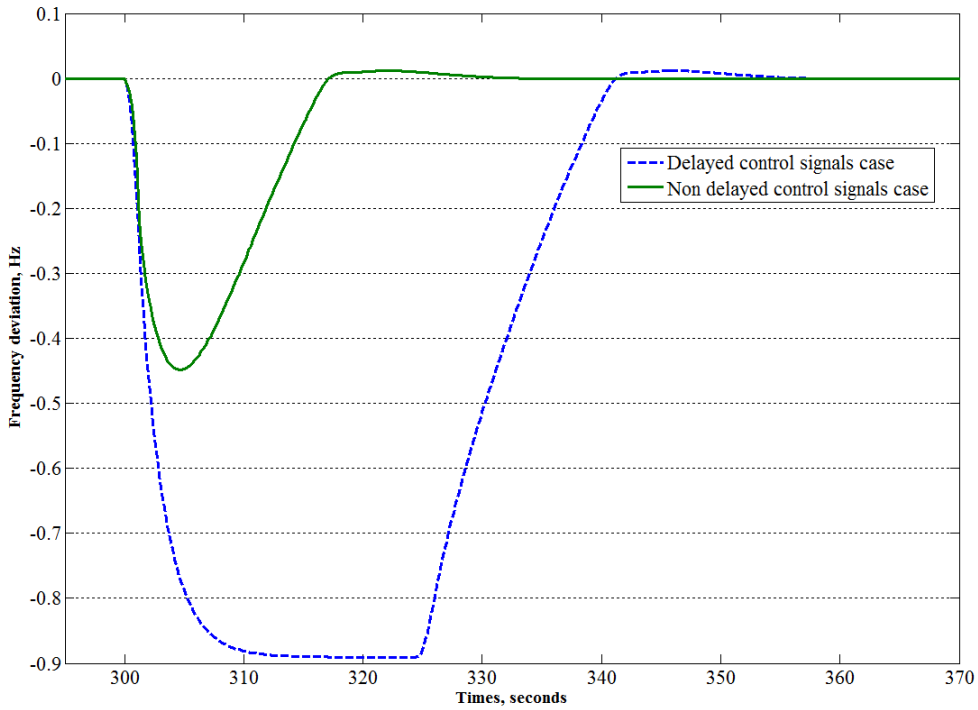

Figure 7.5 Frequency response at delayed and non-delayed control signals (No WFs)

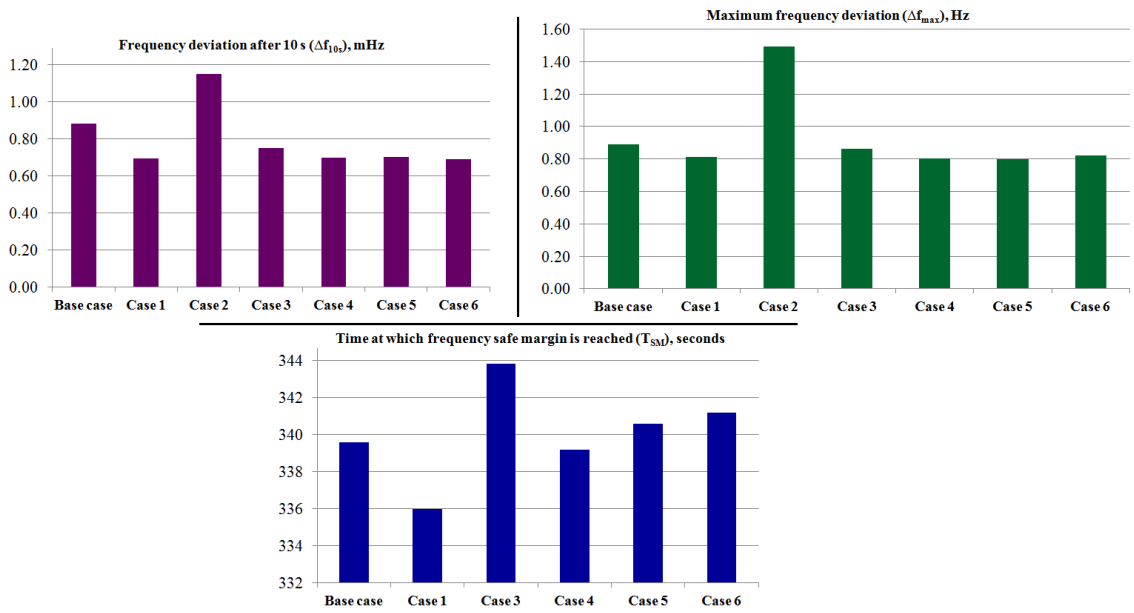

Figure 7.6 Calculated parameters of frequency responses in selected cases

However, the response of Case study 2 is omitted from Figure 7.7, as it exists in a different and inferior range of frequency deviation. Therefore, the inclusion of such a curve reduces the level of details offered by the graph, because the frequency deviation axis range is extended. The scientific reasons for this disparity in Case study 2 are clarified later in the relevant subsection. Most case studies have perceptible impacts on t_{SM}; for example, Case study 1 has the shortest t_{SM} while Case study 3 has the longest. An interpretation of this relies on the weak contribution of WFs in frequency recovery when K_{droop} is adjusted to a relatively low value. In particular, the low values of K_{droop} and $K_{inertia}$ reduces Ni_{pc} so that the surge power injected by WFs is reduced. This is also ensured by Case study 5, with the lowest value of $K_{inertia}$, namely, 4. In contrast, very high value of $K_{inertia}$ forces the WFs to dissipate their stored energy at an early stage and it then takes longer for them to recover to normal operation, hence t_{SM} is not as good, as in Case study 6. Generally, Case study 1, with average values for K_{droop} and $K_{inertia}$ accompanied with a higher WS at all sites achieved the best results for t_{SM}. The low incident WS in all locations, namely 80% from WS_{avg} of each site, ensured that Case study 2 was the worst. In fact, the WFs production at these WSs is not sufficient to cover the full load demand, and certainly enough to load the conventional generators to an almost full capacity. Thus, t_{SM} in Case study 2 is 397 s, as most of frequency deviation elimination process is carried out by the conventional plants. It should be highlighted that t_{SM} in Case study 2 is removed from Figure 7.6 to focus on the relatively smaller deficits occurring in the other cases.

The participation of WFs in the curtailment of frequency drops reduces Δf_{10s}, where all cases (excluding Case study 2) have enhanced results. In particular, WFs anticipated the continuous deterioration in frequency by providing a fast rise in active power as soon as Δf violated the predetermined safe margin. The best Δf_{10s} is achieved in Case study 5, as a result of the high values of K_{droop} and $K_{inertia}$, which amplified the amplitude of injected power surge. In spite of the poor WS conditions in Case study 2, the injected power by the WFs mitigated Δf_{max} by 0.2 Hz to within less

than 10 s (i.e., Δf_{max}-Δf_{10s}= 0.2 Hz). However, the values of K_{droop} and $K_{inertia}$ had a negligible influence on Δf_{max}, because the WFs already participate with all their clusters (i.e., Ni_{pc} = Ni_c) in the severe first one or two seconds of a frequency event, so that the major controller output (i.e., stage 1) had no influence in this period. Hence, the values of Δf_{max} are almost similar, excluding Case study 2, due to the accompanying low WS. The system frequency responses within 65 s after initiation of the frequency event are then shown in Figure 7.7. where the previous outcomes are insured. However, it is of note that the smoothest frequency response is obtained in Case study 5, as $K_{inertia}$ is reduced. Generally, the frequency responses in all the cases experience a slight rise just after the main drop due to the injected extra power by WFs when they are switched to support mode. Thereafter the frequency continues falling according to the delayed interaction of conventional generation but in a decelerated rate compared to the base case. This notable enhancement is the outcome of the WFs' contribution to mitigation of the frequency event.

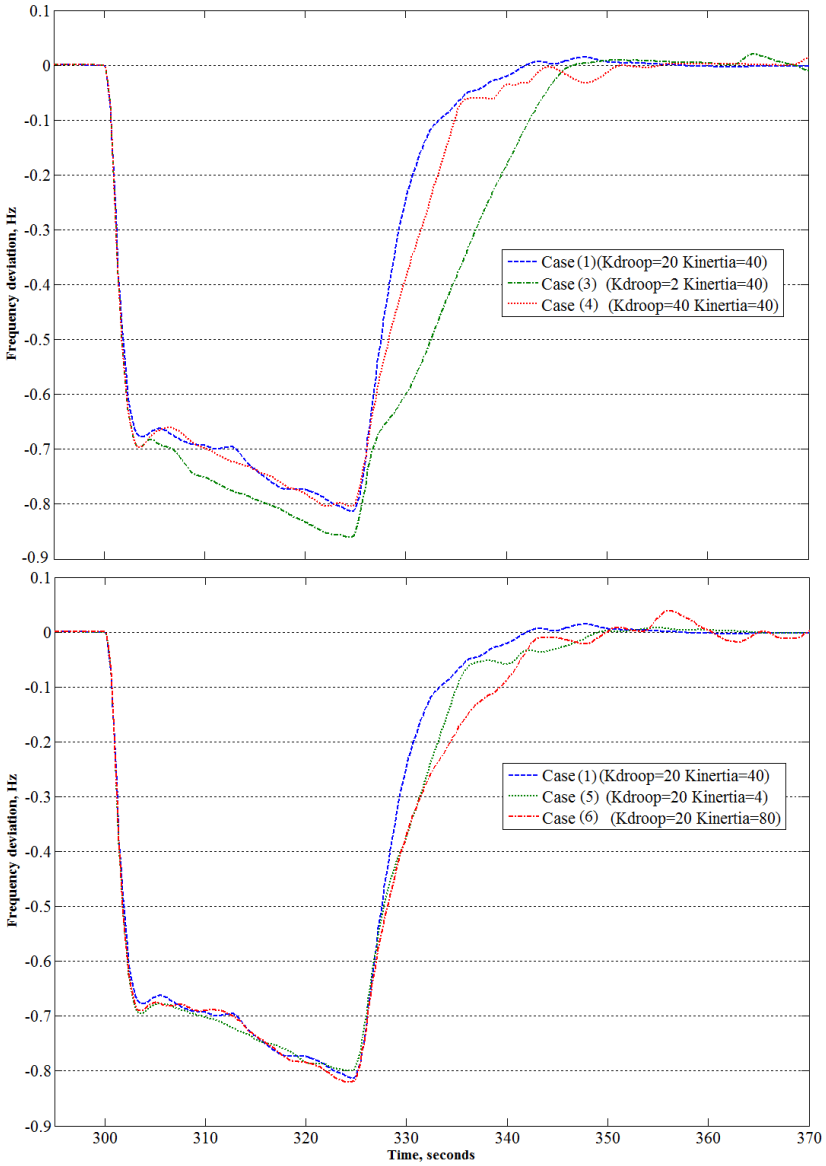

Figure 7.7 System frequency in certain cases of wind farm integration

7.3.2. Power generation variations

The next phase of this discussion highlights the profile of the total power generated by WFs during the dispatching process, as shown in Figure 7.8 and Figure 7.9. In this respect, the level of the WFs injected power is negatively affected during the frequency event in Case study 3, compared to in the other cases, as a result of the K_{droop} reduction which in turn mitigates Ni_{pc}. In addition, the highest $K_{inertia}$ in a case study, namely Case study 5, recorded output power spikes just before reaching stability margin. This relates to the time differential nature of this part of the controller, in addition to the impact of t_f, which leads to consecutive switching from normal to support mode and vice versa, within fixed time intervals. It is possible that further adjustments for t_f could smooth the WFs' output within this stage of the frequency mitigation procedure. It is of note that Case study 1 proved to have optimum values for K_{droop} and $K_{inertia}$, whereas the values in Case study 3 were worse.

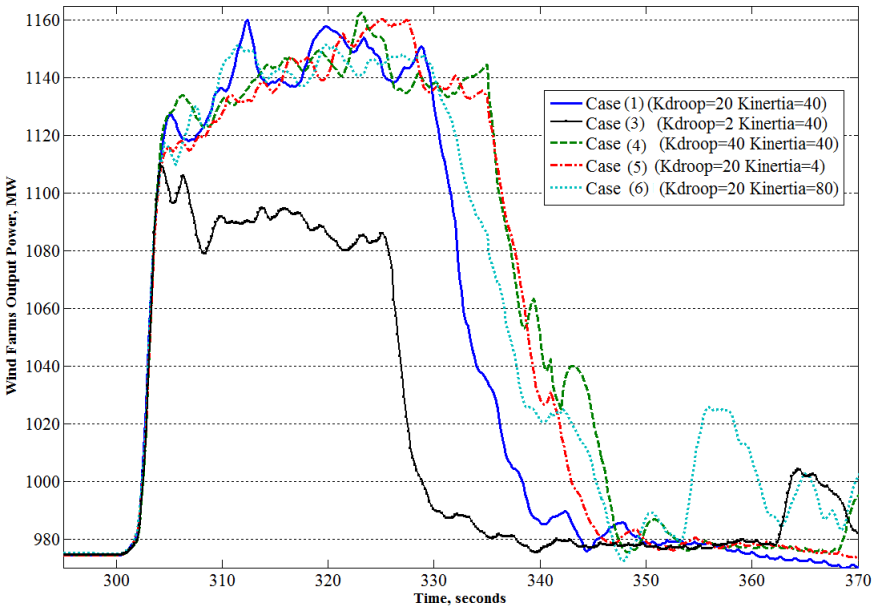

Figure 7.8 Wind farms overall output in selected case studies

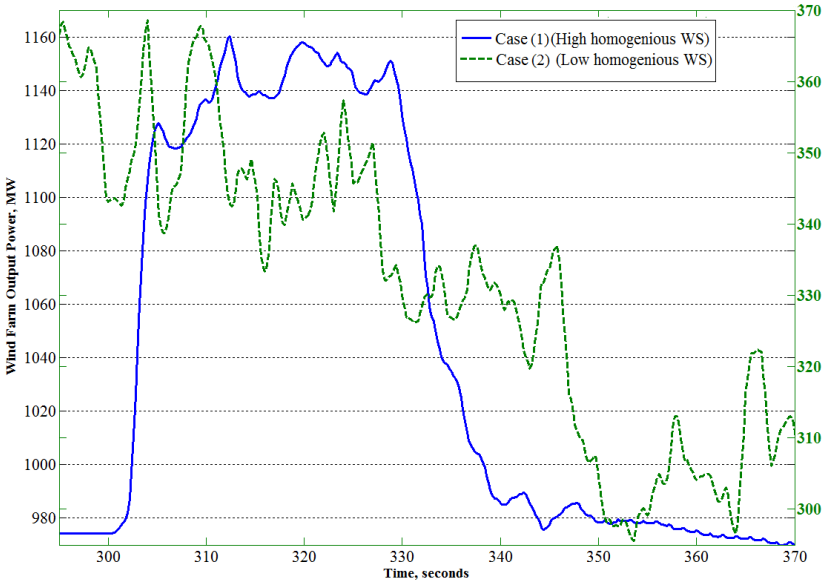

Figure 7.9 Wind farms output in Case studies 1 and 2

In relation to Figure 7.9, it is evident that the huge difference between the WFs' output power at high and low WSs is very notable in Case studies 1 and 2, respectively. The supplied power rise in Case study 2 is evidently limited according to insufficient wind energy. As an illustration, in Case study 1 the supplied power increases by about 140 MW within a few seconds of the frequency event, and conversely Case study 2 records only 60 MW. Furthermore, in Case study 1, the provided power support kept its average value constant within an acceptable period of 30 s. In contrast in Case study 2, the low WS caused several ups and downs in the WFs output, which are spanned by short time intervals (i.e., few seconds). These oscillations are mainly caused by the low amounts of stored KE in WTs, and the long recovery times required by WTs to retain their default rotational speeds before they are able to provide support again. In other words, in Case study 2, the support intervals are shortened but the recovery durations are extended. It should be highlighted that the delay in the conventional generation control signals ends after t=325 s, hence the required WFs support is mitigated after this time point. Attention is also focused on conventional generation in Figure 7.10, in particular steam generation, as it has a higher contribution. As expected, all cases are similar until t = 325 s, due to the imposed delay in the major power and frequency control signals. However, the general process of steam generation does not patently deviate from the base case. In other words, the base case trend is at this point similar to the corresponding curves in other case studies, but with rescaled values due to the WFs replacement of some conventional units, as explained in the previous section. Thus, the WFs supplied power share in load feeding reached 28% in high WS case studies before initiation of the frequency event. It is of note that the conventional contribution in Case study 1 is higher than that of Case study 5. This is related to the higher $K_{inertia}$ in Case study 1, so that the WFs utilize most of their supporting capabilities within the first 25 s after initiation of the frequency event, while at the same time the conventional reaction is retarded. In addition, Case study 5 experienced an oscillatory response in conventional output when the frequency approaches the stability margin, because the major controller cannot suppress Δf fluctuations due to the low value of $K_{inertia}$. Consequently, steam generation is reduced while the WTs are still able to provide support, or until the frequency reaches a safe margin on one side. On the other side, steam generation increases while the WFs are recovering their normal operational conditions.

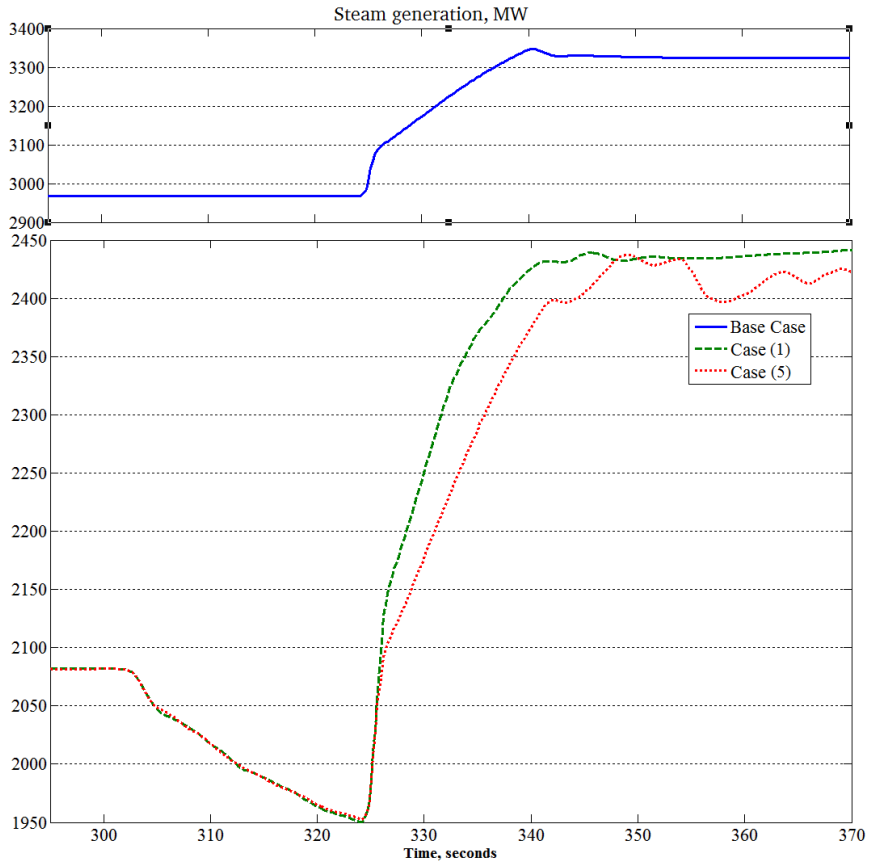

Figure 7.10 Output power of steam plant after occurrence of frequency deviation

7.3.3. Attitude of the main parameters of the proposed algorithm

It is useful to analyse the implemented algorithm internal signals; therefore, selected signals in certain case studies are emphasised. Firstly, droop and inertial controllers' responses are highlighted in Case studies 3 and 5 in Figure 7.11, so that the lowest K_{droop} and highest $K_{inertia}$ impacts are compared respectively. At the initiation of the frequency drop, inertial response fluctuates widely, and then reaches an average range. Meanwhile, the droop response is fully proportional to the frequency deviation through the K_{droop} value.

This initial spike in inertial response increases WFs reactions (namely, ΔP_{WFi}) to their peaks, so that all clusters are switched to support mode, but this lasts only for a very short duration. The droop controller aims to extend the WFs supportive participation for as long as the frequency violates the predetermined constraints. However, in both cases, the WTs recovery periods interrupt this supportive phase. A critical situation occurs when these recovery periods are synchronized with all the WTs, either in the same WF or across all the WFs, such that no support is provided by WTs within the same time interval. Practically, this worst-case scenario is very unlikely to happen, in relation to disparity in WSs probabilities and WFs properties.

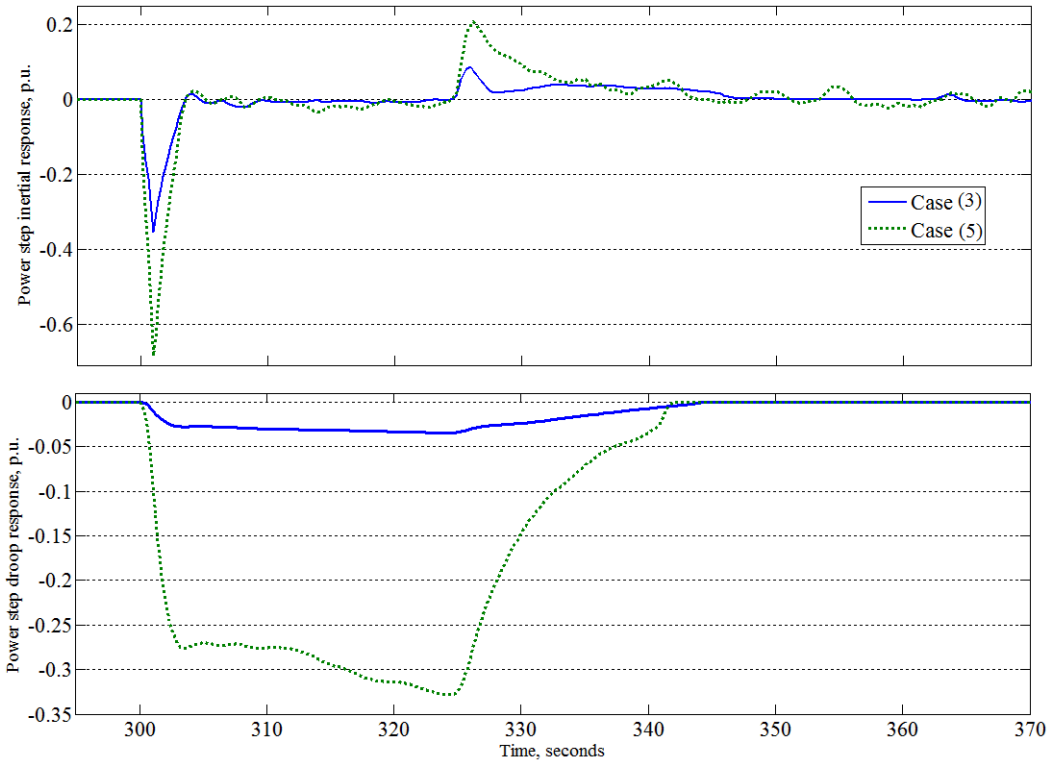

Figure 7.11 The two major control signals in Stage 1 responsible for all wind farms

Figure 7.12 presents ΔP_{WF8} in pu (on WF8 rating base); Case study 1 achieved a better performance from a ΔP_{WF} stability point of view during the critical time span just after the elimination of the major frequency deviation. In addition, there are no tough spikes, so that the risk of suffering a second drop is mitigated. In Case study 2, ΔP_{WF8} attained the maximum possible limit due to the low WSs, thus the extraction of all possible stored KE in all WTs is essential. However, the available wind energy is incapable of providing such power; hence, all clusters are switched to support mode during the frequency drop. Likewise, in Case study 4, ΔP_{WF8} remains constant for the longest time and records a steep rise at 337 s after the end of main supportive action due to the high value of K_{droop}, and the dead-band effect. In contrast, Case study 3 has an oscillatory response in comparison with the other case studies, caused by the low K_{droop} value, which means that the controller's response is highly affected by the intermittent nature of Δf, as proved before in Figure 7.7.

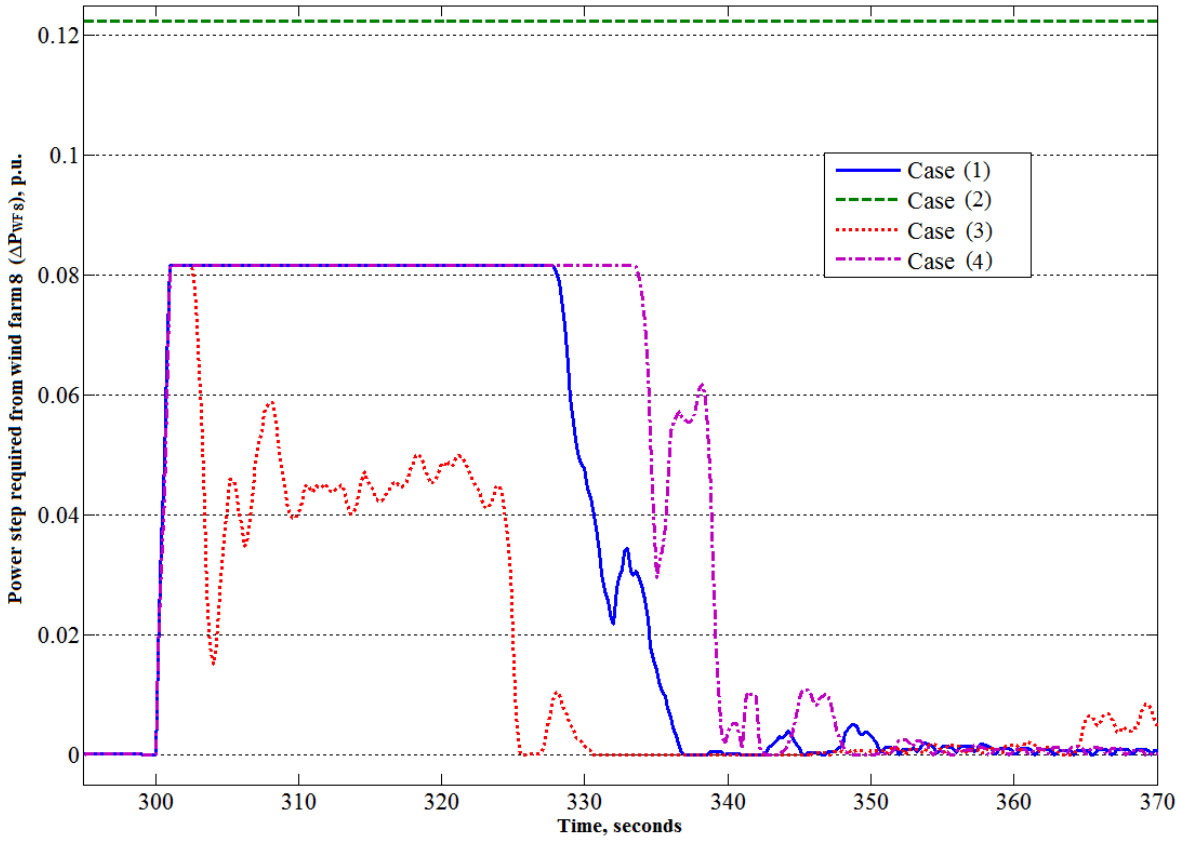

Figure 7.12 Required supportive active power contribution from WF no. 8

Finally, Ni_{pc} variations in WF no. 8 are analysed in Figure 7.13, where the impact of t_f is reflected on the regular step change in Ni_{pc}. In fact, all the clusters are switched to support mode immediately after Δf violates its safe margin, because the system seeks all available extra power. Afterwards, Ni_{pc} follows the corresponding response of ΔP_{WF} with respect to Figure 7.12. It is interesting to note the positive impact of t_f on the oscillatory nature of ΔP_{WF8} in Case study 3, and how t_f converts it to a regular step variation in $N8_{pc}$, thereupon smoothing the frequency recovery process as revealed before in Figure 7.7. In contrast, Case study 5 has only two steps (5 clusters), and then only one when the frequency approaches the safe range. Accordingly, frequency undergoes a minor drop (as in Figure 7.7) because 80% of WF8 is switched to normal and/or recovery operation instead of supportive operation.

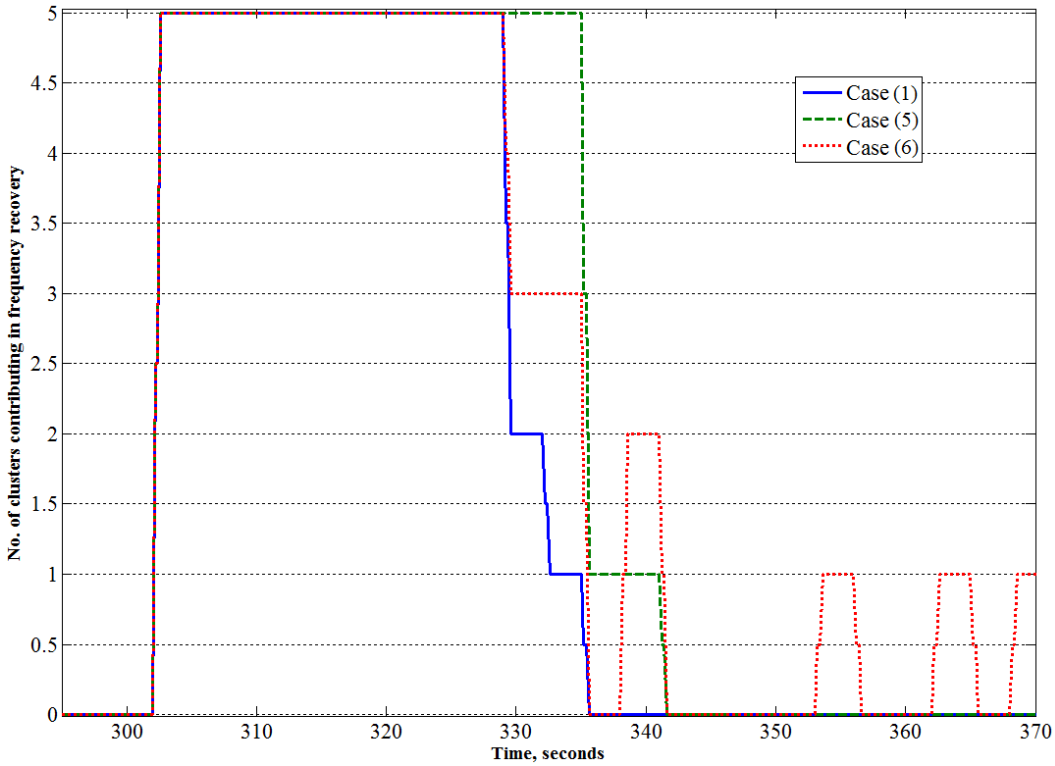

Figure 7.13 Number of clusters in WF no. 8 contributing to frequency recovery process

7.4. Summary

This chapter proposes a novel algorithm to dispatch WFs clusters during participation in frequency excursions curtailment. The dispatching of clusters is based on switching WTs included in each cluster between normal and support operational modes. The numbers of participating clusters in each WF is controlled according to the power required from the concerned WF to support the existing frequency deviation elimination. Estimating the required power from the connected WFs is executed through a droop-inertial controller in the algorithm initial stage. Afterwards, the share of each WF is determined in relation to several static and dynamic factors, including the annual average and instantaneous WS magnitudes. The proposed algorithm is simulated in certain zone in the Egyptian system and the wind energy expectations in some locations, and it is characterized by relatively medium wind energy penetration. Results indicated the validity of the proposed algorithm and its apparent beneficial influence on frequency response during drops. The proposed algorithm is so far universal, and can therefore be applied to different conditions accepting wide range of givens by tuning its parameters to match the concerned practical application. Moreover, one of the clear merits of the proposed algorithm is the centrality of its first stage composite controller, which determines the required extra active power support from all WFs facilitating and accelerating frequency events constriction. It should be mentioned that the settings in Case study 3 are preferable when accelerating the WFs response to frequency events is required. However, the settings in Case study 4 are favourable in cases of high wind energy penetration, especially when a certain ratio from conventional generators is acting as a rotating reserve to anticipate any sudden rise in load demand. Future work could investigate the complication level of the relation between ΔP_{WFi} and Ni_{pc}.

8. Storage banks for frequency support purposes

This chapter offers an algorithm to integrate storage battery banks in WFs to provide feasible power support during frequency events. This algorithm determines rated powers of storage stations and capacities according to several constraints, including WSs characteristics at the WF location. It controls storage bank charging, discharging, and standby modes based on the acquisition of different dynamic variables, for example WF output, load demand, and the storage cells' state of charge. This algorithm is applied on a defined sector from the Egyptian grid merged with real WSs chronological records at certain locations that are candidates to host WFs. Results reveal the positive influence of storage banks' involvement on frequency excursions clearance, and in addition, wasted wind energy is mitigated, WTs de-loading techniques are avoided, and some rejected wind power is utilized to charge the installed storage banks. Three main topics are to be discussed: battery bank sizing, charge/discharge control, and the expected impact on system frequency. The required storage capacity estimation is related to probabilistic forecasting for WS at certain locations. In addition, capacity design aim is to optimize the depth of discharge (DOD) so that battery bank life is intensively extended [99]. The charging and discharging times are also considered to judge the required ampere-hour capacity that allows extraction of all stored energy at a certain output power level.

8.1. Assessment of storage banks rated power

Generally, storage bank (SB) sizing depends on a multi-input process compromising between economical restrictions and technical aspects. However, this chapter concentrates on the technical side that mitigates negative impacts of high wind energy penetration levels on frequency recovery. The proposed algorithm acknowledges WS chronological records in a WF location, and the acceptable level of conventional generation participation in load coverage at normal operation. In other words, wind energy rejection is related to maintaining the participation ratio of conventional generation inside certain boundaries, according to dynamic acquisition for load and WFs output variations. The next steps describe using the implemented algorithm to determine the maximum possible expected charging power and the required overall energy SB rated power and capacity:

1. WS data at a specified site are obtained in high time resolution (average WS value every 20 or 30 s), based on the actual WSs records within the considered time span (e.g. 1 day).

2. WS arrays are incorporated with WFs models, including major details (e.g. pitch angle and rotational speed variations) to obtain WF's output power arrays according to the method explained earlier in Chapter 5. In this chapter, WS is assumed to be typical through the whole WF. Thus, the aggregation of installed WTs equals the output of any WT multiplied by the number of WTs inside the WF.

3. Required conventional generation contribution (CGC) is selected which is a percentage from its total capacity. For example, when CGC = 70%, conventional generation output fluctuates around this value during normal operation, according to the received control signals regarding load and WFs output discrepancies. However, minimum CGC is decided by SOs (WFs' output participation in load feeding should not exceed 50% according to certain codes). When WFs' outputs are high, so that the minimum CGC is violated, excess wind energy is "rejected" by the system.

4. Expected chronological load data should be available within the examined time span. Afterwards, the events at which the load is greater than generation are gathered in *Array 1* using (8.1). Note that, *Array 1* keeps the time instant at which each event occurred. Thereupon, each instant in an array resultant from the previous step is subtracted from the corresponding output power of all integrated WFs at the same instant using (8.2). Hence, the positive events in *Array 2* refer to the WFs rejected power, which could be imposed to charge battery banks. Thus, SB energy capacity and rated power could be estimated. It is of note that low CGC leads to remarkable reduction in the density of rejection events, as shown later.

$$Array\ 1 = \text{Negative values of } \left(Load - \mathrm{CC}_{new} \cdot \mathrm{CGC}\right) \tag{8.1}$$

$$Array\ 2 = \text{Positive values of } \left(WFs\ output - Array1\right) \tag{8.2}$$

5. The average of the rejected power events obtained in step 4 is calculated to obtain an initial value for SBs' power rating based on the average charging power rating (ΔPC_{total}). Nevertheless, it is unrealistic to design storage stations to handle all the expected rejected power, for economical reasons. Additionally, most probably this rejected energy will not be fully utilized (i.e., after being stored) as demonstrated by most of the mentioned literature. Therefore, the expected rejected power should be reduced by a roughly assumed ratio, namely 20%, as in this chapter (which is inspired by outcomes of certain previous literature), but this reduction ratio could be accurately evaluated using probability studies.

This simplified method is applied to reduce simulation and computational efforts. Otherwise, comprehensive data is required on the history of load-supply mismatch events, which cause moderate frequency deviations. Thus, the overall storage power rating is selected to cover a certain share from the extra demanded power

The rated power of each SB is estimated where a fixed ratio, known as the storage contribution factor (SCF_i), is determined for each SB. SCF_i is then multiplied by ΔPC_{total} to obtain the required rated power of each SB. Two procedures are suggested to evaluate SCF_i: *In the first method*, SCF_i^{1st} is obtained using (8.3), where 'm' no. of WT types in the same WF.

$$SCF_i^{1st} = \frac{\left(WS_{i\ avg}/m\right) \cdot \sum_{k=1}^{m} \frac{PWT_{k*}N_{WT-k}}{WS_{rated-k}}}{\sum_{i=1}^{m} \text{Nominator value}_i} \quad (8.3)$$

This formula nominator is evaluated according to the participation of each 'WT_k' type (i.e., the ratio between the number and rating of each WT type with respect to other types installed in the same WF). A resulting value is then obtained for all WTs types, taking into consideration WS_{avg} at the WF location. *In the second method*, at each time step WF_i output power is divided on the overall WFs output. Thereafter, an average value for all ratios within the considered time span is calculated (SCF^{2nd}_i). However, this algorithm requires enormous simulation and computational efforts when it is applied to the whole year's chronological data. In this research work, it is applied only on four specific days; the days of highest average loads in each weather season, as shown in Table 8.1. Finally, a compromise between the two methods is applied in this using (8.4) to calculate SCF_i, where 'M' is the number of SBs (i.e., WFs). This compromise is applicable as the considered time span (i.e., 4 days) is relatively short, so that both methods are computationally feasible, and integrating the two methods reduces the possible higher error in the first one. However, literature had also calculated storage power ratings using other simplified methods. For example, the storage power rating is a fixed percentage of the WF overall capacity (10 - 15% according to the results of [76, 77]).

$$SCF_i = \frac{SCF_i^{1st} + SCF_i^{2nd}}{\sum_{i=1}^{M}\left(SCF_i^{1st} + SCF_i^{2nd}\right)} \quad (8.4)$$

Table 8.1 Four sample days according to Egyptian grid load data

Season	Winter	Spring	Summer	Fall
24 h average load, GW	14.9	13.2	14.6	16.3
Time span (hours in year)	217-240	4273-4296	6529-6552	7561-7584

Afterwards, the number of battery cells required for each WF's SB is estimated based on the power rating of the selected cell type. Consequently, the number of cells (CN_i) composing each WF's SB is obtained by dividing ΔPC_{total} by the power rating of a single cell.

The precise location of SB inside the WF does not have deep impact on its role of supporting system during frequency drops. However, it is more practical to construct SB warehouse near the substation that connects the WF to the grid.

8.2. Storage bank operation

The proposed algorithm is split into two modes (normal and support), and it depends on four control signals: load demand, WF output power, *SOC*, and frequency deviation (Δf), as well as the predetermined CGC fixed value.

8.2.1. Normal Operation

Two possibilities are considered in this operational region: charging and standby (i.e., neither charging nor discharging) modes. Charging activation requires the overlap of the two following conditions:

$SOC < SOC_{max}$

$[(Load_{inst} - CGC \cdot CC_{new}) \cdot SCF_i] > WF_i$ output (i.e., the presence of excess power in WF_i)

SCF_i has a different application in Normal operation algorithm, as it represents the expected share of WFi in the load coverage. However, selection of SOC_{max} and SOC_{min} is related to DOD, which has a severe impact on battery lifetime. In words, SB_i is charged by a power step (ΔP_{ch}) obtained using (8.5).

$$\Delta P_{ch\,i} = WF_i \ output - (Load_{inst} - CGC \cdot CC_{new}) \cdot SCF_i / CN_i \quad (8.5)$$

Nevertheless, the share of each storage cell from ΔP_{ch} should not violate the rated current and voltage of the installed cell type. Particularly, when the output of the WF is such that ΔP_{ch} is higher than SB ratings, the extra power is directed to feed the existing load; hence, CGC is decreased below its predetermined value. Thus, conventional generators output is reduced, in parallel with suitable adjustments in the converters which control the power flow from WF to grid and SB. Hence, the amounts of wasted or rejected wind power are reduced. It is of note that ΔP_{ch} is handled by certain number of AC/DC converters, as shown in Figure 8.1.

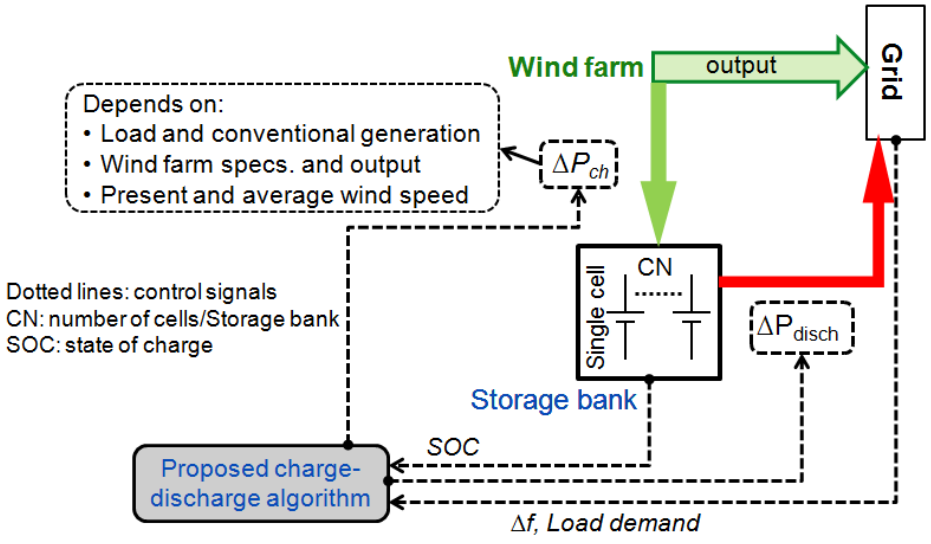

Figure 8.1 Major blocks and control signals of wind generation and storage bank

The number of integrated converters depends on the ratings and budget of available power electronics devices. Some literature prefers a single converter for each WT, and in other approaches, one converter is responsible for several WTs. Likewise, DC/AC converters link between SB and the power system. For simulation simplicity, the ΔP_{ch} is interpreted as a charging DC current fed into storage cell model using (8.6). Moreover, minor losses and time delays of power electronics devices are ignored.

$$i_{\text{charging}} = \frac{\Delta P_{ch}}{\text{V}_{\text{ci}} \cdot \text{CN}_{\text{i}}} \tag{8.6}$$

8.2.2. Support Operation

Support operation is activated when Δf violates a predetermined limit based on grid requirement (similar to previous chapters the safe margin is -0.05 Hz), as long as $SOC > \text{SOC}_{\text{min}}$. In support mode, the WFs outputs are completely exploited to cover the load demand ignoring SB charging even if CGC predetermined value is achieved. The provided power step is considered to be constant ($\Delta\text{P}_{\text{disch}}$) leading to a curtailment of the generation – demand mismatch. The value of $\Delta\text{P}_{\text{disch-i}}$ is calculated using (8.7), where V_{ci} and I_{ci} are the rated voltage and current of SB cell type, respectively.

$$\Delta\text{P}_{\text{disch i}} = \text{Vc}_{\text{i}} \cdot \text{Ic}_{\text{i}} \cdot \text{CN}_{\text{i}} \approx \Delta PC_{total} \cdot \text{SCF}_{\text{i}} \tag{8.7}$$

Most of highlighted support techniques, based on WTs stored KEs, face the risk of causing a second frequency deviation after the depletion of extractable KE. In contrast, SBs have fixed predetermined participation for certain defined duration (i.e., $\Delta\text{P}_{\text{disch-i}}$ continues for certain support time (t_{SB}) to reduce the probability of second frequency excursion occurrence). t_{SB} starts counting when Δf reaches its safety margin for the first time after a frequency event and it is reset when Δf violates the safe limit. However, t_{SB} completion depends on SOC value such that it is prevented from violating SOC_{min}. $\text{t}_{\text{SB-i}}$ is adjusted on a proportional basis to CN_{i} using (8.8) to dispatch WFs' contributions. Thus, the switching of all SBs from support mode to normal mode is not synchronized to mitigate the risks of successive frequency events and incident fluctuations. For instance, the longest t_{SB} is provided by the SB with the highest CN ($\text{CN}_{\text{highest}}$) taking into consideration that all the cells in all SBs are typical. The $\text{t}_{\text{SB-longest}}$ value is predetermined by operators (it is assumed to be 90 s so that it is relevant to the average duration of complete clearance of moderate frequency deviations) and based on this, the $\text{t}_{\text{SB-i}}$ values of other SBs are evaluated. For further illustrations, the numerical outcomes of proposed algorithm are presented in the next section.

$$t_{SB\text{-}i} = \frac{CN_i}{CN_{highest}} \cdot t_{SB\text{-}longest} \quad (8.8)$$

8.3. Test system and case studies

8.3.1. Test system

The test system implemented in this chapter considers a certain sector of the Egyptian 50 Hz power system, which is the same zone implemented in Section 7.2, where **nine** WFs replace a certain portion of the former conventional generation. Two types of WTs are integrated, namely, GE-77 and G-90, and each WF includes 65 units from each type. This chapter assumes that integrated WFs actual capacity is 50% of their rated powers, namely 1024 MW (i.e., [9 (no. of WFs) · [65 (no. of WTs from each type) · [1.5 (rated power of GE-77) +2 (rated power of G-90))]] · 50% (assumed capacity factor)]). Thus, the CC_{new} is 2801 MW (3825-1024) and the average wind power penetration is 27% of the former conventional capacity. High resolution arrays of WSs at a 15 s time step are integrated so that the impact of WS dynamics is acknowledged. The Egyptian grid chronological hourly load is integrated after being de-rated by 79.9% (the ratio between the concerned sector generation capacity and the whole grid capacity is 20.1%).

8.3.2. Case studies

The base case study analyses the system frequency response during two successive frequency excursions caused by a sudden rise in load demand by 8% from its actual amount (2838 MW). It then rises steeply again after 45 s by an additional 3%.

The first and second case studies examine the frequency responses after WF integration, without installing of SBs (Case study 1), and with SBs installed (Case study 2). The benchmark system single line diagram, accompanied by major aspects of both implied case studies is displayed in Figure 8.2. It is of note that the operation of the WTs in all cases is by traditional MPT, and the harvested wind energy is fed to load or charge the SB, or is rejected according to the algorithm previously explained.

Figure 8.3 describes the variation of ΔPC_{total} depending on the CGC value selection in the proposed algorithm. ΔPC_{total} escalates almost linearly with the increase of CGC. As an illustration, the rising CGC expands the wind power rejection possibility, thus more power is available to charge the SBs. Noticeable divergence between the four sample days relates to different WS conditions in all WFs, and the chronological load demand. Thus, spring day results are excluded from calculating ΔPC_{total} average value, due to the very low expected rejected power on that day. However, ΔPC_{total} average value for the three days at CGC=70% is implied (i.e., ΔPC_{total} = 178 MW equivalent to 4.7% from sector capacity).

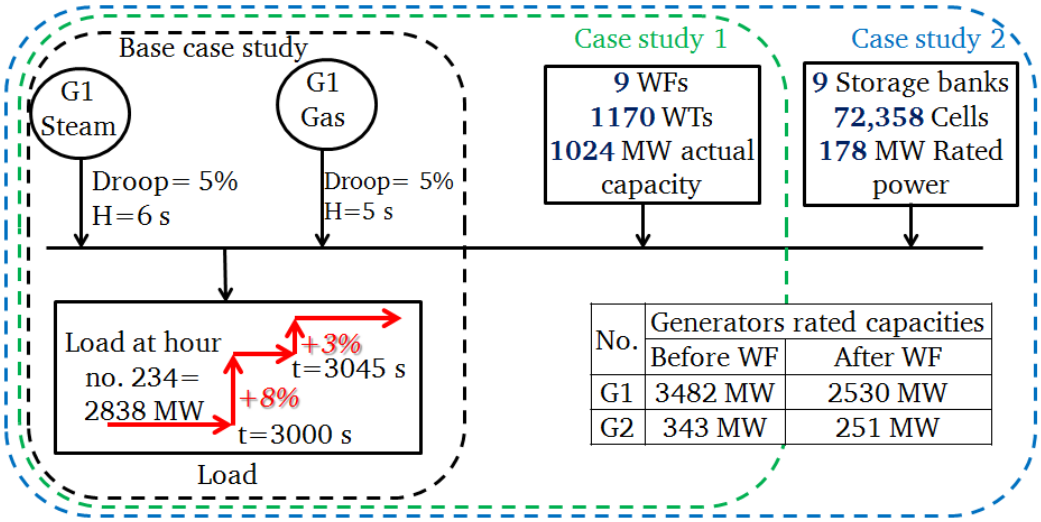

Figure 8.2 Single line diagram indicating applied case studies

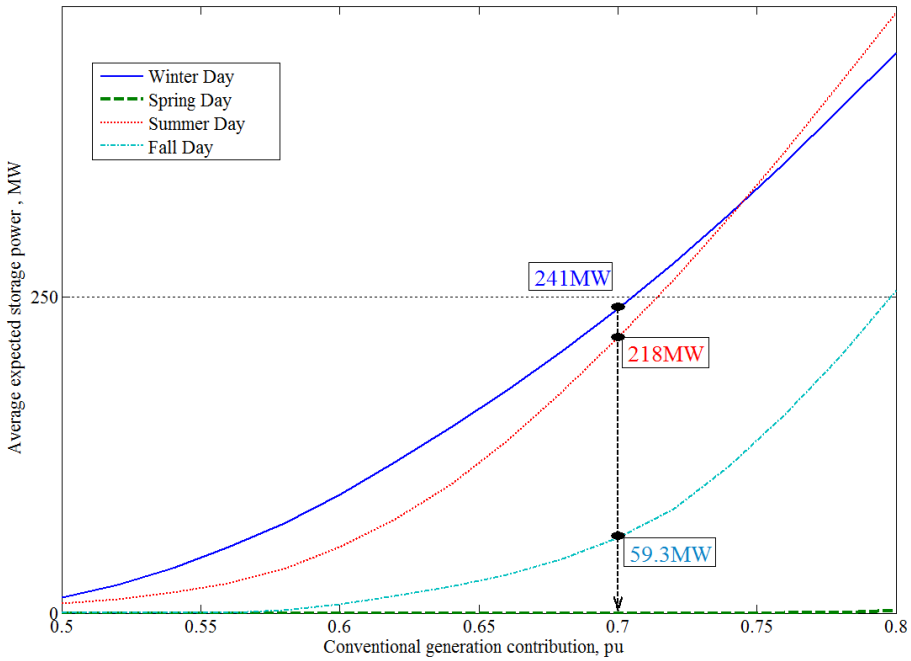

Figure 8.3 ΔPC_{total} vs. CGC on the four indicated sample days

The SB sizing algorithm is applied on the four sample days, providing four various values for ΔPC_{total}, SCF^{1st}, and SCF^{2nd} on each day; hence an average value is calculated for each factor (shown in Table 8.3). However, the error between SCF^{1st} and SCF^{2nd} is considerable, and basically depends on the selected time span for performing the proposed sizing algorithm.

In this research work, only one type of storage cells is exploited for all SBs, namely the Trojan (L16RE-B) battery cell, the characteristics of which are shown in Table 8.2 [100]. DOD is assumed to be 55%; hence, battery lifetime should obviously be extended according to manufacturer's recommendations. Consequently, SOC_{max}=85% and SOC_{min}=30%, while the initial *SOC* in all case studies is assumed to be 70%. The universal battery model embedded in Simulink, and inspired from [101], is implemented to simulate accurate SB cell responses, including the storage units' losses. The

hangar (storage places for the battery banks in each WF) areas included in Table 8.3 are calculated using (8.9). For instance, it is assumed that all the hangars have the same height of 10 m, thereupon 12 cells could be aligned vertically allowing an overall spacing between cells of 30%. The extra spacing in the horizontal distribution of cells columns is 60% of the exact area of the horizontally spreading cells. The outcome hangar areas seem to be reasonable, especially if compared to either substation areas or huge areas of WFs' terrains.

$$\text{Hangar area}_i = \frac{\text{CN}_i}{12} \cdot \text{cell base area} \cdot 1.6 \tag{8.9}$$

The winter day data is selected to execute the mentioned case studies as it recorded the highest superfluous amounts of wind power. Thus, the proposed algorithm is examined at a high wind energy penetration level. The simulation time for each case is one hour (18:00–19:00) as the load is relatively high and the wind power is moderate within this duration. Control signals concerning load variations and Δf fed to conventional plants' governors are delayed by 20 s after the first frequency event starts. This delay emphasizes the WFs impact on the development of frequency excursion in its early stage.

Table 8.2 Integrated (L16RE-B) battery cell technical aspects

Rated power	Energy capacity	Rated voltage	Rated current	Base area	Height
2.46 kW	410 A.H	6 V	410 A	1763 cm^2	61 cm

Table 8.3 WFs storage banks basic parameters

WF location	SCF^{1st}	SCF^{2nd}	Merged SCF	t_{SB}, s	CN	Hangar area, m^2	$\Delta P_{disch,}$ MW
Ras Ghareb	0.23	0.13	0.238	90	11531	271.1	42.31
NW	0.19	0.13	0.185	71	8969	210.8	32.91
Nweiba	0.28	0.09	0.101	39	4896	115.1	17.97
Zayt	0.28	0.14	0.209	80	10152	238.6	37.25
Abu Dara	0.28	0.20	0.178	68	8658	203.5	31.77
Nabq	0.13	0.01	0.161	61	7805	183.5	28.64
Port Said	0.20	0.15	0.071	27	3439	80.8	12.62
St. Paul	0.24	0.11	0.173	66	8413	197.8	30.87
Ras Sedr	0.15	0.05	0.175	67	8494	199.7	31.17

8.4. Results and discussion

The base case study is considered as a reference to assess the impact of wind energy integration with and without SBs. In Figure 8.4, the system frequency responses are displayed until 80 s after the first frequency event is initiated. The forced delay in the control signals from conventional plants governors is clear, so that the frequency begins recovering after 20 s in the base case. However, the integration of WFs accelerated the recovery process, but failed to reduce the maximum Δf. As shown in Figure 8.5, the relatively high, or moderate, WS in some WFs during frequency excursions caused this positive consequence. Meanwhile, the positive impact of SBs is clear, as it mitigated Δf_{max} by 0.2 Hz and derived Δf to a safety margin within 6 s, compared to 22 s in Case study 1.

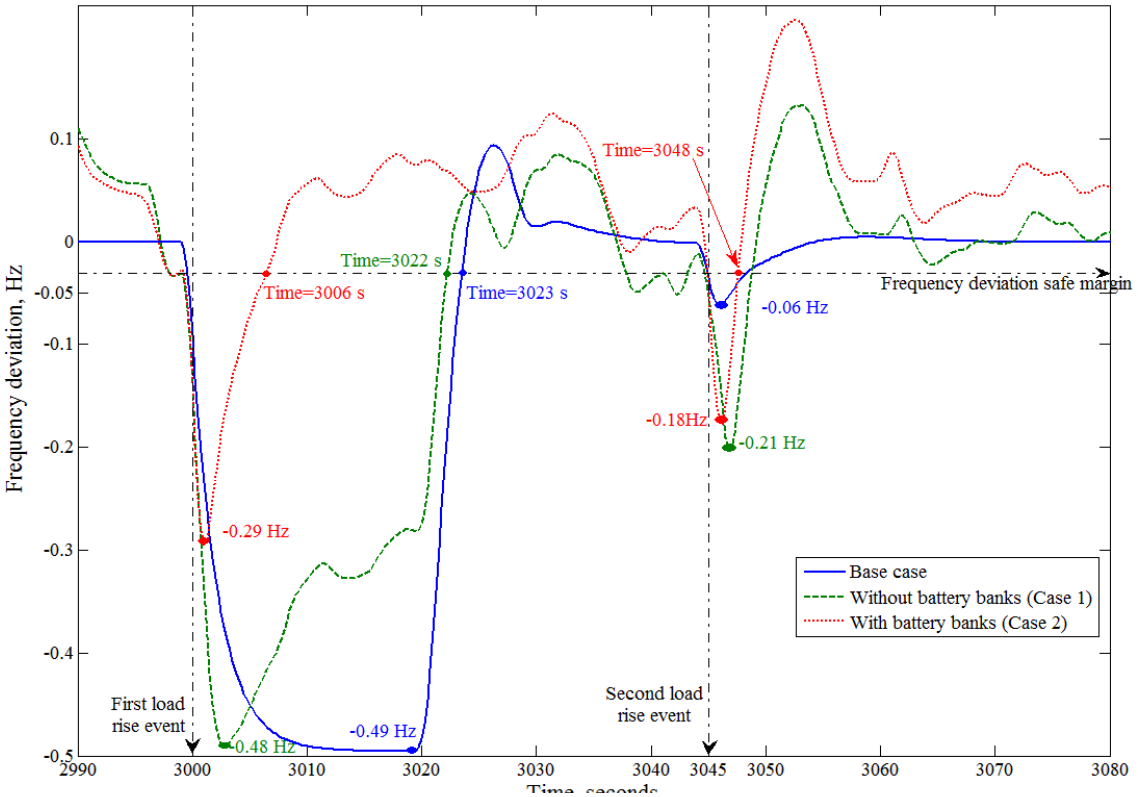

Figure 8.4 System frequency responses in all case studies during frequency events

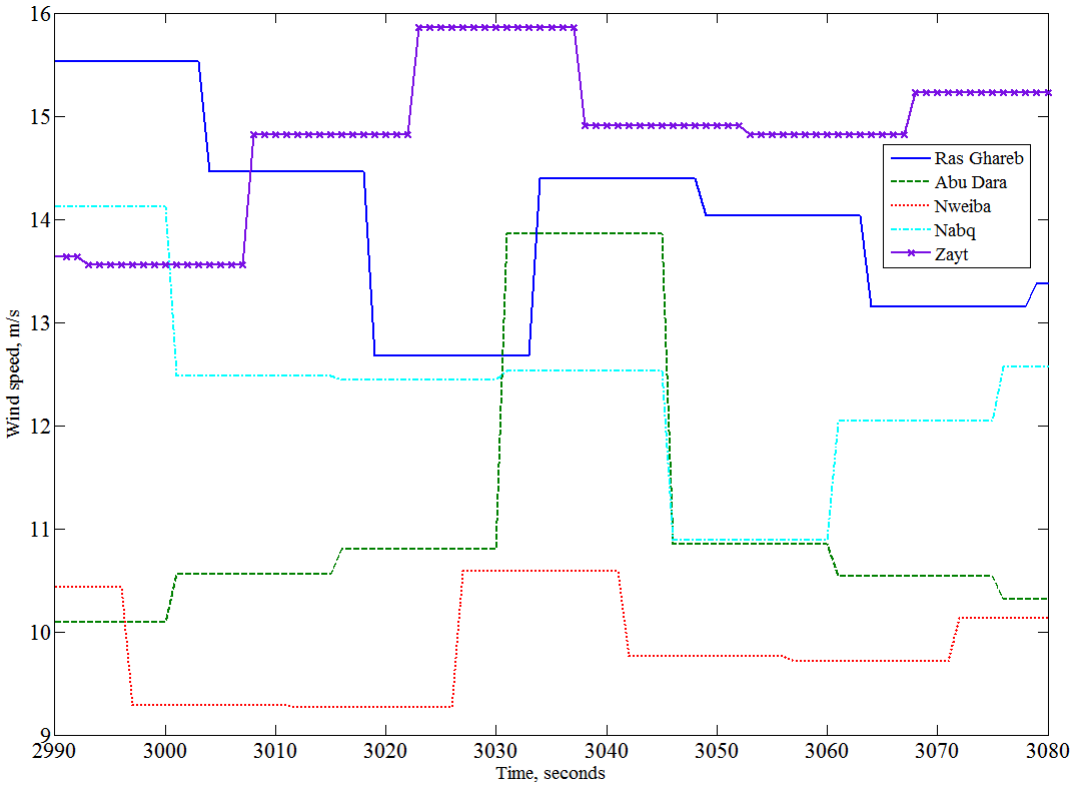

Figure 8.5 Wind speeds in five WFs during the frequency events

Moreover, the resultant frequency fluctuations are not severe, and could be handled. In the second frequency event, the conventional generation reaction is not delayed; hence, the recovery process starts earlier. Nevertheless, the positive effect of the SBs is still apparent, so that Δf_{max} is mitigated,

reaching its acceptable threshold faster than in Case study 1. The major drawback is represented by a relatively positive Δf overshoot. In particular, the positive Δf occurring after each frequency excursion clearance is an expected result in relation to the extra power fed by the SBs within the different t_{SB} duration. In other words, the SBs supportive power continues even after Δf reaches its acceptable value, until t_{SB} ends. As previously illustrated, the independence of SB supporting the power continuity from Δf is the cause of this overshoot. To fix this problem, $t_{SB\text{-}longest}$ could be shortened, or t_{SB} and ΔP_{disch} adjusted dependently on Δf instantaneous value through a certain droop function. However, linking ΔP_{disch} to Δf would generate high undesired fluctuations in the SBs output power. Generation variations during frequency drop clearance are considered in Figure 8.6. Wind power penetration at the instant of the frequency excursion is 48% of the whole load demand. In spite of this high WF participation the frequency attitude is not negatively affected, but it slightly improves, even without the SBs integration. Conventional generation is evidently reduced in Case study 2 compared to Case study 1, due to the SBs contribution. Additionally, there is almost no deviation between the steam generation curves in Case studies 1 and 2.

Conversely, conventional generation supplies more power to compensate the power injected by WFs when the SBs are connected, to charge the connected SBs. As shown in Figure 8.7, all batteries banks reached SOC_{max} prior to the displayed time interval within the simulated hour (consider that the initial *SOC* is 70%, as mentioned earlier). As an illustration, moderate WS conditions during the simulation interval caused *SOC* to reach its optimum value before the first frequency event.

Focus is now directed to the output of certain SBs during frequency events, as shown in Figure 8.6. The output power of all SBs within the first few seconds increases rapidly to a value of 182 MW, which is higher than the rated power of all the SBs, because the transient voltage response of the installed cells implies voltage overshoots accompanied with rated currents that cause this high output. After a few seconds the aggregated output settles down to its normal rated power of 178 MW, but then faces an intended decrease after 43 s because the t_{SB} of some SBs have run out, at Port Said and Nweiba SBs, as indicated in Table 8.3. As soon as the second frequency event happens these two SBs are switched again to the discharging support mode and their t_{SB} are reset. It is of importance that the major merit of SBs over other support techniques is accentuated under these severe circumstances. As an illustration, in traditional support techniques, WTs require a certain amount of time to re-store KE and attain their normal rotational speeds; hence their chances of providing further support in the case of a second successive frequency event diminish. Conversely, SBs are able to interact positively to a second frequency deviation as long as the *SOC* is sufficient, whereas their reacting speed depends on the time constants of integrated batteries and installed power electronics devices. In addition, the offered SBs support algorithm does not require any instantaneous measurements of WS and it thus evades the debate of possible errors and negative influence on the feasibility and consistency of the other support techniques. The internal performance of some of the selected cells is also included in this discussion, as depicted in Figure 8.7. In the proposed algorithm, the available extra wind power

(i.e., utilized for charging of SBs) is equally distributed among the installed cells. Therefore, the SOCs of all cells in the same SB are typical, as shown in Figure 8.7. The Nweiba *SOC* reaches its optimum value after certain delay (compared to the other two SBs) due to poor WSs conditions; hence, the WF output is barely sufficient to cover its forecasted share in load coverage, and the charging power is restricted. At the excursion instant, all cells are discharging by the same rate as all of them are discharging at their rated outputs. The same concept is ensured by the discharging currents' of the three different cells.

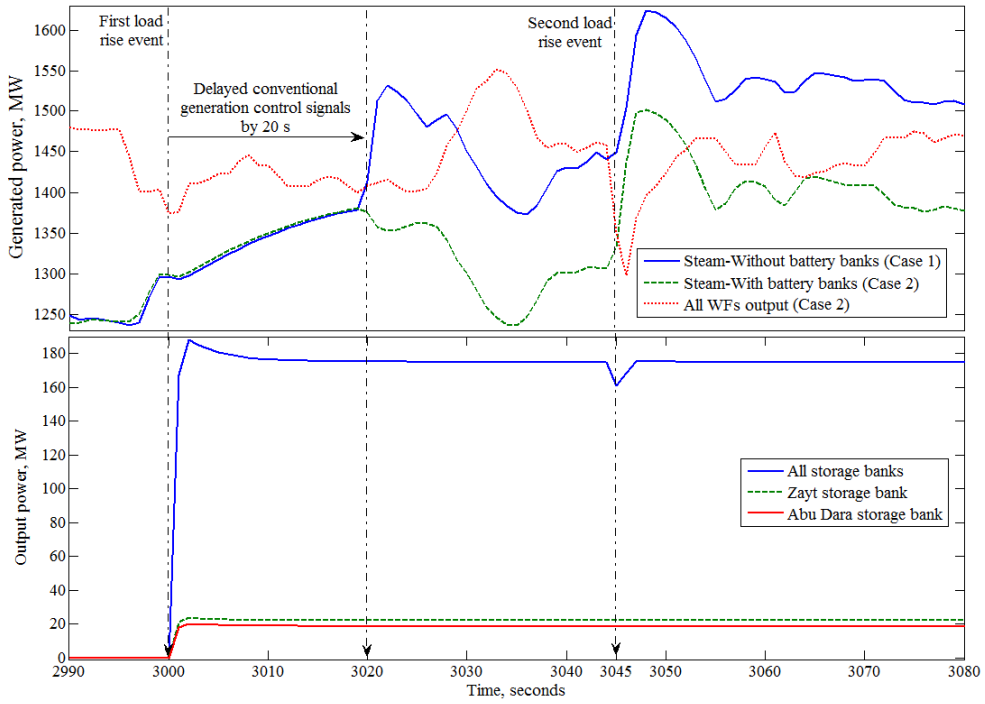

Figure 8.6 Conventional, WFs, and storage banks output powers

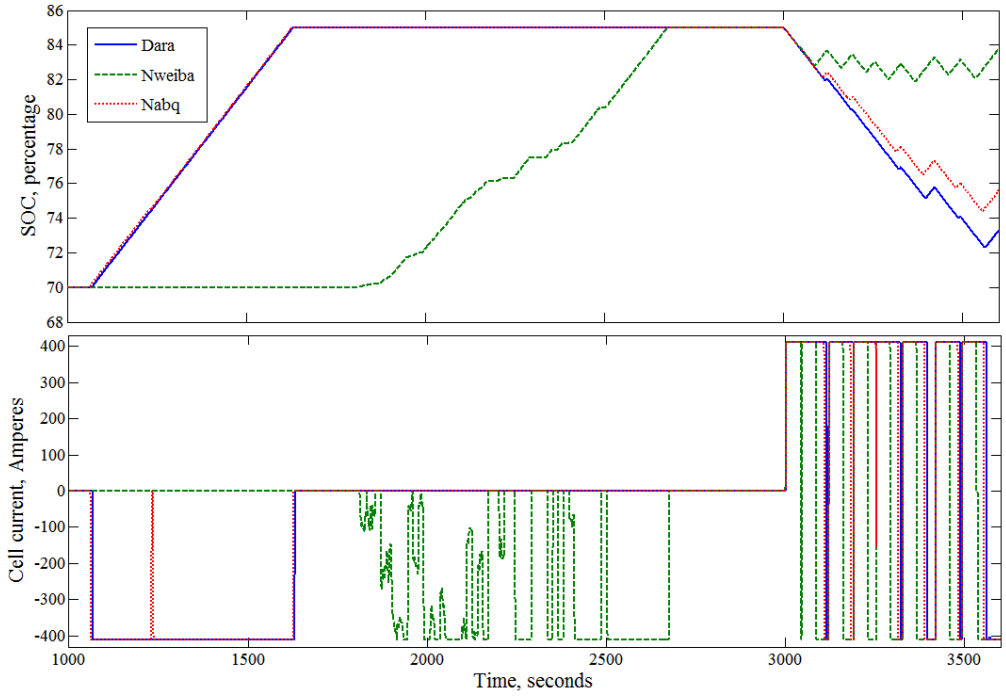

Figure 8.7 Selected battery cells internal parameters performance

The discharging current is always fixed at its rated value to provide the pre-adjusted ΔP_{disch} from the whole SB. However, the negative charging current fluctuates all the time according to WS variations, which determine how much excess power is available to charge the cell (e.g. Nweiba SB). The high WSs in the Abu Dara and Nabq sites caused a fixed rated charging current, which is an advantage to the cell life span. Either during charging or discharging the current is limited to its rated value to avoid any damage. In addition, steep changes in current variations are interpreted by ignoring the power electronic devices time delays and their transitioning stages, as these are extremely short compared to the time required by the system inertial responses and frequency variations. The intermittent discharging period after the end of the main frequency events is caused by further minor frequency excursions created by variations in the WFs output. These wind power oscillations caused a mismatch between generation and demand, and thus the system frequency suffers either drops or overshoots so that the SBs react to Δf based on the proposed support algorithm. Figure 8.8 affirms the existence of different discharging periods related to the pre-defined t_{SB} durations. The Nweiba SB has the shortest t_{SB} in comparison with Abu Dara and Nabq SB (of 39 s). In relation to the time instant at which Δf reaches its safe margin after the first excursion (3006 s), $t_{SB\text{-}Nweiba}$ ends at 3045 s. Meanwhile, Abu Dara has longer t_{SB} (69 s); hence, it does not end after the first frequency event, because the second excursion occurs prior to t_{SB} completion. However, it ends after Δf stabilizes in the safe region (at 3048 s as shown in Figure 8.4), and thus the Abu Dara discharging mode stops at time = 3048 + 69 = 3117 s, as shown in Figure 8.8.

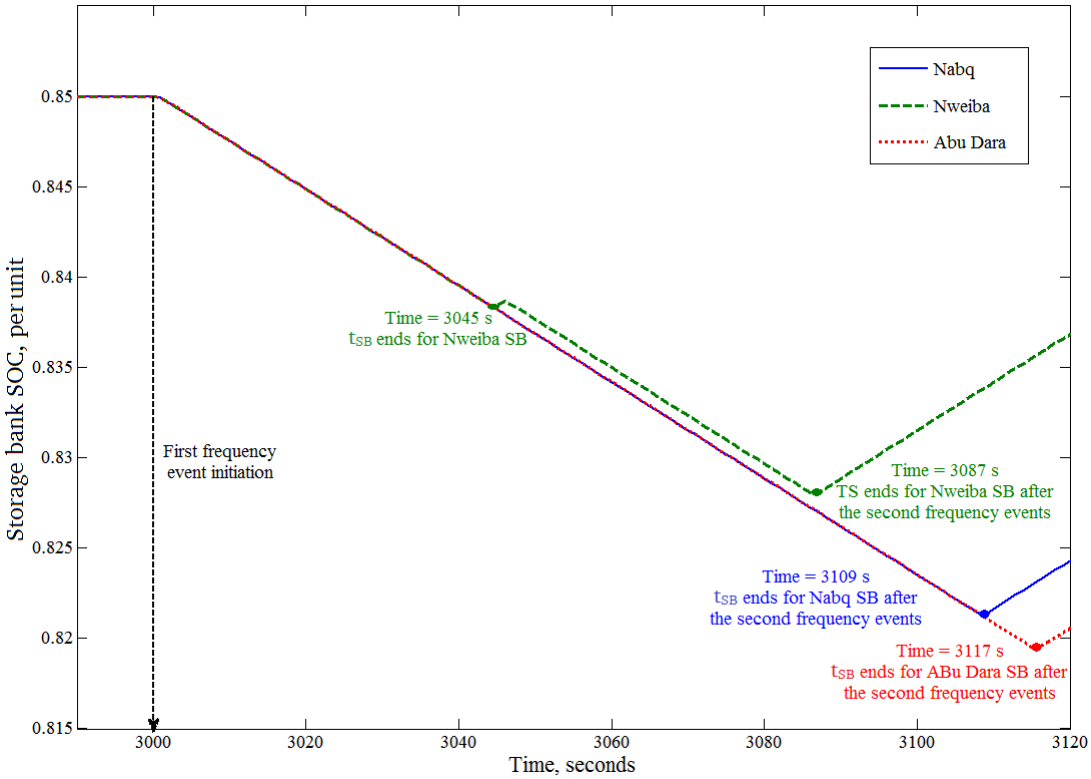

Figure 8.8 *SOC* of selected cells within 2 min after the first event

8.5. Summary

This chapter considers the impact of the integration of WFs in power systems in relation to frequency response, particularly at frequency excursions. Battery storage banks are used to overcome any possible drawbacks in moderate levels of wind power penetration in conventional grids. This chapter focused on providing a feasible and detailed algorithm to estimate the power rating of the required SBs. In addition, it offered a consistent methodology for driving the installed SB in each WF, either during normal operating conditions or during frequency drops. Both algorithms are implemented in a certain sector in the Egyptian grid using real WS data. A detailed analysis of frequency responses, generation variations, and cells' internal parameter fluctuations are conducted. The obtained results designate the positive influence of the applied algorithm on mitigating frequency excursions and curtailment of the required time to reach the frequency safe margin.

9. Conclusions, recommendations, and future work

This thesis is focused on the problem of wind power fluctuations and its impact on power system frequency, especially during excursions. The first proposed algorithm presents the concept of wind turbine speed control to manage the amount of stored kinetic energy in wind turbine rotating parts. This stored kinetic energy is depleted during frequency events by a decelerating wind turbine speed. The amount of active power support depends on several static and dynamic factors, including wind speed and wind turbine inertia. It also depends on the pre-adjusted time span through which this extracted energy is released. According to the achieved results, the average time duration required by the wind turbine to utilize the available kinetic energy is in range of 9 to 15 s in correspondence with wind turbine inertia. The amount of step rise in output active power is variable and determined by the frequency deviation severity, as well as the tip speed ratio's initial and final values. The frequency deviation improvement is in the range of 10 mHz, but this improvement could be fixed or variable based on the selected mode of the 'M' parameter calculation. As a recommendation, it is preferable to keep 'M' fixed as an average value to reduce calculation time and efforts, and to simplify the integrated control equipment. However, variable 'M' mode causes further suppression of frequency oscillations and facilitates the forecasting of the system performance during drops.

The second algorithm applies different concepts and merges through more complicated operational regions that are classified based on an approximate value of the instantaneous wind speed. This algorithm gives the wind turbine the opportunity to select better solutions to ensure the presence of excess active power support. In addition, it partially treats the problem of a wind speed drop during the activation of support mode, so that the negative impact is almost eliminated or strongly mitigated. The wasted energy is this algorithm is slightly higher than the first one; however, it is more flexible and provides higher levels of support. Therefore, the enhancements in frequency response during drops are clearer in the second algorithm. Nevertheless, the amount of wasted energy in the second algorithm is less than the continuous de-loading algorithm by 50% on average. In fact, the amount of saved energy is directly proportional to the wind speed conditions and wind turbine rating.

Comparing the second algorithm's results to corresponding results obtained in [11, 102] ensures the advantage of the proposed algorithm. As an illustration, the actual wind energy penetration in the presented cases is 26%, but the penetration levels in [102] are 28% and 63%. However, the maximum frequency deviations require shorter time to reach a safe frequency margin, and the root mean square values of the frequency oscillations during its recovery are improved compared to the results of the two penetration levels. For example, at 63% penetration, t_{SM} was less than 30 s, and Δf_{RMS} was higher compared to Case studies 2C and 2D. Similarly, the penetration levels in [11] were 20% and 50%. Comparing the obtained results against 20% penetration, it was found that the improvement in Δf_{max} is almost the same. In addition, t_{SM} is better with respect to the corresponding time at 20% penetration,

and almost equivalent at 50%. As a recommendation, the second algorithm is preferred for wind turbines equipped with pitch controllers and at high levels of wind energy penetration. In addition, it is more efficient for wind farms locations that are characterized by low average wind speeds. It is of note that overloading the wind turbine generator proved to be a feasible solution at high wind speeds, because it avoids de-loading at these wind speeds, and hence reduces wasted energy. The dispatching algorithm has improved this method and, and has proved to be an essential part in completing the support process and reducing frequency oscillations. The major inertial droop controller (which manages the number of participating clusters in frequency support) makes the wind farm operation equivalent to conventional generation; however, it slightly mitigates the achievement improvements in frequency recovery. In other words, integrating the second algorithm with the proposed dispatching method provides a reasonable solution for enabling wind farms to contribute positively in the elimination of frequency drops.

This thesis also presents a modified method of estimating a round figure for the upgraded conventional capacity after certain wind farms integration. This method mainly relies on the amount of annual generated energy by a certain wind turbine type according to wind speed chronological data in a concerned location. Results show that the annual energy generation ranges from 35% up to 73% (in very limited locations) of continuous full load generation. Examined locations and wind turbine types reveal that large wind turbines with a wide range of rotational speeds are the best choice for moderate or low wind speed sites. However, medium-sized cheaper wind turbines are acceptable in locations with high average wind speeds. According to the Egyptian case study capacity assessment, thirteen wind farms with 1300 wind turbines from three different manufacturers can replace 20% of conventional generation without the need to use reserves. These numbers are obtained using tough constraints, as the energy production analysis was performed using the top 10% of records of the Egyptian grid's hourly load. However, this number is a round figure, which is highly affected by the matching criterion between wind turbines types and integrated locations. In addition, the worst frequency deviation occurred due to this replacement at standard operation for wind turbines, did not exceed 40 mHz during the hour of peak load record.

The integration of storage banks as an alternative source of power support has also proved to be valid. In particular, the construction of a batteries hangar near the connection point of each wind farm is a practical solution, and it avoids any 'special' algorithm for wind turbine operation. The achieved frequency improvement is almost similar to enhancements achieved in the first and second algorithms, but with better sustainability. In addition, wasted wind energy is reduced to zero in this case but more wind energy is utilized when the batteries are charged. However, the criterion used to decide whether excess wind energy is available to charge the batteries banks is a point of further investigations. In this research work, it is assumed that the conventional generation contribution in the load feed should be in the range of 70% of the total demand, and that the remaining 30% would be covered by wind farms. If the generation from wind farms is higher than the required power to fulfil this requirement, the excess

energy is directed to charge the battery banks. In relation to the applied case study, it is evident that storage banks with an overall rated power of 8.7% (from the nameplate ratings of installed wind farms) clearly improve the frequency response during drops. In general, there are markedly improved achievements in frequency, because maximum drop is alleviated by 150 mHz, with a reduction of 10 s in reaching the safety margin. In addition, it was found that reducing the average participation of conventional generation in the load feed will dramatically reduce the power rating of the required storage banks.

It is possible that future work will investigate the integration of a central pumped-hydro storage facility as an alternative to all battery banks. The presence of several water resources in Egypt, and the suitable geographical nature in some areas, makes it feasible to construct hydro energy storage reservoirs. Thus, the excess wind power could be used to lift the water from the natural resource to a higher level, and the available hydro power could be utilized either for support in frequency events, or to mitigate the intermittent nature of wind power generation. In addition, future work will highlight reliability studies to calculate load interruptions indices at major load points after the replacement of conventional units. The real reliability data of both conventional units and wind turbines will be involved, as well as the precise distribution of economic load categories. It is also possible that the economic impacts of the proposed support algorithms could be examined and compared to a standard maximum power tracking operation and its economical merits. Likewise, the capital and running costs of integrating possible storage mediums would be estimated and compared with the extra financial burdens that will occur due to implementation of the proposed frequency support algorithms.

10. Bibliography

[1] T. Hartkopf, *Lecture notes - Renewable energies*. Darmstadt: Technical University of Darmstadt, 2010.

[2] R. Thresher, M. Robinson, and P. Veers, "To capture the wind," *IEEE power energy Magazine*, vol. 5, no. 6, 2007.

[3] Z. Xu, M. Gordon, M. Lind, and J. Ostergaard, "Towards a danish power system with 50% wind — smart grids activities in Denmark," in *IEEE Power & Energy Society General Meeting*, Lyngby, 2009.

[4] T. Ackermann, *Wind power in power systems*. John Wiley & Sons Ltd, 2005.

[5] T. Burton, D. Sharpe, N. Jenkins, and E. Bossanyi, *Wind energy handbook*. John Wiley & Sons Ltd, 2001.

[6] B. Fox, L. Bryans, D. Flynn, N. Jenckins, and D. Milborrow, *Wind power integration*. IET Power and Energy Series 50, 2007.

[7] G. Michalke, *PhD thesis-Variable speed wind turbines - modeling, control, and impact on power system*. Darmstadt: Darmstadt University of technology, 2008.

[8] S. Engelhardt, I. Erlich, C. Feltes, J. Kretschmann, and F. Shewarega, "Reactive power capability of wind turbines based on doubly fed induction generators," *IEEE Transactions on Energy Conversion*, vol. 26, no. 1, pp. 364-372, 2011.

[9] R. Doherty, et al., "An assessment of the impact of wind generation on system frequency control," *IEEE Transactions on Power Systems*, vol. 25, no. 1, pp. 452-460, 2010.

[10] A. R. Bergen and V. Vittal, *Power system analysis, Second edition*. Prentice Hall, 2000.

[11] L.-R. Chang-Chien, C.-M. Hung, and Y.-C. Yin, "Dynamic reserve allocation for system contingency by DFIG wind farms," *IEEE transactions on Power Systems*, vol. 23, no. 2, pp. 729-736, 2008.

[12] V. Akhmatov, *PhD Thesis- Analysis of dynamic behaviour of electrical power systems with large amounts of wind energy*. Lyngby: Technical University of Denmark, 2003.

[13] M. Tazil, et al., "Three-phase doubly fed induction generators: an overview," *IET Journal of Electric Power Applications*, vol. 4, no. 2, pp. 75-89, 2009.

[14] H. Polinder, S. W. H. De Haan, M. R. Dubois, and J. G. Slootweg, "Basic operation principles and electrical conversion systems of wind turbines," *European power electronics and drives journal*, vol. 15, no. 4, 2005.

[15] L. Y. Pao and K. E. Johnson, "Control of wind turbines," *IEEE Control System magazine*, vol. 31, no. 2, pp. 44-62, 2011.

[16] A. Perdana, *PhD thesis-Dynamic model of wind turbines, a contribution towards the establishment of standardized models of wind turbines for power system stability studies*. Sweden: Chalmers university of technology, 2008.

[17] N. Miller, W. Price, and J. Sanchez-Gasca, "Dynamic modeling of GE 1.5 and 3.6 wind turbine-generators," in *Power Engineering Society General Meeting*, New York, 2003.

[18] A. B. Attya and T. Hartkopf, "Evaluation of wind turbines dynamic model parameters using published manufacturer product data," in *IEEE International Energy Conference and Exhibition*, Florence, 2012.

[19] Y. Zou, M. Elbuluk, and Y. Sozer, "A complete modeling and simulation of induction generator wind power systems," in *IEEE Industry Applications Society Annual Meeting*, Houston, 2010.

[20] A. Grauers, "Efficiency of three wind energy generator systems," *IEEE Transactions on Energy Conversion*, vol. 11, no. 3, pp. 650-657, 1996.

[21] Enercon company, (2011) Enercon wind turbines - product overview. [Online]. http://www.enercon.de/p/downloads/ENERCON_PU_en.pdf

[22] U. S. department of energy, (2012) Documentation, user support, and verification of wind turbine and plant models. [Online]. http://www.osti.gov/bridge/servlets/purl/1051403/.pdf

[23] S. Nishikata and F. Tatsuta, "A new interconnecting method for wind turbine generators in a wind Farm and basic performances of the integrated system," *IEEE Transactions on Industrial Electronics*, vol. 57, no. 2, pp. 468-475, 2010.

[24] M. Jelavić, N. Perić, and I. Petrović, "Damping of wind turbine tower oscillations through rotor speed control," in *International Conference on Ecologic Vehicles & Renewable Energies*, Monaco, 2007.

[25] M. Qian, N. Chen, L. Zhao, D. Zhao, and L. Zhu, "A new pitch control strategy for variable-speed wind generator," in *IEEE Innovative Smart Grid Technologies - Asia*, Tianjin, 2012.

[26] T. Senjyu, et al., "Output power control of wind turbine generator by pitch angle control using minimum variance control," *Wiley library- Electrical engineering in Japan*, vol. 154, no. 2, pp. 10-18.

[27] I. A. Hiskens, "Dynamics of type-3 wind turbine generator models," *IEEE Transactions on Power Systems*, vol. 27, no. 1, pp. 465-474, 2012.

[28] L. Yang, Z. Xu, J. Ostergaard, Z. Y. Dong, and K. P. Wong, "Advanced control strategy of DFIG wind turbines for power system fault ride through," *IEEE Transactions on Power Systems*, vol. 27, no. 2, pp. 713-722, 2012.

[29] S.-B. Lee and K.-B. Lee, "Performance improvement of a DFIG in a wind turbine under an unbalanced grid-voltage condition," in *IEEE International Symposium on Industrial Electronics*, Italy, 2010.

[30] J. Hu and Y. He, "Reinforced control and operation of DFIG-based wind power generation system under unbalanced grid voltage conditions," *IEEE Transactions on Energy Conversion*, vol. 24, no. 4, pp. 905-915, 2009.

[31] D. Xiang, L. Ran, J. R. Bumby, P. J. Tavner, and S. Yang, "Coordinated control of an HVDC link and doubly fed induction generators in a large offshore wind farm," *IEEE Transactions on Power Delivery*, vol. 21, no. 1, pp. 463-471, 2006.

[32] J. F. M. Padron and A. E. F. Lorenzo, "Calculating steady-state operating conditions for doubly-fed induction generator wind turbines," *IEEE Transactions on Power Systems*, vol. 25, no. 2, pp. 922-928, 2010.

[33] Z. J. Meng, "An improved equivalent wind method for the aggregation of DFIG wind turbines," in *IEEE International Conference on Power System Technology*, China, 2010.

[34] S. Li, T. A. Haskew, and S. Mazari, "Integrating electrical and aerodynamic characteristics for DFIG speed control study," in *IEEE Power Systems Conference and Exposition*, Seattle, 2009.

[35] S. M. Muyeen, et al., "Low voltage ride through capability enhancement of wind turbine generator system during network disturbance," *IET Renewable Power Generation*, vol. 3, no. 1, pp. 65-74, 2009.

[36] O. Aluko, T. M. Smith, and L. M. Tolbert, "Behavior of doubly-fed induction generator under nearby wind plant fault," in *IEEE Power and Energy Society General Meeting*, Tennessee, USA, 2010.

[37] N. Joshi and N. Mohan, "A novel scheme to connect wind turbines to the power grid," *IEEE Transactions on Energy Conversion*, vol. 24, no. 2, pp. 504-510, 2009.

[38] J. Hu, et al., "A novel control strategy for doubly fed induction generator and permanent magnet synchronous generator during voltage dips," in *20th Australasian Universities Power Engineering Conference*, Australia, 2010.

[39] A. D. Hansen and G. Michalke, "Fault ride-through capability of DFIG wind turbines," *Elsevier Renewable Energy*, vol. 32, no. 9, p. 1594–1610, 2006.

[40] L. Peng, B. Francois, and Y. Li, "Improved crowbar control strategy of DFIG based wind turbines for grid fault ride-through," in *IEEE 24th Applied Power Electronics Conference and Exposition*, Washington, DC, 2009, pp. 1932-1938.

[41] G. Pannell, D. J. Atkinson, and B. Zahawi, "Minimum-threshold crowbar for a fault-ride-through grid-code-compliant DFIG wind turbine," *IEEE Transactions on Energy Conversion*, vol. 25, no. 3, pp. 750-759, 2010.

[42] R. G. de Almeida and J. A. Peas Lopes, "Participation of doubly fed induction wind generators in system frequency regulation," *IEEE Transactions on Power Systems*, vol. 22, no. 3, pp. 944-950, 2007.

[43] H. Holttinen, et al., "Currents of changes," *IEEE Power and Energy Magazine*, vol. 9, no. 6, pp. 47-59, 2011.

[44] I. R. Unknown, "Dynamic models for steam and hydro turbines in power system studies," *IEEE Transactions on Power Apparatus System*, vol. 92, no. 6, pp. 1904-1915, 1973.

[45] M. Bhuiyan and S. Dinakar, *Master thesis-Comparing and evaluating frequency response characteristics of conventional power plant with wind power plant*. Goteborg: Chalmers University of Technology, 2008.

[46] O. Anaya-Lara, F. M. Hughes, N. Jenkins, and G. Strbac, "Contribution of DFIG-based wind farms to power system short-term frequency regulation," in *IEE Proceedings- Generation, Transmission and Distribution*, Manchester, 2006.

[47] J. Ekanayake and N. Jenkins, "Comparison of the response of doubly fed and fixed-speed induction generator wind turbines to changes in network frequency," *IEEE Transactions on Energy Conversion*, vol. 19, no. 4, pp. 802-812, 2004.

[48] J. Berdy. (2010) Out-of-step protection for generators. [Online]. http://store.gedigitalenergy.com/FAQ/Documents/CEB/GER-3179.pdf

[49] N. Rahmat Ullah, T. Thiringer, and D. Karlsson, "Temporary primary frequency control support by variable speed wind turbines - potenial and applications," *IEEE Transactions on Power Systems*, vol. 23, no. 2, pp. 601-612, 2008.

[50] M. F. M. Arani and E. F. El-Saadany, "Implementing virtual inertia in DFIG-based wind power generation," *IEEE Transactions on Power Systems*, vol. 28, no. 2, pp. 1373-1384, 2012.

[51] D. L. Yao, S. S. Choi, K. J. Tseng, and T. T. Lie, "Determination of short-term power dispatch schedule for a wind farm incorporated with dual-battery energy storage scheme," *IEEE Transactions on Sustainable Energy*, vol. 3, no. 1, pp. 74-84, 2012.

[52] P. Kundur, *Power system stability and control*. 1994: McGraw-Hill Inc., New York.

[53] G. Andersson, *Lecture notes: Dynamics and control of eletrical power systems*. Zurich: ETH Zurich, 2011.

[54] S. Muller, M. Deicke, and W. D. Doncker, "Double fed induction generator for wind turbine systems," *IEEE Industry Applications Magazine*, vol. 8, no. 3, pp. 26-33, 2002.

[55] W. Leonhard, *Control of electrical drives*, 3rd ed. Springer , 2001.

[56] T. R. Ayodele, A. A. Jimoh, J. L. Munda, and J. T. Agee, "Impact of variation of wind speed in a wind integrated power system," in *International Conference on Advances in Energy Engineering (ICAEE)*, Tshwane, South Africa, 2010.

[57] S.-J. Huang and H.-H. Wan, "Enhancement of matching turbine generators with wind regime using capacity factor curves strategy," *IEEE Transactions on Energy Conversion*, vol. 24, no. 2, pp. 551-553, 2009.

[58] A. Kusiak and Z. Zhang, "Short-horizon prediction of wind power: A data-driven approach," *IEEE Transactions on Energy Conversion*, vol. 25, no. 4, pp. 1112-1122, 2010.

[59] A. Kusiak, H. Zheng, and Z. Song, "Short-term prediction of wind farm power: a data mining approach," *IEEE Transactions on Energy Conversion*, vol. 24, no. 1, pp. 125-136, 2009.

[60] M. Narayana, G. Putrus, M. Jovanovic, and P. S. Leung, "Predictive control of wind turbines by considering wind speed forecasting techniques ," in *44th International Universities Power Engineering Conference*, Glasgow, 2009 .

[61] P. Clemow, T. C. Green, and C. A. Hernandez-Aramburo, "Wind farm output smoothing through co-ordinated control and short-term wind speed prediction," in *IEEE Power and Energy Society General Meeting*, London, 2010.

[62] R. J. Barthelmie and L. E. Jensen, "Evaluation of wind farm efficiency and wind turbine wakes at the nysted offshore wind farm," *Willey wind energy journal*, vol. 13, no. 6, p. 573–586, 2010.

[63] M. Magnusson and A. .-S. Smedman, "Air flow behind wind turbines," *Wind Engineering and*

Industrial Aerodynamics, vol. 80, no. 1-2, pp. 169-189, 1999.

[64] L. M. Frenandez, C. A. Garcia, J. R. Saenz, and F. Jurado, "Equivalent models of wind farms by using aggregated wind turbines and equivalent winds," *Elsevier Journal of Energy Conversion and Management*, vol. 50, no. 3, pp. 691-704, 2009.

[65] M. Ali, I. .-S. Ilie, J. V. Milanovic, and G. Chicco, "Wind farm model aggregation using probabilistic clustering," *IEEE Transactions on Power Systems*, vol. 28, no. 1, pp. 309-316, 2012.

[66] B. P. Hayes, I. Ilie, A. Porpodas, S. Z. Djokic, and G. Chicco, "Equivalent power curve model of a wind farm based on field measurement data," in *IEEE PowerTech*, Trondheim, 2011.

[67] M. Ali, J. Matevosyan, J. V. Milanović, and L. Söder, "Effect of wake consideration on estimated cost of wind energy curtailments," in *8th Int. Workshop Large-Scale Integration of Wind Power into Power Systems and on Transmission Networks for Offshore Wind Farms*, Bremen, 2009.

[68] J. Ekanayake, K. Liyanage, J. Wu, A. Yokoyama, and N. Jenkins, *Smart grid: technology and applications*. New Delhi, India.: John Wiley & Sons, 2012.

[69] X. Liu and W. Xu, "Economic load dispatch constrained by wind power availability: A here-and-now approach," *IEEE Transactions on Sustainable Energy*, vol. 1, no. 1, pp. 2-9, 2010.

[70] L. Li, Q. Ding, H. Li, and M. Dan, " Optimal dispatching method for smoothing power fluctuations of the wind-photovoltaic-battery hybrid generation system ," in *IEEE Asia Innovative Smart Grid Technologies*, Tianjin, 2012.

[71] A. B. Attya and T. Hartkopf, "Penetration impact of wind farms equipped with frequency variations ride through algorithm on power system frequency response," *International Journal of Electrical Power and Energy Systems*, vol. 40, no. 1, pp. 94-103, 2012.

[72] J. A. Martinez, "Modeling and characterization of energy storage devices," in *IEEE Power and Energy Society general meeting*, San Diego, 2011.

[73] T. K. A. Brekken, et al., "Optimal energy storage sizing and control for wind power applications," *IEEE Transactions on Sustainable Energy*, vol. 2, no. 1, pp. 69-77, 2011.

[74] B. Hartmann and A. Dan, "Cooperation of a grid-connected wind farm and an energy storage unit — demonstration of a simulation tool," *IEEE Transactions on Sustainable Energy*, vol. 3, no. 1, pp. 49-56, 2012.

[75] S. Teleke, M. E. Baran, A. Q. Huang, S. Bhattacharya, and L. Anderson, "Control strategies for battery energy storage for wind farm dispatching," *IEEE Transactions on Sustainable Energy*, vol. 3, no. 2009, pp. 725-732, 2009.

[76] S. Teleke, M. E. Baran, A. Q. Huang, and S. Bhattacharya, "Rule-based control of battery energy storage for dispatching intermittent renewable sources," *IEEE Transactions on Sustainable Energy*, vol. 1, no. 3, pp. 117-124, 2010.

[77] D. L. Yao, S. S. Choi, K. J. Tseng, and T. T. Lie, "A statistical approach to the design of a dispatchable wind power-battery energy storage system," *IEEE Transactions on Energy Conversion*, vol. 24, no. 4, pp. 916-925, 2009.

[78] D. Gautam, V. Vittal, and T. Harbour, "Impact of increased penetration of DFIG-based wind turbine generators on transient and small signal stability of power systems," *IEEE transactions on Power Systems*, vol. 24, no. 3, pp. 1426-1434, 2009.

[79] C.-C. Le-Ren and Y. Yao-Ching, "Strategies for operating wind power in a similar manner of conventional power plant," *IEEE transactions on energy conversion*, vol. 24, no. 4, pp. 926-934, 2009.

[80] P.-K. Keung, L. Pei, H. Banakar, and O. Boon Teck, "Kinetic energy of wind-turbine generators for system frequency support," *IEEE transactions on Power Systems*, vol. 24, no. 1, pp. 279-287, 2009.

[81] G. C. Tarnowski, P. C. Kjar, P. E. Sorensen, and J. Ostergaard, "Variable speed wind turbines capability for temporary over-production," in *Proceedings of IEEE Power & Energy Society General Meeting*, USA, 2009.

[82] M. Kayikci and J. V. Milanovic, "Dynamic contribution of DFIG-based wind plants to system frequency disturbances," *IEEE transactions on Power Systems*, vol. 24, no. 2, pp. 859-867, 2009.

[83] I. W. G. R. Unknown, "Hydraulic turbine and turbine control models for system dynamic studies," *IEEE Transactions on Power Systems*, vol. 7, no. 1, pp. 167-179, 1992.

[84] H. Emam Shalan, M. A. Moustafa Hassan, and A. B. G. Bahgat, "Parameter estimation and dynamic simulation of gas turbine model in combined cycle power plants based on actual operational data," *Journal of American Science*, vol. 7, no. 5, pp. 303-310, 2011.

[85] N. Jaleeli, D. N. Ewart, and L. H. Fink, "Understanding automatic generation control," *IEEE Transactions on Power Systems*, vol. 7, no. 3, pp. 1106-1122, 1992.

[86] A. B. Attya, Y. G. Hegazy, and M. A. Mostafa, "Evaluation of system reliability using seasonal and random operation techniques," in *IEEE Power Engineering Society General Meeting*, Pittsburgh, 2008.

[87] A. B. Attya and T. Hartkopf, "Generation of High Resolution Wind Speeds and Wind Speed Arrays inside a Wind Farm based on Real Site Data," in *IEEE 11th conference on electrical power quality and utilization*, Lisbon, 2011.

[88] N. Moskalenko, K. Rudion, and A. Orths, "Study of wake effects for offshore wind farm," in *Modern Electric Power Systems*, Wroclaw, Poland, 2010.

[89] P. Frohboese and C. Schmuck, "Thrust coefficients used for estimation of wake effects of fatigue load calculation," in *Proceedings of European Wind Energy Conference*, Warsaw, Poland, 2010.

[90] A. Keane, et al., "Capacity value of wind power," *IEEE Transactions on Power Systems*, vol. 26, no. 2, pp. 564-572, 2011.

[91] I. A. Gowaid, A. El-Zawawi, and M. El-Gammal, "Improved inertia and frequency support from grid-connected DFIG wind farms," in *IEEE Power Systems Conference and Exposition*, USA, 2011.

[92] M. Faridi, R. Ansari, S. A. Mousavi, and M. Dodman, "Pitch control of wind turbine blades in noisy and unstable wind conditions," in *International Conference on Environment and Electrical Engineering*, Iran, 2010.

[93] UCTE, *Appendix 1 —load-frequency control and performance*. The Union of the coordination of the transmission of electricity, 2002.

[94] Gameza company, (2011) Brochure of wind turbine: G-90-2.0 MW. [Online]. http://iberdrolarenewables.us/roaringbrook/DEIS_Appendices/Appendix-A-Component-Specs-and-Construction-Info/2-Gamesa_Eolica_G90.pdf

[95] Nordex company. (2011) Brochure of wind turbine: Nordex 117- 2400 kW. [Online]. http://www.nordex-online.com/en/produkte-service/wind-turbines/n117-24-mw.html

[96] R. M. G. Castro and A. F. M. Ferreira, "A comparison between chronological and probabilistic method to estimate wind power capacity credit," *IEEE Transactions on Power Systems*, vol. 16, no. 4, p. 904–909, 2001.

[97] Egyptian ministry of electricity and and energy, "Annual energy and power generation report," 2010.

[98] N. G. Mortensen and U. S. Said, "Wind Atlas for Egypt," 2009.

[99] Q. Li, S. S. Choi, Y. Yuan, and D. L. Yao, "On the determination of battery energy storage capacity and short-term power dispatch of a wind farm," *IEEE Transactions on Sustainable Energy*, vol. 2, no. 2, pp. 148-158, 2011.

[100] Trojan Batteries company (2012) Energy storage solutions for renewable energy series manual.

[101] M. Ceraolo, "New dynamical models of lead-acid batteries," *IEEE Transactions on Power Systems*, vol. 15, no. 4, pp. 1184-1190, 2000.

[102] L. Ruttledge, N. W. Miller, J. O'Sullivan, and D. Flynn, "Frequency response of power systems with variable speed wind turbines," *IEEE transactions on Sustainable Energy*, vol. 3, no. 4, pp. 683-691, 2012.

[103] I. Kamwa, D. Lefebvre, and L. Loud, "Small signal analysis of hydro-turbine governors in large interconnected power plants," in *IEEE Power Engineering Society Winter Meeting*, Varennes, Canada, 2002.

11. Appendix

11.1. List of figures

11.2. List of tables

11.3. List of abbreviations

AGC	Automatic Generation Control
DFIG	Double Fed Induction Generator
DOD	Depth Of Discharge
DOIG	Doubly Outage Induction Generator
E-101	Enercon 101 m, 3.05 MW wind turbine
FDRT	Frequency Drop Ride Through
FoR	Facilitation of Renewables
G-90	Gameza 90 m, 2 MW wind turbine
GE-77	General Electric 77 m, 1.5 MW wind turbine
KE	Kinetic Energy
LVRT	Low Voltage Ride Through
MPT	Maximum Power Tracking
N-117	Nordex 117 m, 2.5 MW wind turbine
pu	per unit
PCC	Point of Common Coupling
PEC	Power Electronics Converter
PI	Proportional Integral
PQ	active-reactive powers bus
PV	active power-voltage bus
ROCOF	Rate of Change of Frequency
SB	Storage Bank
SCIG	Squirrel Cage Induction Generator
SOC	State Of Charge
SOs	System Operators
WF	Wind Farm
WT	Wind Turbine
WTG	Wind Turbine Generator
WS	Wind Speed

11.4. Nomenclature

ρ	Air density	Kg/m^3
Δf	System frequency deviation	Hz or pu
Δf_{10s}	Frequency deviation after 10 s from frequency event initiation	Hz
Δf_{max}	Maximum frequency deviation during a frequency event	Hz
$\Delta f_{improved}$	Improved frequency deviation due to WFs support	Hz or pu
$\Delta KE_{available}$	Available KE stored in WT rotating parts	Joule
$\Delta KE_{required}$	Required KE to recover the system nominal frequency	Joule
ΔP_{ch}	Charging power step for a storage bank	MW
ΔPC_{total}	Average charging power rating for all installed storage banks	MW
ΔP_{disch}	Supportive power step during frequency drop by a storage bank	MW
$\Delta P_{WFs\ total}$	Power support provided by all WFs	Pu
$\Delta \omega$	Deviation in rotational speed	Pu
A	Wind turbine rotor swept area	m2
CGC	Conventional generation contribution	dimensionless
C_F	Certainty factor integrated in *Method 1*	dimensionless
CC_{new}	New conventional power capacity after wind energy integration	MW
CN_i	number of batteries cells in storage bank (*i*)	dimensionless
C_p	Coefficient of performance of a WT	dimensionless
$C_{p\text{-}optimum}$	Optimum coefficient of performance	dimensionless
D	Wind turbine rotor diameter	M
D_F	WT output power de-loading factor	dimensionless
D_{row}	Distance between two successive WTs rows inside a WF	M
E_{MPT1}, E_{MPT2}	Generated energies within time span (T) when WT operates based on MPT1 and MPT2 respectively	GWh
E_{OS}, $E_{D,}$ E_{PD}	Generated energies when WT operates using over-speeding, de-loaded and partial de-loaded strategies respectively	GWh
f_o	Power system nominal frequency	Hz
H	System inertia	seconds
H_G	Certain generator inertia	seconds
H_{WT}	Wind turbine inertia	seconds
J_{WT}	Wind turbine lumped moment of inertia	kg m^2
K	Number of WSs events which exist during certain load level	dimensionless
K_{Droop}, $K_{Inertia}$	Droop and inertial gain constants in *Dispatching method*	dimensionless
KE_{base}	Power system base kinetic energy	kWh
k_w	Ground roughness used to calculate wake effect	dimensionless

$Load_{inst.}$	instantaneous load demand	MW
M	Special parameter used in *Method 1* to switch between fixed and dynamic frequency support	dimensionless
m	number of wind turbines of the same type inside wind farm	dimensionless
Ni_c	Number of clusters inside a wind farm	dimensionless
Ni_{pc}	Number of participating clusters in power support in a WF (i)	dimensionless
N_L	Number of considered load points in WF production assessment method	dimensionless
N_p	Number of points in output power array at WS record (k)	dimensionless
N_{WT}	Number of WTs inside a WF	dimensionless
P_B	base WT output power at base WS	Per unit
PWT_e	Wind turbine generator output electrical power	W or pu
PWT_m	Wind turbine mechanical power	W or pu
PWT_r	Wind turbine rated output power	W or pu
R	Wind turbine rotor radius	m
S_b	Power system base apparent power	VA
SCFi	Storage contribution factor of storage bank (i)	dimensionless
$Slope_{WT}$	Slope of WT speed recovery	rad /sec^2
S_{WFi}	Aggregate rated output power of WF number 'i'	MW
s_R	Support ratio in *Method 2*	dimensionless
t_{delay}	Time required by wind stream to travel from one row to the next	seconds
t_f	Time frame within which N_{ipc} value is periodically updated	seconds
t_{OL}	Allowed WT generator overloading duration in *Method 2*	seconds
t_R	Wind turbine default speed recovery time	seconds
t_s	Support time in *Method 1*	seconds
t_{SB}	Support time of a storage bank	seconds
t_{SM}	Time required by the system to reach frequency safe margin	seconds
t_{start}, t_{end}	start and end instants of frequency support phase in *Method 2*	seconds
t_{WS}	Time span between each two successive records in a WS array	seconds
TWT_e	Wind turbine electrical torque	pu or N.m
TWT_m	Wind turbine mechanical torque	pu or N.m
V_{ci}, I_{ci}	Rated voltage and current of single cell in battery bank (i)	V and A
WFi_{weight}	Wind farm contribution ratio in support power	dimensionless
WFs_{total}	All installed wind farms contributions' ratios	dimensionless
$WS(x)$	Wind velocity in the wake at distance x	m/s
WS_B	Base wind speed in *Method 2*	m/s

WS_{CI}	Wind turbine cut-in wind speed	m/s
WS_{CO}	Wind turbine cut-out wind speed	m/s
WS_{high}	high WS limit in *Method 2*	m/s
WSi_{avg}	Average wind speed in location no. (*i*)	m/s
WSi	Free stream wind speed magnitude in location no. (*i*)	m/s
WSi_{rated}	Rated wind speed of wind turbine installed in wind farm (*i*)	m/s
WS_{low}	low WS limit in Method 2	m/s
WS_o	Free stream wind speed	m/s
WS_R	Wind turbine rated wind Speed	m/s
WTi_{rating}	Rated power of wind turbine installed in wind farm (*i*)	MW
β	Rotor blade pitch angle	degree
λ	Tip speed ratio	dimensionless
λ_H	High tip speed ratio in *Method 1*	dimensionless
λ_L	Low tip speed ratio in *Method 1*	dimensionless
λ_{min}	Lowest allowed tip speed ratio in *Method 1*	dimensionless
ω_b	Base rotational speed	pu or rad/s
$\omega_{pu\text{-}stop}$	Threshold 'stop' rotational speed in *Method 2*	pu or rad/s

11.5. Method 1 mathematical derivations

Generally, for any power system [**10**,**52**]: required KE to remove a frequency deviation equals the system base KE (KE_{base}) multiplied by $\frac{f_o^2 - f^2}{f_o^2}$.

$$\therefore\ \Delta KE_{required} = KE_{base} \cdot \left[1 - \left(\frac{f_o + \Delta f}{f_o}\right)^2\right],\ \ \Delta f_{improved} = f_{improved} - f_o \tag{11.1}$$

$$\Delta KE_{new} = \Delta KE_{required} - \Delta KE_{available} \tag{11.2}$$

$$\Delta KE_{available} = 0.5 \cdot J_{WT} \cdot \frac{1}{R^2}\left(\lambda_H^2 - \lambda_L^2\right) \cdot WS^2 \tag{11.3}$$

$$KE_{base} = H \cdot S_b \tag{11.4}$$

Note that, H, S_b and f_o are fixed parameters for the investigated power system

Using (11.3) substituting by $\Delta f = \Delta f_{improved}$ at $\Delta KE_{new} = \Delta KE_{required}$ ($\Delta f_{improved}$),

$$\Delta KE_{new} = KE_{base} \cdot \left[1 - \left(\frac{f_o + \Delta f_{improved}}{f_o}\right)^2\right] \tag{11.5}$$

Substitute (11.1), (11.3) and (11.5) in (11.2)

$$\text{hence, } \left(\frac{f_o + \Delta f_{improved}}{f_o}\right)^2 = \frac{\Delta KE_{available}}{KE_{base}} + \left(\frac{f_o + \Delta f}{f_o}\right)^2 \tag{11.6}$$

$$\text{hence, } \Delta f_{improved} = f_o \cdot \sqrt{\frac{\Delta KE_{available}}{KE_{base}} + \left(\frac{f_o + \Delta f}{f_o}\right)^2} - f_o \tag{11.7}$$

Evaluating λ_L value at each frequency drop depends on WS instantaneous value. However, it is expected that the whole available KE from WFs is always insufficient to cover the required KE by the system to eliminate the existing frequency deviation. Hence, it may be said that ‘M’ is a proportionality factor between the available and required KEs as in (11.8)

$$\Delta KE_{available} = M \cdot \Delta KE_{required} \tag{11.8}$$

Substituting by (11.1), (11.4) and (11.5) in (11.8) taking into consideration total number of installed WTs (N_{WT}):

$$\lambda_L = \sqrt{\lambda_H^2 + \frac{2 \cdot M \cdot H \cdot S_b \cdot R^2}{J_{WT} \cdot WS^2 \cdot N_{WT}} \cdot \left[\frac{2\Delta f}{f_o} + \frac{\Delta f^2}{f_o^2} \right]} \qquad (11.9)$$

$$\lambda_H = 1.15 \cdot \lambda_{optimum}$$

Note that, R and J_{WT} are fixed parameters for each integrated WT meanwhile N_{WT} is fixed for each WF for the same WT type.

Previous equation can be used to calculate λ_{min} by setting Δf to its maximum allowed value (Δf_{max}) (i.e., when Δf exceeds this threshold WT doesn't participate in frequency deviation elimination). However, WT minimum rotational speed (ω_{min}) indicated in its specifications is considered so that applying λ_{min} does not violate it, therefore 'M_{min}' is calculated at minimum allowed WS and at ω_{min} using (11.10). In conclusion, in case of Δf_{max} WT injects the full allowed amount of KE without reducing rotational speed beyond the minimum limit. Taking into consideration in all presented equations that Δf must have certain sign not just an absolute value.

Substitute by Δf_{max} in (11.10) to estimate 'M' minimum value at certain WS:

$$M_{min} = WS_{min}^2 \cdot \frac{\left(\left(\frac{\omega_{min} \cdot R}{WS_{min}} \right)^2 - \lambda_H^2 \right) \cdot J_{WT} \cdot N_{WT}}{2H \cdot S_b \cdot R^2} \cdot \frac{1}{\frac{2 \cdot \Delta f_{max}}{f_o} + \left(\frac{\Delta f_{max}}{f_o} \right)^2} \qquad (11.10)$$

The SI dimensions check for parameter 'M' evaluated using (3.4) is as follows:

$$M = m^2 \cdot s^{-2} \cdot \frac{(\text{dimensionless}) \cdot kg \cdot m^2}{s \cdot (m^2 \cdot kg \cdot s^{-3}) \cdot m^2} \cdot \frac{1}{\frac{s^{-1}}{s^{-1}} + \left(\frac{s^{-1}}{s^{-1}} \right)^2} = \text{dimensionless}$$

The AGC block is described by (11.11) while the load static and dynamic responses are represented by Figure A.2:

$$\Delta P_{AGC} = -B \cdot C_{pAGC} \cdot \Delta f - \frac{1}{t_n} \int (P_{gen.} - P_{load} + K \cdot \Delta f)\, dt \qquad (11.11)$$

11.6. Tables

Table A.1 WTs types major specifications

WT type	GE-77	G-90	E-101	N-117
Manufacturer	General Electric	Gameza	Enercon	Nordex
Rotor diameter, m	77	90	101	117
Cut-in WS, m/s	3.5	3	3	3
Cut-out WS, m/s	25	21	28	20
Default rated WS, m/s	13	16	13	11
Nameplate rating, MW	1.5	2	3.05	2.4
Rotational speed range, rad/ s	1.15 - 2.51	0.94 - 1.99	0.67 - 2.31	1.19 - 2.1
Optimum tip speed ratio	8.1	10	10.4	8

Table A.2 N-117 Model parameters

a	b	c_1	c_2	c_3	c_4	c_5	c_6
0.142	0.03277	0.51	92.7	0.4582	5	31.79	0.03886

Table A.3 E-101 Model parameters

a	b	c_1	c_2	c_3	c_4	c_5	c_6
0.09394	0.04562	0.51	94.05	0.5245	5	23.69	0.03991

Table A.4 G-90 Model parameters

a	b	c_1	c_2	c_3	c_4	c_5	c_6
0.1536	0.0388	0.51	100.5	0.4828	5	34.44	0.03979

Table A.5 Wind speeds categories

Cat.	1	2	3	4	5	6
WS ranges	WS $\leq$ 4	4 < WS $\leq$ 6	6 < WS $\leq$ 8	8 < WS $\leq$ 10	10 < W S $\leq$ 12	WS > 12

Table A.6 WSs characteristics in all considered locations (Average, Max and Min are in m/s, while Categories are in percentages of occurrence per one year)

Nabq									
Corruption	Average	Max	Min	Cat. 1	Cat. 2	Cat. 3	Cat. 4	Cat. 5	Cat. 6
2.07	6.85	18.42	0.19	25.27	22.54	15.12	14.13	13.30	9.64
Dakhla									
Corruption	Average	Max	Min	Cat. 1	Cat. 2	Cat. 3	Cat. 4	Cat. 5	Cat. 6
18.53	6.26	15.52	0.19	18.93	24.37	33.42	17.81	4.55	0.93
Galala									
Corruption	Average	Max	Min	Cat. 1	Cat. 2	Cat. 3	Cat. 4	Cat. 5	Cat. 6
0.04	5.99	20.35	0.18	20.53	33.85	26.68	12.74	4.35	1.86
Hekma									
Corruption	Average	Max	Min	Cat. 1	Cat. 2	Cat. 3	Cat. 4	Cat. 5	Cat. 6
0.08	6.51	20.24	0.19	17.71	30.02	26.27	15.08	6.45	4.45
Mathany									
Corruption	Average	Max	Min	Cat. 1	Cat. 2	Cat. 3	Cat. 4	Cat. 5	Cat. 6
0.37	5.75	22.56	0.19	23.94	34.12	25.65	10.77	3.72	1.80
Port Said									
Corruption	Average	Max	Min	Cat. 1	Cat. 2	Cat. 3	Cat. 4	Cat. 5	Cat. 6
33.72	4.80	15.18	0.18	36.95	38.25	17.49	5.62	1.38	0.31
Kossier									
Corruption	Average	Max	Min	Cat. 1	Cat. 2	Cat. 3	Cat. 4	Cat. 5	Cat. 6
2.91	5.53	16.61	0.20	30.60	27.04	22.33	13.69	5.10	1.23

Nuweiba									
Corruption	Average	Max	Min	Cat. 1	Cat. 2	Cat. 3	Cat. 4	Cat. 5	Cat. 6
18.98	5.51	16.26	0.24	24.92	35.86	25.65	10.79	2.32	0.46
Dara									
Corruption	Average	Max	Min	Cat. 1	Cat. 2	Cat. 3	Cat. 4	Cat. 5	Cat. 6
5.24	8.21	19.22	0.19	14.33	12.67	17.29	24.24	17.49	13.99
Ras Sedr									
Corruption	Average	Max	Min	Cat. 1	Cat. 2	Cat. 3	Cat. 4	Cat. 5	Cat. 6
13.41	7.40	17.33	0.18	13.95	17.07	25.53	24.71	13.40	5.34
Ras Ghareb									
Corruption	Average	Max	Min	Cat. 1	Cat. 2	Cat. 3	Cat. 4	Cat. 5	Cat. 6
6.06	9.77	20.14	0.16	7.29	7.78	13.39	21.42	22.43	27.70
NW									
Corruption	Average	Max	Min	Cat. 1	Cat. 2	Cat. 3	Cat. 4	Cat. 5	Cat. 6
13.63	10.00	21.95	0.19	8.40	9.68	13.29	14.75	18.84	35.04
St. Paul									
Corruption	Average	Max	Min	Cat. 1	Cat. 2	Cat. 3	Cat. 4	Cat. 5	Cat. 6
5.92	8.25	17.83	0.18	14.35	13.23	16.56	22.19	19.32	14.35

Table A. 7 Adjustments of WS_b and ω_b in several locations

Site	**Abu Dara** (8.21)		
WT type	E101	G90	N117
ω_b	1.25	1.6	1.38
WS_{low}	5.6	5.88	4.76
WS_{high}	16.20	17.01	13.77
WS_b	10	10.5	8.50

Dakhla (6.26)		
E101	G90	N117
0.95	1.35	1.05
7.84	6.44	5.32
22.68	18.63	15.39
14	11.5	9.5

El-Galala (6)		
E101	G90	N117
0.9	1.3	1
8.4	7.84	4.76
24.30	22.68	13.77
15	14	8.5

Site	**El-Mathany** (5.75)		
WT type	E101	G90	N117
ω_b	0.9	1.3	1
WS_{low}	8.4	7.84	4.76
WS_{high}	24.30	22.68	13.77
WS_b	15	14	8.5

Kossier (5.53)		
E101	G90	N117
0.9	1.2	0.95
8.4	7.28	5.6
24.30	21.06	16.20
15	13	10

Nabq (6.85)		
E101	G90	N117
1.05	1.5	1.15
6.72	5.88	4.9
19.44	17.01	14.18
12.00	10.5	8.75

Site	**Nuweiba** (5.52)		
WT type	E101	G90	N117
ω_b	0.9	1.24	0.95
WS_{low}	8.4	7.56	5.6
WS_{high}	24.30	21.87	16.20
WS_b	15	13.5	10

Ras Elhekma (6.52)		
E101	G90	N117
1	1.45	1.1
7.28	6.16	5.04
21.06	17.82	14.58
13	11	9

Ras Ghareb (9.77)		
E101	G90	N117
1.4	1.7	1.38
5.46	5.6	4.76
15.80	16.20	13.77
9.75	10.00	8.5

Site	**Ras Sedr** (7.4)		
WT type	E101	G90	N117
ω_b	1.15	1.7	1.25
WS_{low}	6.16	5.88	4.76
WS_{high}	17.82	17.01	13.77
WS_b	11	10.5	8.5

Port Said (4.8)		
E101	G90	N117
0.85	1.05	0.9
8.96	7.84	6.16
24.00	22.68	17.82
16	14.00	11.00

St. Paul (8.25)		
E101	G90	N117
1.25	1.84	1.4
5.6	5.6	4.76
16.20	16.20	13.77
10	10	8.50

Note: the highlighted values represent the amounts of energy in GWh; meanwhile the other values represent the energy efficiency in %.

Table A.8 Harvested energy in all locations according to the algorithm proposed in Chapter 4

Location	Dara			Dakhla			El-Galala		
Season	E101	G90	N117	E101	G90	N117	E101	G90	N117
Winter	4.2	3	4.1	1.5	1.2	2.1	1.1	0.8	1.4
	63.29	67.80	78.46	22.28	26.64	40.80	15.87	18.20	27.07
Spring	1.7	1.3	2.1	1.7	1.4	2.5	1.1	0.8	1.4
	25.10	29.18	39.06	25.24	32.58	47.63	15.89	18.60	27.06
Summer	3.1	2.2	3.1	1.1	0.8	1.5	1.6	1.3	2.2
	46.67	50.26	59.50	16.37	19.22	29.03	24.47	28.82	40.96
Fall	3.7	2.6	3.6	1.2	0.9	16.4	1.3	0.9	1.6
	54.98	58.70	68.25	17.29	20.94	31.22	18.73	21.42	30.94
Annual	12.7	9	12.9	5.4	4.4	7.8	5	3.8	6.6
	47.51	51.49	61.32	**20.29**	24.85	37.17	18.74	21.76	**31.51**

Location	El-Mathany			Kossier			Nabq		
Season	E101	G90	N117	E101	G90	N117	E101	G90	N117
Winter	0.9	0.7	1.1	1.2	1	1.7	2.4	1.7	2.5
	13.37	15.24	21.32	18.48	21.71	33.18	35.72	38.49	47.12
Spring	1	0.7	1.3	1.2	1	1.7	2	1.4	2.1
	14.47	15.74	24.26	18.39	22.87	32.69	29.20	32.04	39.55
Summer	1.6	1.2	2.1	1.2	0.9	1.7	1.8	1.3	1.8
	24.03	27.98	40.53	17.29	20.39	31.84	26.28	28.60	35.15
Fall	1.1	0.8	1.5	0.8	0.6	1.1	2.8	1.9	2.6
	15.78	18.63	28.50	12.09	13.96	20.73	42.16	43.82	49.72
Annual	4.5	3.4	6	4.4	0.3	6.2	8.9	6.3	9
	16.91	**19.40**	28.65	16.56	19.73	**29.61**	**33.34**	35.74	42.88

Location	Nuweiba			Ras Elhekma			Ras Ghareb		
Season	E101	G90	N117	E101	G90	N117	E101	G90	N117
Winter	0.9	0.6	1.6	1.3	1	1.7	5.5	3.7	4.8
	13.39	14.69	31.22	20.19	23.01	32.74	82.53	84.53	92.21
Spring	0.9	0.7	1.2	1.4	0.9	1.6	4.7	3.2	4.3
	14.01	15.28	23.10	20.29	21.74	30.32	70.15	73.27	81.36
Summer	1	0.7	1.4	2.5	1.8	2.7	2.7	1.9	2.9
	15.54	17.06	27.02	37.69	40.97	50.75	39.90	44.42	55.63
Fall	1.2	0.9	1.7	1.6	1.1	1.9	4.2	2.9	3.9
	17.52	19.98	31.53	23.74	26.12	35.21	63.47	65.82	73.49
Annual	4	0.3	5.9	6.8	4.9	7.8	1.7	1.2	1.6
	15.11	16.75	**28.22**	25.48	**27.96**	37.26	64.01	**67.01**	75.67

Location	Ras Sedr			Port Said			Saint Paul		
Season	E101	G90	N117	E101	G90	N117	E101	G90	N117
Winter	3.5	2.5	3.8	0.6	0.4	0.7	4	2.9	4
	53.10	57.89	71.41	8.88	9.13	13.91	60.44	65.54	77.02
Spring	2.6	1.9	2.9	0.6	0.4	0.7	3.8	2.7	3.7
	39.33	43.28	55.10	8.53	8.98	13.89	57.00	61.14	70.95
Summer	1.2	0.9	1.6	0.7	0.5	1	1.7	1.2	1.9
	17.59	20.29	30.30	10.98	11.51	18.71	25.45	28.48	36.18
Fall	2.6	1.9	2.8	0.8	0.6	0.1	3.4	2.3	3.2
	39.35	42.77	53.48	12.34	12.99	21.02	50.16	53.30	61.38
Annual	10	7.2	1.1	2.7	1.9	3.5	12.9	9.1	12.9
	37.34	41.06	**52.57**	10.18	10.65	**16.88**	48.26	52.11	**61.38**

Location	ZT NW		
Season	E101	G90	N117
Winter	5.8	3.9	4.9
	87.27	88.13	93.97
Spring	4.6	3.1	4.1
	68.66	70.97	78.15
Summer	2.3	1.7	2.5
	34.08	37.78	47.72
Fall	4.4	2.9	3.9
	65.42	66.81	73.44
Annual	17.1	11.5	15.4
	63.86	65.92	73.32

Note: the highlighted values represent the amounts of energy in GWh; meanwhile the other values represent the energy efficiency in %.

Table A.9 Implemented governors' parameters values

Steam turbine double reheat	
Parameter	value
T_{ch}	0.25 s
T_{co}	0.4 s
T_{rh1}	7.5 s
T_{rh2}	7.5 s
F_{hp}	0.22
F_{ip}	0.3
F_{vhp}	0.22
F_{lp}	0.26

Steam turbine single reheat	
Parameter	value
T_{ch}	0.25 s
T_{co}	0.4 s
T_{rh1}	7.5 s
T_{rh2}	7.5 s
T_{sr}	0.1 s
F_{hp}	0.22
F_{ip}	0.3
F_{vhp}	0.22
F_{lp}	0.26

Table A.10 Implemented governors' parameters values

Steam governor	
Parameter	value
T_1	2.8 s
T_2	5 s
T_3	0.15 s
Valve rate limits	
Increasing	0.2 pu
Decreasing	-1 pu
Valve opening	
Max	1
Min	0

Hydro mechanical governor	
Parameter	value
∂	0.2 s
T_g	0.2 s
T_p	0.045 s
Gate rate limits	
Increasing	0.2 pu
Decreasing	-0.2 pu
Gate opening	
Max	1
Min	0

Table A.11 Implemented governors' parameters values

Hydro Woodward PID governor	
Parameter	value
K_a	1
K_d	1.5
K_p	3.2
K_{sm}	4
T_c	0.1 s
T_d	0.02 s
Gate rate limits	
Increasing	0.1 pu
Decreasing	-0.1 pu
Gate opening limits	
Max	0.95
Min	0

Hydro electronic governor	
Parameter	value
K_a	5
K_d	0.8
T_a	0.05 s
T_d	0.2 s
T_w	0.55 s
beta	0.5
Gate rate limits	
Increasing	0.1 pu
Decreasing	-0.1 pu
Gate opening	
Max	0.95
Min	0

Table A.12 Load model and AGC parameters

Load model	
Parameter	value
D_l (static load component)	1/200 Hz/MW
W_o (Dynamic load component)	100 MW/Hz

AGC	
Parameter	value
C_{pAGC}	0.17
T_n	120
K	8

11.7. Figures

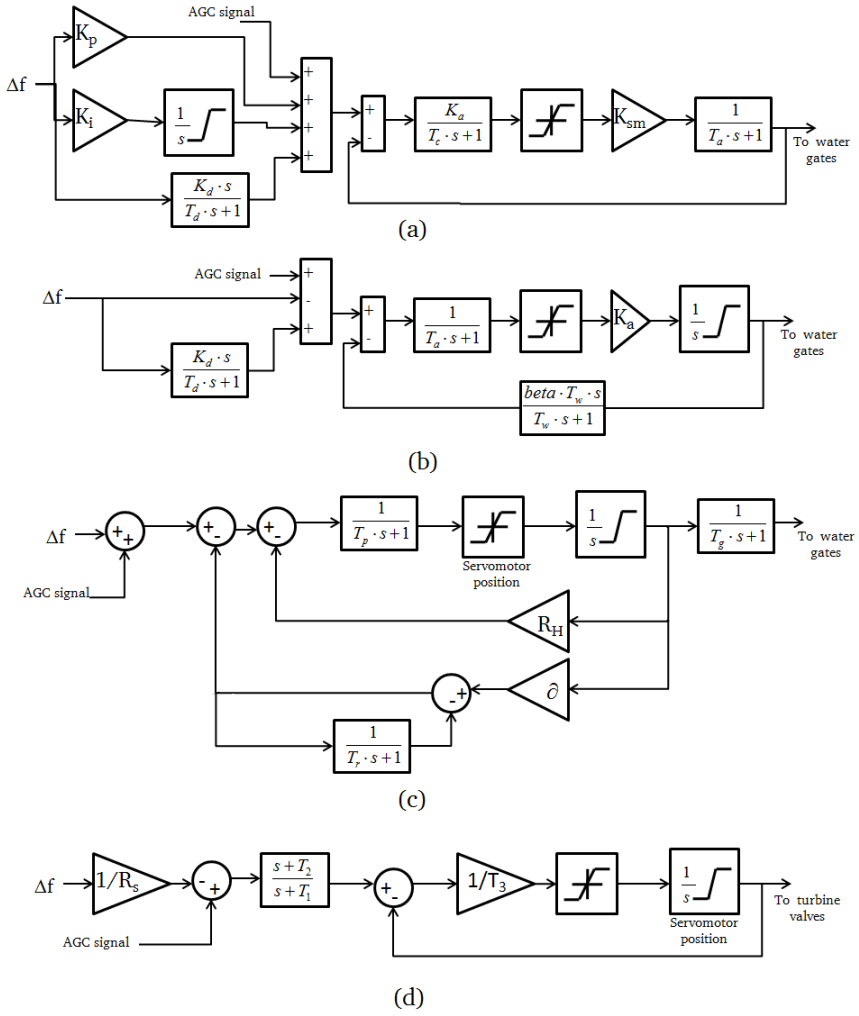

Figure A.1 Conventional generation governors

a) Hydro Woodward PID governor [103] b) Hydro electronic governor [103]
c) Hydro mechanical governor [83] d) Steam governor [44]

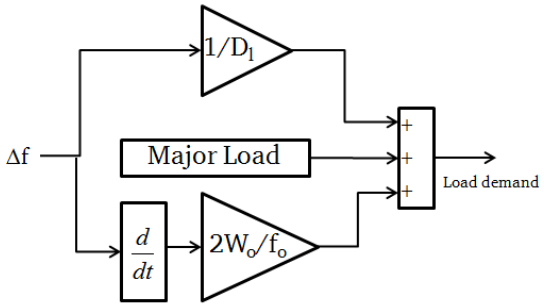

Figure A.2 Complete load model

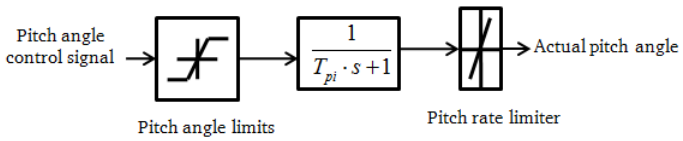

Figure A.3 Servomotor typical model (used to pitch WT blade)

Related publications

International peer reviewed journals

- A. B. Attya, T. Hartkopf, Wind turbines support techniques during frequency drops — Energy utilization comparison, AIMS Energy Journal, vol. 2, no. 3, pp. 219-234, 2014.
- A. B. Attya, T. Hartkopf, Wind turbine contribution in frequency drop mitigation – Modified operation and estimating released supportive energy, IET Journal of Generation, Transmission and Distribution, vol. 8, no. 5, pp. 862-872, May 2014.
- A. B. Attya, T. Hartkopf, Wind farms dispatching to manage the activation of frequency support algorithms embedded in connected wind turbines, International Elsevier Journal of Electrical Power and Energy Systems, vol. 53, issue 1, December 2013.
- A. B. Attya, T. Hartkopf, Control and quantification of kinetic energy released by wind farms during power system frequency drops, IET Renewable Power Generation, vol. 7, issue 3, May 2013.
- A. B. Attya, T. Hartkopf, Penetration impact of wind farms equipped with frequency variations ride through algorithm on power system frequency response, Elsevier International Journal of Electrical Power and Energy Systems, vol. 40, issue 1, September 2012.

International peer reviewed conferences' proceedings

- A. B. Attya, T. Hartkopf, Wind energy in Egypt- Capacity assessment and analyzing penetration impact on grid frequency, in proc. of IEEE 4th International conference on Power Engineering, Energy and Electrical Drives, Istanbul, 2013.
- A. B. Attya, T. Hartkopf, Estimation of wind turbines dynamic model parameters using published manufacturer product data, in proc. of IEEE International Energy Conference and Exhibition, Florence, 2012.
- A. B. Attya, T. Hartkopf, Generation of high resolution wind speeds and wind speed arrays inside a wind farm based on real site data, in proc. of IEEE 11th conference on Electrical Power Quality and Utilization, Lisbon, October 2011.

Acknowledgement

All praise and thanks to Allah

Special thanks to my respectable supervisors Prof. Hartkopf, Prof. Griepentrog, and Prof. Hegazy

Special thanks to my friend and ex-colleague Dr. Peter Engel

Special thanks for the DAAD (Deutscher Akademischer Austausch Dienst), and the Egyptian ministry of high education and research who funded my PhD scholarship.

Special thanks to Prof. Hegazy who provided me with valuable data about the Egyptian case study.

Thanks to my parents, my wife, my children and my friends who supported me, and kept their patience and prayers through the road towards this valuable degree.

Thanks to my colleagues in the department.

Academic career

Employment history

- German Egyptian Research Long term scholarship (GERLS)- [01.10.2011 till now]

Full PhD scholarship at the Technical University of Darmstadt, at the department of Renewable Energies. Thesis topic: Wind energy penetration impact on grid frequency during normal operation and frequency drops

- Part time research assistant – Technical University of Darmstadt [01.12.2012 till now]

Tutor and instructor in undergraduate and postgraduate tutorials beside the supervision of master students. Courses: Renewable Energies and Efficient use of Energy

- Research Assistant – GUC (German University in Cairo) - [05.9.2006 -30.9.2010]

Tutor and instructor in undergraduate and postgraduate tutorials and labs in the faculty of Information Engineering and Technology (IET), besides the supervision of the bachelor projects. Courses: Power Electronics, Electrical Circuits I, Electrical Circuits II and Advanced power electronics lab.

Education

- M. Sc. in Electrical Power Engineering, Faculty of Engineering, Ain Shams University. Thesis title: Impact of Distributed Generation Technology on Distribution System Reliability **[May 2008]**
- B. Sc. in Electrical Power Engineering, faculty of engineering, Ain Shams University. Grade: Very Good with Honour (ranked 11^{th} over 280 students) **[July 2005]**.
- High school education at Saint Fatima language school, (English as a first Language, French as a second language), Secondary certificate (Grade: 98%) **[July 2000]**

Master thesis topic

Adequacy analysis of distributed generation, and offered methodologies to judge the system performance. MATLAB codes were developed to estimate reliability indices based on Monte Carlo simulation. Different generation techniques were examined. Cost-worth reliability evaluation was implemented in an attempt to judge on the feasibility of any modifications that could be applied in a given power network.